Investigation of MEMS micro-implants: *in vitro* and *in vivo* analysis for advanced biomedical applications

BALOGH-LANTOS Zsófia

PhD Supervisors:

Dr. HORVÁTH Ágoston Csaba, PhD

Dr. IVÁN Kristóf, PhD

A dissertation submitted for the degree of

Doctor of Philosophy

Pázmány Péter Catholic University

Roska Tamás Doctoral School of Sciences and Technology

Budapest, 2025

Abstract

The brain is the most complex and vital organ in the body. It is responsible for regulating cognitive functions, emotions, motor skills, and autonomic processes. Despite its remarkable adaptability, the brain remains vulnerable to a variety of diseases, including neurodegenerative and neurological diseases, as well as disorders affecting glial cells and tumors. Conditions such as Alzheimer's, Parkinson's, and epilepsy not only have a significant impact on quality of life but also place a heavy burden on global healthcare systems. Understanding the underlying mechanisms of these disorders is essential for the development of effective treatments and prevention strategies.

One of the most promising advances in neuroscience research is the development of neuromodulation techniques that allow for precise control of neuronal activity. Infrared neuromodulation, a method that uses infrared light to selectively manipulate neurons, has emerged as a minimally invasive and highly targeted approach. Temperature changes induced by infrared stimulation play a critical role in modulating neuronal states. High-density laminar electrode recordings were used to study the effects of pulsed and continuous-wave infrared stimulation on cortical neurons in anesthetized rats. The results show that infrared stimulation has a layer and cell-type-dependent effect on neuronal activity. Pulsed stimulation primarily enhances neuronal firing, whereas continuous stimulation tends to suppress activity. These findings provide valuable insights into the biophysical mechanisms underlying infrared neural stimulation and highlight its potential as a powerful tool for modulating brain activity.

The second part of the study focuses on microimplants designed for precise neural recording and intervention. These implants allow neural activity to be monitored with exceptional temporal and spatial resolution, making them essential tools for the study of brain function and neurodegenerative diseases. In the first part of this research, the optical properties and long-term spike detection performance of a thiol-ene/acrylate shape memory polymer-based microelectrocorticography (microECoG) device were evaluated. This shape-memory polymer (SMP) microECoG is compatible with two-photon microscopy and allows simultaneous optical imaging and electrophysiological recording. The results indicate that the SMP microECoG does not introduce significant optical distortion and allows the detection of single unit spikes over long periods, up to at least seven weeks, demonstrating its reliability for long-term neural monitoring.

This research advances the understanding of how neurotechnologies can be used to study or modify brain activity, offering new avenues for therapeutic intervention and improving the precision of neural monitoring techniques.

Kivonat

Az agy a testünk legösszetettebb és legfontosabb szervei közé tartozik, mivel irányítja a kognitív funkciókat, az érzelmeket, a mozgáskoordinációt és a vegetatív folyamatokat. Bár rendkívüli alkalmazkodóképességgel bír, továbbra is érzékeny a neurodegeneratív és neurológiai betegségekre, valamint glia sejteket érintő rendellenességekre, és daganatokra, amelyek működését és szerkezetét egyaránt befolyásolhatják. Az olyan betegségek, mint az Alzheimer-kór, a Parkinson-kór és az epilepszia nemcsak az érintettek életminőségét rontják jelentősen, hanem komoly terhet jelentenek a globális egészségügyi rendszerek számára is. E betegségek kialakulásának és működési mechanizmusainak feltárása kulcsfontosságú az eredményes kezelések és megelőzési stratégiák kidolgozásában.

Az idegtudomány egyik legígéretesebb fejlődési iránya a neuromodulációs technikák fejlesztése, amelyek lehetővé teszik a neuronális aktivitás pontos szabályozását. Az infravörös neuromoduláció olyan módszer, amely infravörös fény segítségével képes szelektíven befolyásolni a neuronokat, így minimálisan invazív és rendkívül célzott megközelítést kínál. Altatott patkányok agykérgében nagy sűrűségű lamináris elektródafelvételekkel vizsgáltam az impulzus üzemű és folytonos üzemű infravörös stimuláció hatásait. Eredményeim azt mutatják, hogy az infravörös ingerlés réteg- és sejttípusfüggően befolyásolja a neuronális aktivitást: az impulzus üzemű stimuláció elsősorban fokozza, míg a folytonos üzemű stimuláció inkább csökkenti az idegsejtek tüzelési gyakoriságát. Ezek az eredmények értékes ablakot nyitnak az infravörös neurális stimuláció biofizikai alapjainak megismerésére, és megerősítik a módszer gykorlati használhatóságát az agyi aktivitás célzott modulálásában.

A tudományos munkám második része a precíz idegi rögzítésre és beavatkozásra tervezett mikroimplantátumokra összpontosít. Ezek az eszközök kivételes időbeli és térbeli felbontással képesek megfigyelni az idegi aktivitást, így alapvető szerepet játszanak az agyműködés és a neurodegeneratív betegségek vizsgálatában. Kutatásom első szakaszában egy tiolén/akrilát alapú alakemlékező polimerből készült mikroelektrokortikográfiás eszköz optikai tulajdonságait és hosszú távú extracelluláris akciós potenciál detektálási teljesítményét vizsgáltam. Az SMP microECoG kompatibilis a kétfoton-mikroszkópiával, így lehetővé teszi az egyidejű optikai képalkotást és az elektrofiziológiai méréseket. Eredményeim szerint az SMP microECoG nem okoz számottevő optikai torzulást, és képes az egyedi extracelluláris akciós poteniálok legalább hét héten át történő megbízható észlelésésre, ami igazolja alkalmazhatóságát az idegi aktivitás hosszú távú monitorozásban.

Ez a kutatás hozzájárul annak mélyebb megértéséhez, hogy a neurotechnológiák miként alkalmazhatók az agyi aktivitás vizsgálatára és befolyásolására. Eredményeim új lehetőségeket nyitnak a terápiás beavatkozások terén, miközben javítják az idegi megfigyelési technikák pontosságát és megbízhatóságát.

Contents

Acronyms

AC Alternating current

aCSF Artificial Cerebrospinal Fluid

ANOVA Analysis of Variance

BBB Blood-Brain Barrier

CT Computed Tomography

CVD Chemical Vapor Deposition

CW Continous Wave

DG Dentate Gyrus

DRIE Deep Reactive Ion Etching

ECoG Electrocorticography

EEG electroencephalography

EIS Electrochemical Impedance Spectroscopy

FBR Foreign Body Response

FOV Field of View

INS Infrared Neural Stimulation

IR Infrared

ISI Inter-Spike Interval

LFP Local Field Potential

LTP Long-Term Potentiation

MEG Magnetoencephalography

MEMS Microelectromechanical Systems

microECoG Microelectrocorticography

MRI Magnetic Resonance Imaging

MS Multiple Sclerosis

MUA Multi-Unit Activity

OCT Optical Computed Tomography

PD Parkinson's Disease

PDMS Polydimethylsiloxane

PVD Physical Vapor Deposition

PW Pulsed Wave

RIE Reactive Ion Etching

ROI Region of Interest

SiC Silicon Carbide

SIROF Sputtered Iridium Oxide

SMP Shape Memory Polymer

SNR Signal-to-Noise Ratio

SUA Single-Unit Activity

SWR Sharp Wave Ripple

TiN Titanium Nitride

TRPV Transient Receptor Potential Vanilloid

1 General introduction

1.1 Neuronal signals and computation: from brain structures to data processing

The brain is the body's most complex and vital organ, responsible for controlling cognitive functions, emotions, motor skills, and autonomic processes. Despite its remarkable adaptability, the brain remains vulnerable to a variety of diseases, including neurodegenerative and neurological diseases, as well as disorders affecting glial cells and tumors. Neurodegenerative diseases, including Alzheimer's disease [1], Parkinson's disease [2], and epilepsy [3], have a significant impact on the quality of life of individuals and place a growing burden on healthcare systems around the world [4]. Understanding the role of the brain in these diseases is critical to developing effective treatments and prevention strategies.

Neurodegenerative diseases often result from a combination of genetic, environmental, and lifestyle factors that contribute to neuronal damage and dysfunction. These diseases can result in progressive neuronal loss, impaired neurotransmission, and inflammation, leading to severe cognitive and motor impairments [5]–[7]. Studying the underlying mechanisms of these disorders not only improves our understanding of brain function but also opens avenues for novel therapeutic interventions.

This dissertation begins with an exploration of fundamental aspects of brain function, with a focus on neuronal signals and the structural substrates that support them. Our experiments examined two main brain areas: the somatosensory cortex, a surface structure, and the hippocampus, a deep brain structure. The somatosensory cortex is located on the surface of the brain within the parietal lobe and is primarily responsible for processing sensory information from the body. It plays a critical role in perception and motor control by integrating sensory feedback to refine movements [8], [9]. In contrast, the hippocampus, located deep within the medial temporal lobe, is essential for learning, memory consolidation, and spatial navigation [10], [11]. Rather than emphasizing the broader functional roles of these regions, this work focuses on the structural and cellular elements within them that are directly relevant to our analysis. We focus particularly on the laminar organization of the cortex, consisting of six distinct layers, each with specific input-output patterns and cell-type distributions. This layered architecture plays a crucial role in shaping the flow of information through cortical circuits. Within this scope, three key neuronal cell types are examined: pyramidal neurons, which are the primary excitatory cells found predominantly in layers 2/3 and 5 of the cortex, and two classes of inhibitory interneurons, wide-spiking and narrow-spiking, that modulate

circuit activity and contribute to the generation of oscillatory dynamics. These cell types and laminar structures are present in cortical and hippocampal regions, allowing for a comparative analysis of how local microcircuits function in different anatomical contexts. This study focuses on these shared cellular and structural components to elucidate the mechanisms by which neuronal activity is generated, coordinated, and recorded.

A major technological advance in neuroscience research is the use of microimplants, which allow for precise neural recording and intervention. These implants enable neural activity to be monitored with high temporal and spatial resolution, making them indispensable tools in the study of neurodegenerative diseases. The remainder of this dissertation will introduce the mechanisms of signal generation, spikes, local field potentials (LFP), and various recording techniques. Additionally, different signal processing techniques will be explored to better understand and analyze neural data.

1.1.1 Cortical structure and cell types

1.1.1.1 Laminar structure of the neocortex

The cerebral cortex, also known as the cerebral mantle, is the outermost layer of neural tissue in the brain's cerebrum. This layer is present in both humans and other mammals. This region is considered to be the most extensive area for neural processing in the central nervous system [12], contributing significantly to processes such as attention, sensory perception, cognition, language, memory, and overall consciousness. The neocortex, which constitutes approximately 90% of the cerebral cortex, is distinguished by its unique six-layer arrangement, thereby setting it apart from the more ancient allocortex [13]. In small mammals, such as rats and mice, the neocortex typically measures between 1 and 1.5 millimeters in thickness. The neurons within this region are typically organized based on their respective synaptic functions. The majority of these neurons, constituting approximately 80% of the total population, are excitatory and primarily utilize glutamate as a neurotransmitter. In contrast, the remaining 20% of neurons are inhibitory GABA-erg neurons. The cerebral cortex coats the surface of the brain's hemispheres and features characteristic folds: elevated ridges known as gyri and shallow depressions called sulci. Major sulci and gyri serve as landmarks separating the brain into its primary lobes: frontal, parietal, temporal, and occipital. The neocortex is organized into six distinct layers, designated as layers I through VI. These layers extend from the outer surface near the pia mater and continue inward toward the white matter. Each layer exhibits a distinct neuronal composition and unique connection patterns, establishing interconnectivity with other cortical and subcortical regions. By employing staining techniques that highlight neuronal cell bodies and intracortical axons, early 20th-century neuroanatomists were able to detail the layered structure of the cortex across various species. A significant contribution was made by Korbinian Brodmann [14], who described the neocortex as consisting of six layers.

The first layer, designated as Layer I, is the molecular layer. This superficial layer contains a sparse distribution of neurons, including GABA-ergic rosehip neurons. It is composed primarily of horizontally oriented axons, apical dendritic tufts from deeper

pyramidal neurons, and glial cells [15]. During the developmental process, transient cell types, including Cajal–Retzius cells [16] and cells from the subpial granular layer [17], are also present. On occasion, spiny stellate neurons have also been identified in this region. This layer plays a crucial role in integrating feedback signals and top-down processing, which are essential for attention and associative learning [18]. Contrary to the early hypothesis that inputs to this layer were predominantly cortical in origin [19], more recent evidence suggests that it receives input from matrix-type thalamic neurons [20], whereas core-type thalamic neurons primarily target layer IV [21]. Functionally, layer I serves as a central integrative node, merging ascending sensory data with higher-level predictions. It has been demonstrated that this process plays a critical role in the regulation of perception by filtering excitatory inputs and modulating them with neuromodulatory signals. This regulatory process is facilitated by inhibitory interneurons from various layers [22].

Layer II, or the external granular layer, is characterized by the presence of stellate cells and small pyramidal neurons. It is involved in local cortical processing and horizontal connectivity. It plays a role in local circuit processing and integrating signals from various brain regions. Specifically, neurons in layer II are involved in corticocortical connections, contributing to the integration of information across cortical areas and hemispheres.

The third layer, or external pyramidal layer, is comprised predominantly of small to medium pyramidal neurons and a subset of vertically projecting non-pyramidal neurons. This layer functions as a primary source of output to other cortical areas and serves as a recipient of input from commissural fibers. The layers I–III collectively serve as the primary target of interhemispheric corticocortical inputs, with layer III playing a particularly crucial role in the transmission of outputs.

Layer IV, also known as the internal granular layer, is a specific type of layer in the brain. This layer consists of various stellate and pyramidal cells and is the primary recipient of sensory input from the thalamus, specifically from core-type thalamic neurons [21]. Furthermore, the inferior temporal cortex receives intra-hemispheric cortical inputs, suggesting a role in multimodal integration within the brain. Anatomically, layers I–III are designated as supragranular layers, while layers V and VI are classified as infragranular layers.

Layer V, or the internal pyramidal layer, contains primarily large pyramidal neurons, which serve as the primary output channels of the cortex. These cells transmit signals to a variety of subcortical targets, including the basal ganglia, thalamus, brainstem, and spinal cord.

layer VI, or multiform layer, exhibits a diverse neuronal composition, including spindle-shaped, pyramidal, and multifaceted neurons, which facilitate communication with the thalamus. These reciprocal circuits are meticulously calibrated, with excitatory projections targeting the same thalamic neurons that provide input to the cortex. These excitatory neurons also send collaterals to the thalamic reticular nucleus, thereby providing inhibitory feedback to the thalamus or nearby regions [23]. The hypothesis posits that cholinergic modulation of this feedback loop enables the brain to modulate the sensitivity, or gain,

of incoming sensory signals.

1.1.1.2 Neuronal cell types: pyramidal cells and interneurons

Neuronal computation in the cortex and hippocampus depends on the coordinated activity of different types of cells. Excitatory pyramidal cells and inhibitory interneurons are at the core of local circuit processing. Studying their morphological and electrophysiological characteristics is essential for understanding how information is encoded, transmitted, and modulated in the brain [24], [25].

Pyramidal neurons, which are the primary excitatory cells in the cerebral cortex and hippocampus, are characterized by their distinctive triangular soma, a single, long apical dendrite that extends toward the cortical surface, multiple, horizontally-branching basal dendrites, and a long, myelinated axon that projects to distant targets [26]. They are a major component of cortico-cortical and cortico-subcortical communication and participate in cognitive functions, motor output, and sensory integration [27]. First studied by Santiago Ramón y Cajal [28], pyramidal neurons have become central to investigations of neuroplasticity and cortical organization. A single pyramidal cell in the CA1 region of the hippocampus can have dendritic trees that span approximately $12,000\ \mu m$ and receive up to 30,000 excitatory and 1,700 inhibitory inputs [26]. Dendritic spines increase the receptive surface area and are the primary sites for excitatory synaptic input. Apical dendrites branch extensively and are typically studded with thousands of spines, enabling these neurons to integrate synaptic inputs over large spatial domains. Basal dendrites emerge from the base of the soma and exhibit dense arborization. They also play essential roles in local circuit integration. Electrophysiologically, pyramidal cells generally fire at relatively low and irregular rates. Their spiking behavior approximates a Poisson process, suggesting that they act as coincidence detectors, responding selectively to a specific configuration of excitatory inputs [24]. In the CA3 subregion of the hippocampus, about 37% of pyramidal neurons exhibit a regular firing pattern. This pattern is characterized by a short latency to the first spike and spike frequency adaptation during stronger stimulation, indicating a gradual decline in firing rate over time. Around 46% exhibit weak adaptation, with delayed spike onset at the threshold and minimal adaptation under stronger depolarizing inputs. The remaining 17% demonstrate a burst-firing pattern, in which single spikes at rheobase convert into brief, high-frequency bursts with increased stimulation [29]. Spontaneous bursting is rare under baseline conditions. Bursting behavior in pyramidal cells is important because it is variable and can be modulated by factors such as extracellular potassium concentration, which can shift firing patterns from regular spiking to increased bursting. In the neocortex, most pyramidal neurons exhibit regular spiking patterns with stable interspike intervals during sustained depolarization. Nonetheless, subtypes displaying initial bursts or rapid spike frequency adaptation have also been observed, underscoring the functional diversity of pyramidal cell populations [30], [31]. Pyramidal neurons are also distinguished by their broad action potential waveforms, which are typically characterized by a longer duration and slower repolarization phase

than interneurons. These broader spikes reflect the underlying membrane properties and ion channel distributions that contribute to the pyramidal cells' ability to integrate and output information. Electrophysiological recordings often use waveform shape to differentiate pyramidal neurons from fast-spiking interneurons.

Contrary to the traditional association of broad extracellular spike waveforms with excitatory pyramidal neurons, a subset of inhibitory interneurons exhibits these waveforms. These interneurons include morphologically and functionally distinct subtypes, such as Martinotti cells, double bouquet cells, and certain spiny interneurons that target dendrites [32], [33]. These cells are generally parvalbumin-negative and differ from narrow-spiking interneurons in their intrinsic membrane properties and synaptic targets. Electrophysiologically, wide-spiking interneurons tend to have slower firing rates and target dendritic compartments rather than the soma of pyramidal neurons. This dendrite-specific inhibition modulates synaptic integration and plasticity rather than spiking output itself, suggesting a complementary role in circuit regulation [32].

Narrow-spiking interneurons are a type of inhibitory neuron characterized by short extracellular action potentials, typically less than $300\mu s$ from trough to peak [32], [34]. Often fast-spiking, these interneurons display minimal adaptation, enabling them to fire at high frequencies. They are commonly associated with parvalbumin-positive basket cells, which provide strong perisomatic inhibition to pyramidal cells [33]. Functionally, narrow-spiking interneurons are crucial for controlling excitability and timing within cortical and hippocampal circuits. They participate in feedforward and feedback inhibition, synchronizing the activity of large populations of pyramidal cells and contributing to oscillatory dynamics and temporal precision [24], [35]. Their involvement in cognitive processes, such as working memory and attentional selection, has been demonstrated in rodent and primate studies [32]. These cells typically exhibit high-frequency firing, with some cells reaching frequencies of 300-400 Hz or more. They are also capable of maintaining such high-frequency firing for extended periods, which exceeds the duration observed in other interneuron types. It has been demonstrated that other interneurons, including somatostatin-expressing cells, exhibit intermediate maximal firing rates of approximately 230–250 Hz. In contrast, pyramidal cells typically demonstrate lower maximal firing frequencies, ranging from 130 to 150 Hz [29]. Figure 1.1 illustrates the distinctions among the three cell types based on trough-to-peak time and burst index characteristics.

Together, pyramidal cells and interneuron subtypes comprise the foundation of cortical and hippocampal processing. Pyramidal cells integrate and transmit excitatory signals across brain regions, while interneurons, including both narrow- and wide-spiking types, modulate network excitability and synchronize neural ensembles through inhibition. Advances in large-scale recordings and classification tools have improved our understanding of these fundamental cell types and their role in cognition and behavior [37].

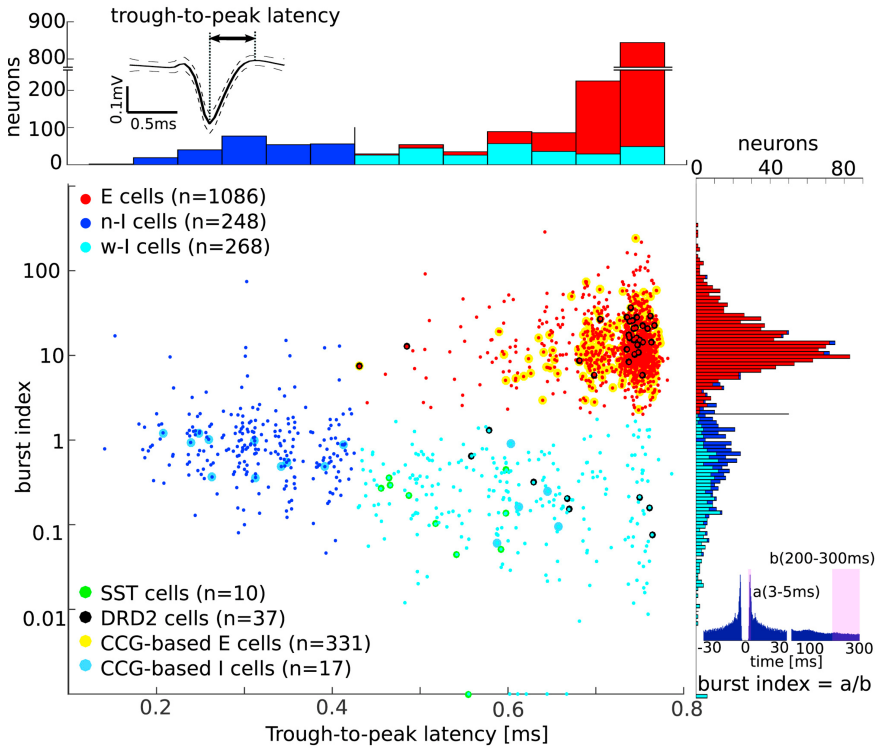

Figure 1.1: Waveform classification of recorded units. Each dot in the graph represents a single unit plotted by trough-to-peak latency and burst index. Units exhibiting a latency below 0.425 milliseconds were designated as narrow-waveform putative interneurons (n-I, blue). Units with broader waveforms were separated into excitatory neurons (E, red; burst index > 1.8) and interneurons (w-I, cyan) based on the bimodal distribution of burst indices (right panel). Green and black circles indicate optogenetically tagged SST+ and DRD2+ cells, respectively. Additional identification via short-latency spike cross-correlograms highlights CCG-defined excitatory (yellow) and inhibitory (blue) units. Top inset shows an example waveform (mean ± SD). Bottom right inset illustrates the burst index definition: spike count in 3–5 ms bins divided by the mean spike count in 200–300 ms bins. Source: [36].

1.1.2 Signal generation and cortical oscillations

The generation and propagation of signals are fundamental to brain function, with neurons communicating by generating electrical impulses, known as action potentials, which travel along their axons to transmit information. This process is essential for neural activity and underlies a wide range of functions, from basic reflexes to complex cognitive processes. The velocity and efficiency of signal propagation are influenced by factors such as axon myelination, while the interaction between excitatory and inhibitory neurons ensures that signals are generated and transmitted in a coordinated and balanced manner, thereby maintaining proper brain function.

The ability of neurons to generate and transmit electrical signals is fundamental to brain function. More than 80 years ago, Hodgkin and Huxley [38] uncovered the processes behind the action potential by recording electrical changes in the membrane of a squid giant axon. The initiation of stimulation in a neuron precipitates a rapid change in

membrane potential, known as the action potential, which is propagated down the axon. The initiation of an action potential within the axon terminal is known to induce the opening of voltage-gated calcium (Ca^{2+}) channels, thus facilitating the influx of calcium ions into the presynaptic neuron, a pivotal step in the process of neurotransmitter release. The increase of the intracellular Ca^{2+} concentration subsequently prompts the fusion of synaptic vesicles, which are filled with neurotransmitters, with the presynaptic membrane. This process is fundamental to the communication between neurons, which is a prerequisite for the processing and relaying of information by the brain. The coordinated activity of multiple neurons firing action potentials in synchrony gives rise to rhythmic patterns of electrical activity known as neural oscillations. These oscillations, like delta, theta, alpha, beta, and gamma (Figure 1.2), are the result of a complex interplay between excitatory and inhibitory neurons, as well as the temporal dynamics of synaptic transmission and membrane properties. Distinct oscillation frequencies are indicative of specific modes of neural communication and information processing within brain networks.

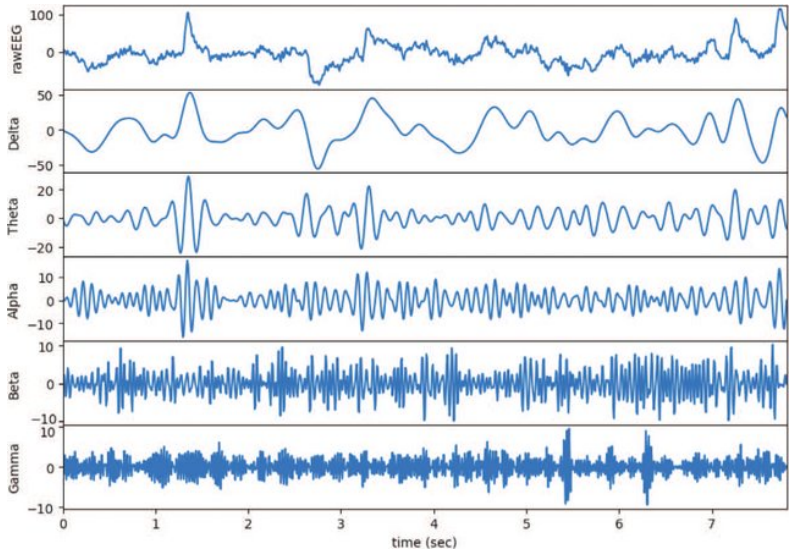

Figure 1.2: Cortical oscillations. The x-axis represents time (s), while the y-axis shows amplitude (μV). Source: [39].

The delta band (less than 4 Hz) is most prominent during deep sleep, particularly slow wave sleep, and is thought to be associated with restorative processes in the brain. They are the slowest brainwaves recorded in humans and are most prominent during the deep stages of non-rapid eye movement (NREM) sleep, especially stage N3 or slow-wave sleep (SWS) [40]. Delta waves are crucial for restorative sleep, brain rejuvenation, and overall physical healing.

Theta waves (4-7 Hz) are typically observed during drowsiness, relaxed wakefulness, and light sleep, but they also play a critical role in cognitive functions such as working memory, learning, and navigation. Theta oscillations are particularly prominent in the hippocampus and prefrontal cortex during tasks requiring attention or memory processing.

The alpha band (8-12 Hz) is most commonly seen when a person is relaxed but awake, especially with eyes closed, and is thought to reflect a resting state of cortical networks. Alpha waves are often observed in the occipital cortex during visual processing tasks, and

a reduction in alpha power is associated with increased cognitive engagement.

The beta band (13-35 Hz) is most evident during motor control and active thinking. Beta rhythms are prominent when the brain is in a state of alertness or during voluntary movement, and they increase in the motor cortex during movement preparation and execution.

Finally, the gamma band (above 35 Hz) is associated with higher cognitive functions such as attention, sensory processing, and cognitive binding. Gamma rhythms are observed in regions involved in sensory integration and neural synchrony, especially during tasks requiring focused attention and perception.

1.2 Micro implant technologies: connecting neuroscience with medical innovation

1.2.1 Microfabrication techniques

A typical ECoG electrode consists of three primary components: the substrate, encapsulation, and lead. The substrate is defined as the foundational material that provides support for the active components of the electrode, thereby ensuring its structural integrity and long-term functionality. A balance of mechanical properties is required, including flexibility and strength, while also ensuring biocompatibility to prevent any adverse tissue reactions [41]. Materials commonly utilized for substrates include silicone, polyimide, and parylene. The selection of these materials is based on their capacity to adapt to the soft tissue of the brain, thereby minimizing mechanical mismatch that could potentially lead to inflammation or tissue damage [42]. The encapsulation layer fulfills the function of a protective barrier around the electrode, thus preventing the surrounding biological environment from degrading the device. Furthermore, it assists in the isolation of electrical currents, thereby avoiding interference with nearby tissues. Typically, encapsulation is made from biocompatible polymers, such as parylene, which are inert in biological settings. This layer helps to reduce the foreign body response and extend the device's longevity by protecting it from moisture and other factors that could cause degradation. The lead constitutes the conductive pathway that connects the electrode to the external recording or stimulation system and is composed of materials such as platinum or gold, which are recognized for their excellent electrical conductivity and resistance to corrosion. The lead must also be sufficiently flexible to accommodate the movements of the brain without causing mechanical damage to the electrode or the surrounding tissue [43]. Advances in microfabrication techniques have enabled the creation of thin, flexible leads that maintain high signal quality and durability. The integration of substrate, encapsulation, and lead is critical to the performance and longevity of the electrode. In this section, microfabrication techniques used to create these components will be explored, introducing processes that are improving the development of long-lasting, high-performance neural interfaces.

Microfabrication techniques play a critical role in the development of microelectromechanical system (MEMS) electrode devices, enabling the creation of miniaturized, high-

precision components for applications in biosensors, neural interfaces, and microelectronics. These devices are typically manufactured using processes derived from the semiconductor industry, such as photolithography, thin film deposition, and etching. The choice of materials, including metals, silicon, and biocompatible polymers, depends on the specific application requirements. Advances in microfabrication have enabled the development of highly sensitive and durable MEMS electrodes, enabling innovations in medical diagnostics, neural stimulation, and environmental sensing.

The primary area of interest is the device's small size, as it facilitates both biocompatibility and the capacity to interface with individual neurons [44]. Given the small size of neurons, the recording sites must be scaled to approach the size of the neurons themselves. Achieving such a compact size requires a high-resolution patterning technique. Photolithography is a precise method for patterning a photoresist-coated substrate [45]. After spin-coating the photoresist, a photomask is used to expose the substrate to light, changing the solubility of the photoresist. Positive resists become more soluble, negative resists less. The exposed areas are developed and removed, allowing further processing like etching or layer deposition. Finally, the remaining photoresist is stripped. Figure 1.3 shows this process and the difference between resist types.

Bulk micromachining creates 3D microstructures by selectively removing material from within the substrate. Unlike surface micromachining, which builds on the surface using thin films, bulk micromachining shapes deeper features via wet chemical etching or dry methods like reactive ion etching (RIE) and deep reactive ion etching (DRIE). It's ideal for fabricating high aspect ratio structures from micrometers to centimeters in height [46].

Surface coating techniques deposit thin layers to enhance material properties and performance. Common methods include vapor-phase processes like chemical vapor deposition (CVD) and physical vapor deposition (PVD), which produce durable, high-quality coatings [47]. PVD transfers material from a solid source to vapor that condenses on a substrate, with techniques such as thermal evaporation and sputtering, ideal for temperature-sensitive materials. CVD grows films through chemical reactions of gaseous precursors on the substrate, offering uniform, high-purity coatings on complex shapes. Although CVD usually requires higher temperatures and precise control, plasma-enhanced variants allow deposition at lower temperatures, suitable for microelectronics and protective coatings.

Neurobiological electrodes are typically subjected to more rigorous testing than conventional physiological devices to ensure their reliability and long-term stability. One widely used evaluation method is accelerated aging testing, which exposes the electrodes to elevated environmental conditions, such as increased temperature, humidity, vibration, light, and oxygen, to simulate long-term degradation over a shorter time frame. This technique is essential for identifying potential failure mechanisms and predicting the device's lifespan under normal physiological conditions. The rate of chemical reactions increases exponentially with temperature, as described by the Arrhenius equation. A general approximation suggests that for every 10°C increase, the rate of polymer reactions doubles, making temperature a key factor in accelerated aging studies [48]. These tests

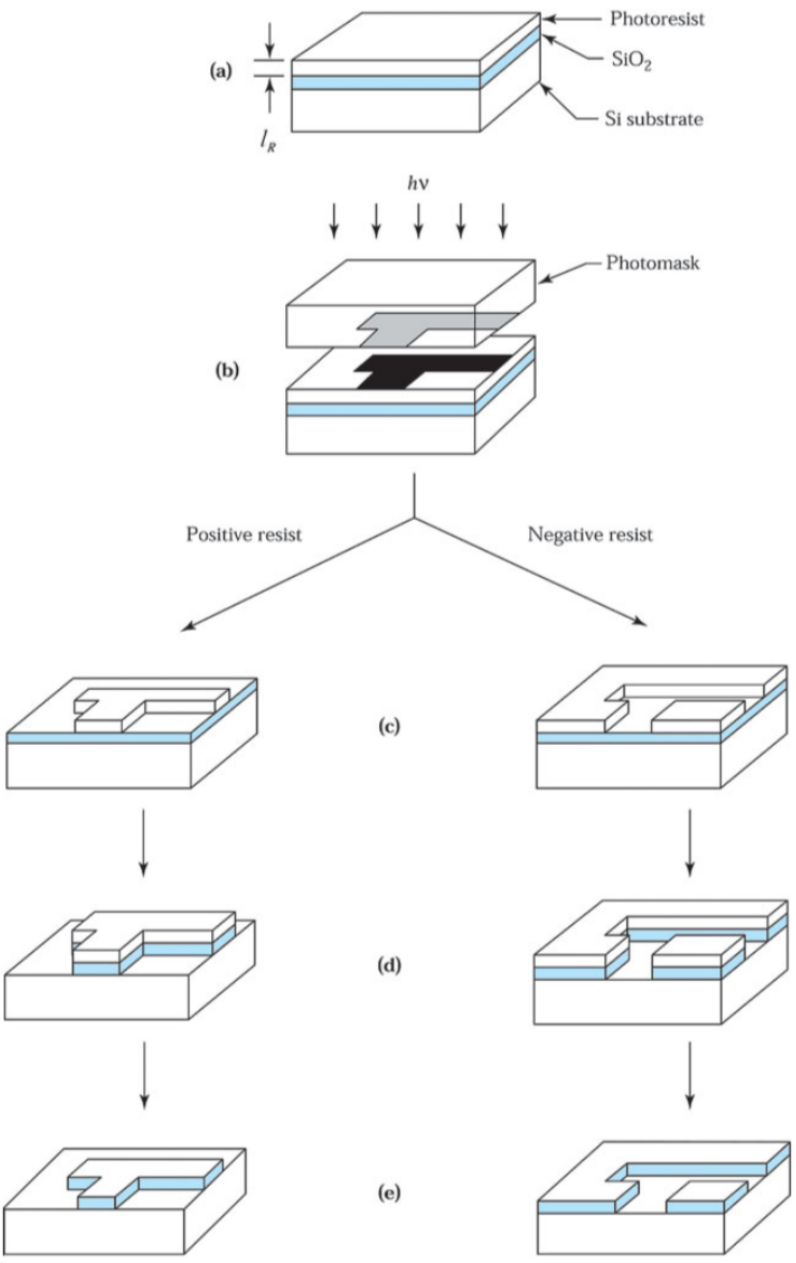

Figure 1.3: Schematic representation of the photolithographic process. (a) A silicon (Si) substrate is coated with a silicon dioxide (SiO_2) insulation layer, followed by a photoresist coating. (b) A mask is then placed over the resist, and UV exposure alters its chemical structure. (c) For positive photoresist, the exposed areas are dissolved in the developer solution (left side), while in negative photoresist, the unexposed areas are removed, leaving the reverse pattern (right side). (d) The wafer is then etched in an environment that removes the exposed SiO_2 insulation layer but does not affect the resist. (e) Finally, the resist is stripped, leaving the insulator pattern: in the case of positive photoresist, the pattern mirrors the opaque image on the mask (left side), and for negative photoresist, the pattern is the inverse of the mask image (right side). Source: [46].

provide valuable insights into the durability of electrode materials, helping to ensure their performance over extended periods in biological environments. In addition to structural

and functional optimization, another critical consideration for neurobiological electrodes is their biocompatibility. The following section will explore how material choices and surface modifications influence the interaction between implanted electrodes and biological tissues, with a focus on minimizing inflammatory responses and improving long-term integration.

1.2.2 Biocompatibility

Glial cells are an important element of nervous tissue. Their main function is to support neural cells, develop the blood-brain barrier, maintain a stable environment, assist the transmission of stimuli, and participate in the immune response of tissues [49]. An important question regarding the development of brain implants and implantable brain biosensors is the effect of the implanted device on living organisms and cells.

The interactions between an implanted device and the biological tissue arise from several factors, including surgical procedures, device repositioning, and oscillatory micromotions. These micromotions are small displacements caused by brain movements, which are influenced by physiological activities such as respiration and blood flow [50]. These mechanical interactions can lead to tissue damage and inflammation, ultimately affecting the long-term stability and performance of the implanted device.

Furthermore, the tissue trauma resulting from implantation elicits a foreign body response (FBR), or encapsulation. The foreign body response is a neuroinflammatory reaction triggered by the presence of the implanted device in the brain. This reaction can compromise the stability of neural recordings, rendering them unreliable over time [41]. A key feature of the foreign body response is persistent inflammation at the biotic-abiotic interface, typically marked by the activation of microglia and macrophage biomarkers [51]. This chronic inflammatory environment can lead to tissue damage and signal degradation, creating significant challenges for long-term neural monitoring. As part of the inflammatory response, other plasma components enter the area, and local astrocytes and microglia transition from resting to active, phagocytic phenotypes [52]. The activation of microglia and macrophages releases anti-inflammatory chemokines and cytokines to the damaged area. These molecules play a role in tissue remodeling and the degradation of foreign materials, but they also contribute to neurodegeneration. Studies have reported the loss of nerve fibers and nerve cells surrounding the implanted device [51], [53], [54]. However, the persistent inflammation and neural loss observed in these cases are not typically associated with the initial stab wound injuries caused by device implantation. This suggests that these inflammatory responses are driven by the continuous presence of the implant, rather than the mechanical injury from implantation itself [53].

In addition to these cellular and inflammatory responses, the blood-brain barrier (BBB) is often compromised, leading to a decrease in myelin within the surrounding tissue [51]. Figure 1.4 illustrates the process of the foreign body response.

The trauma caused by implantation can arise from several factors, including mechanical insertion, protective mechanisms, and mechanical mismatch. The insertion of the device causes local injury, triggering a wound-healing response. The mechanical mismatch refers

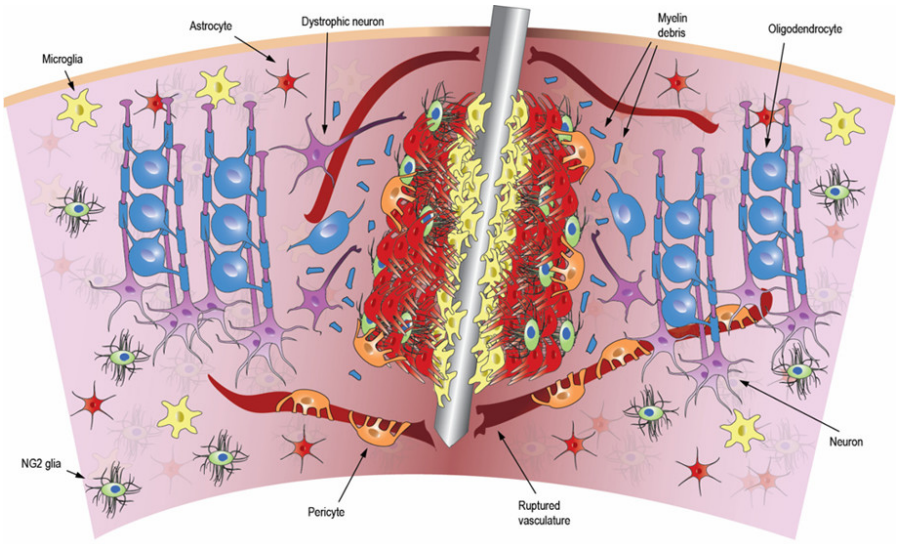

Figure 1.4: Neural interfaces and electrodes disrupt local tissue, triggering an acute immune response. Microglia and astrocytes migrate to the area, where they release anti-inflammatory factors. The astrocytes are forming the scar around the implant. Source: [55].

to the difference in Young's modulus between the brain tissue and the implanted device, which can significantly affect the tissue's response. Traditionally, electrodes for cortical and deep brain recordings are microfabricated using metals or silicon [56], [57]. Due to the stiffness of these materials, the mechanical mismatch between the device and the soft brain tissue contributes to both acute and chronic injuries and exacerbates the foreign body response. This response ultimately leads to encapsulation, where tissue surrounds the electrode, insulating it from the target neurons. As a result, the combined impedance of the electrode and the brain tissue increases, which can significantly impair the device's ability to record neural signals effectively. (Hereafter, any reference to an increase in the impedance of the device will specifically refer to the impedance of this complex system, including both the electrode and the surrounding neural tissue) [52]. Device failure can stem from a variety of biological and mechanical sources. Biological factors contributing to device failure include glial insulation, neuronal death, and bleeding. On the other hand, mechanical factors include delamination, corrosion, and encapsulation. In the early stages of gliosis, microglial cells are activated, releasing factors that trigger the activation of astrocytes. This leads to an initial increase in the impedance of the device over several days, which later stabilizes before gradually decreasing [58]. In addition to gliosis, corrosion of the metal and the degradation of the passive layers surrounding the device are also known causes of failure and instability in long-term implanted electrodes [59]. These issues, along with neuronal cell loss surrounding the electrodes in the brain, significantly contribute to device failure and result in inconsistent recording performance [60]. However, the implementation of precise microfabrication and implantation techniques, as demonstrated by NeuroProbes silicon probes, has shown that when insertion injury, particularly blood vessel damage, is minimized, the resulting tissue response can be significantly reduced with minimal neuronal loss and gliosis [61].

There are different methods to measure the stability of the device. One method is immunofluorescence staining, which is an anti-body-based staining of the brain slice. The most used stains are DAPI and Anti-Neun, which bind to the nuclei, and Anti-GFAP, which is a glial-specific protein. With immunofluorescence staining the foreign body response can be measured, which indicates the biocompatibility and stability of the device [42]. Another method to measure the stability and reliability of the implanted probes is electrochemical impedance spectroscopy (EIS) with Bode plot representation. This is a double-axis plot, with the impedance value on the primary vertical axis, phase angle on the secondary vertical axis, and frequency on the horizontal axis, as figure 1.5 shows. This plot helps the understanding of how the device circuit behaves at different frequencies because the impedance of circuit elements changes with frequency. Also, EIS contains more information than DC techniques or single-frequency measurements, like information from high-frequency electrode kinetics, and from low-frequency diffusion or mass transport regions.

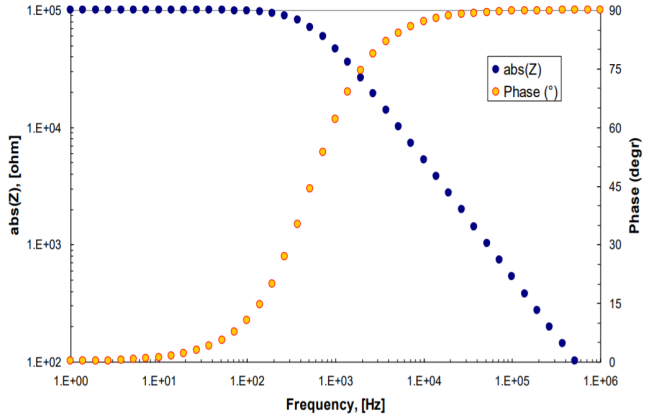

Figure 1.5: Bode plot. The electrode impedance is plotted with the logarithm of the frequency on the horizontal axis and both the absolute value of the impedance and phase angle on the vertical axes. Source: [62].

Multiple strategies are available to reduce the neuroinflammatory effects and decrease the likelihood of device failure. Beyond chemical signaling, the extracellular environment in the brain also presents cells with a variety of geometrically defined, three-dimensional physical topographies at the micro- and nanometer scale. These topographies significantly influence neuronal development, function, and regeneration [63]. Recently, advances in micro- and nanomanufacturing technologies have enabled the creation of biometric structures that allow for the topographic regulation of cellular functions with unprecedented spatial and temporal resolution. By tailoring the surface of the device to mimic these natural patterns, the electrode surface becomes more favorable to cells, allowing for better cellular adhesion and migration along the device surface [64]. Incorporating bioactive coatings is another effective strategy for improving the biocompatibility of the implant. Cellular behavior is strongly influenced by both the chemical and physical properties of the surrounding environment, and bioactive coatings can enhance cellular interactions with the implant [65].

One promising strategy to reduce the mechanical mismatch between the implanted device and brain tissue is the use of materials with Young's modulus that closely approximates that of brain tissue.[66] Young's modulus, also known as the elastic modulus, is a measure of the stiffness of a material and describes how much a material will stretch or compress under a given force. This approach helps mitigate the risk of tissue damage and inflammation, which are often caused by differences in stiffness between the device and surrounding tissue. Furthermore, replacing traditionally used rigid materials with more adaptive and biocompatible alternatives, such as flexible materials that adjust their elastic modulus to match the brain's elastic modulus at body temperature, can reduce both neuroinflammatory effects and the likelihood of device failure. Figure 1.6 shows the Young's modulus of various materials. The brain tissue lies in the kilopascal (kPa) range, typically around 1–10 kPa, which indicates its soft and flexible nature. In contrast, shape-memory polymers, when in a soft state, have Young's modulus around 300 MPa. Most polymers generally fall within the gigapascal (GPa) range, while materials like silicon have a much higher modulus, typically ranging from 100 to 200 GPa.

Using shape-memory polymers that adjust to body temperature softens the implant and minimizes scarring, offering a promising solution for enhancing the long-term viability and effectiveness of implanted devices. A flexible implant that changes its elastic modulus in response to body temperature can reduce scarring and improve integration with surrounding tissue [42].

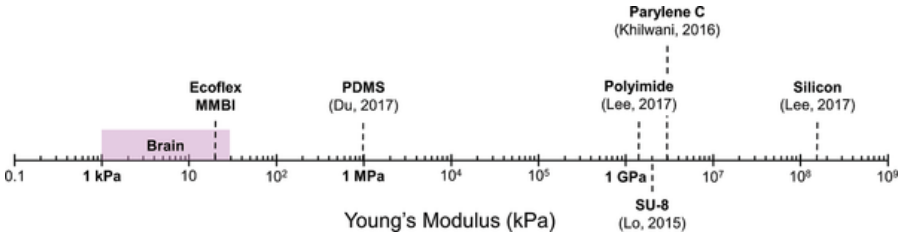

Figure 1.6: Young's modulus of the brain and different electrode substrate materials. Shape-memory polymer, which is not denoted in the figure, has a Young's modulus in the few hundred MPa range. Source: [67].

1.3 Photoelectric artefacts

Photoelectric artefacts are distortions in imaging that occur when high-energy photons interact with the detector material, commonly in techniques such as two-photon microscopy and electrophysiology. When we use these advanced techniques to study biological tissues, these artefacts can complicate the interpretation of both structural and functional data. Understanding and dealing with photoelectric artefacts is essential to optimize image quality, and their correction is often integrated with image processing techniques to improve the accuracy of imaging and electrophysiological analysis in research.

The photoelectric effect refers to the phenomenon of electrons being emitted from a material when exposed to light, a discovery first made by Alexandre Edmond Becquerel [68] in 1839 while experimenting with photovoltaic cells. Becquerel observed that varying

the intensity of light on two electrodes in an electrolyte solution produced an electrochemical current. Later, Heinrich Hertz's [69] work on electromagnetic waves and Albert Einstein's theoretical contribution in 1905, for which he won the Nobel Prize, refined our understanding of this effect. A key feature of the photoelectric effect is that electrons are only moved when the incident light reaches or exceeds a certain frequency threshold, regardless of its intensity or exposure time [70].

In materials, the behavior of electrons is described by atomic and molecular orbital theories, where electrons occupy discrete energy levels. In solids, these energy levels are organized into bands: the valence band, which holds electrons at the lowest energy levels, and the conduction band, where electrons move freely when excited. The band gap between these bands determines the electrical properties of a material (Figure 1.7). In metals, the valence and conduction bands overlap, allowing electricity to be conducted easily. In semiconductors, a small energy gap allows photons or heat to excite electrons into the conduction band. In contrast, insulators have large band gaps that prevent such excitation. When photons of a certain frequency or energy interact with an electron in an atom or material, energy is transferred from the photon to the electron. For the electron to be dislodged from its orbital, the energy of the incoming photon must be at least equal to the energy required to overcome the binding force holding the electron in its orbital. This energy corresponds to a certain threshold frequency of light.

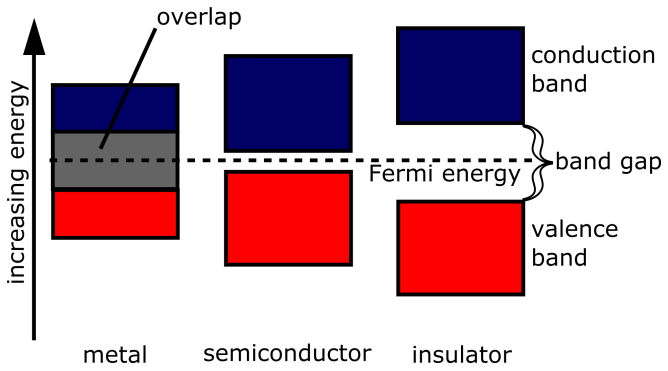

Figure 1.7: Diagram of the band gaps of conductors (metals), semiconductors, and insulators. Source: [71].

The photoelectric effect plays a critical role in imaging technologies, particularly in optogenetics and multi-photon microscopy. When laser pulses are used in optical imaging, photoelectric artefacts can occur, producing electrical signals that resemble neural activity, such as action potentials (Figure 1.8). These artefacts complicate the interpretation of data in experiments designed to study neural responses or local field potentials.

Several strategies have been explored to mitigate the effects of photoelectric artefacts [70]. A common approach in two-photon microscopy is to "zero" or "blank" the laser light amplitude while scanning over electrode sites, thereby reducing the intensity of the photoelectric signals. However, this method only partially attenuates the artefact. Another solution is to use incoherent light sources, which reduce the intensity of the Becquerel effect. In addition, moving the light sources away from the electrode sites can

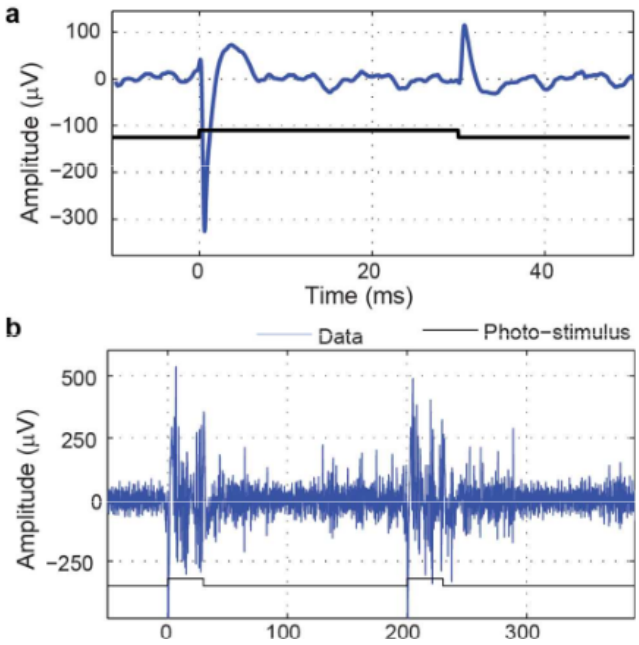

Figure 1.8: A) Photoelectric artefact, recorded with a tungsten electrode during photo stimulation B) Raw data trace. Source:[70].

also minimize photoelectric activation.

For the study of neural activity, one strategy is to use high-frequency pulses with a low-pass filter, which helps to remove the high-frequency noise caused by optical pulses. However, this does not eliminate the challenge of detecting neural spike activity during optical pulse exposure, as the spikes often overlap with the artefacts. One potential solution to this problem is to use transparent electrode materials. Insulators with large band gaps prevent excitation from interfering with electrical conduction, making them ideal for reducing photoelectric interference.

Despite these approaches, the search for materials that balance conductivity with sufficient band gaps remains a challenge in the development of biomaterials for optical imaging and electrophysiology applications. Ultimately, understanding and controlling the photoelectric effect in these technologies is crucial to improving the accuracy of neural recordings and advancing research in optogenetics and beyond.

1.4 Infrared neurostimulation

As neurodegenerative and psychiatric disorders continue to increase in prevalence, there is an urgent need for innovative neuromodulation strategies that can alleviate symptoms, improve quality of life, and offer safe, effective therapeutic options. While traditional pharmacological treatments have been beneficial in many cases, they often come with significant side effects and limited efficacy, particularly for conditions such as Parkinson's disease, epilepsy, and depression. Among the most promising neuromodulation techniques, electrical stimulation has demonstrated considerable success in clinical applications, offering targeted symptom relief for disorders like Parkinson's disease and essential

tremor [72]. Similarly, optogenetics has revolutionized fundamental neuroscience research, allowing precise control of neural circuits with light through genetically modified ion channels [73]. However, optogenetics requires genetic modifications, limiting its immediate clinical translation. In contrast, infrared neural stimulation (INS) is emerging as a promising alternative that harnesses the intrinsic temperature sensitivity of neurons and metabolic processes to modulate neural activity. Unlike optogenetics, INS does not require genetic alteration of the cell membrane, making it a potentially safer and more widely applicable technique for both research and therapeutic use (Figure 1.9). Furthermore, INS enables spatially precise control of neural activity through localized heating, offering a non-invasive and highly targeted approach to neuromodulation [74]. As this field continues to develop, further research is needed to optimize the safety, efficacy, and long-term effects of INS, paving the way for its potential clinical applications in treating neurological disorders.

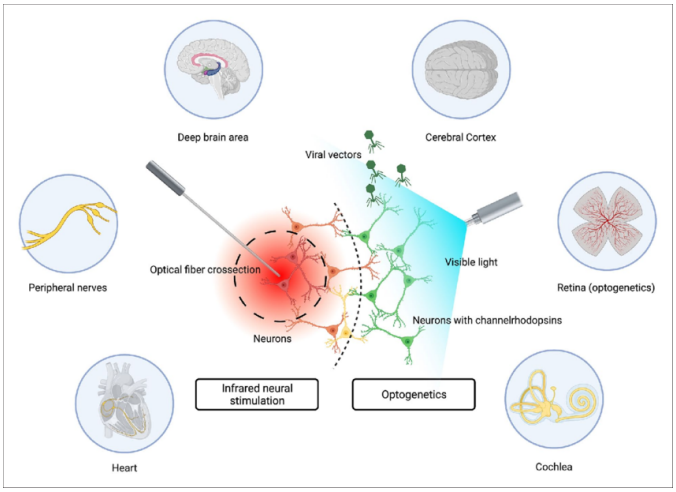

Figure 1.9: Infrared stimulation and optogenetics. INS relies on temperature-induced activation, while optogenetics requires viral transduction and the expression of channelrhodopsins to modulate neural activity. Both methods have been utilized to stimulate various organs and tissues, including the heart, peripheral nerves, deep brain regions, cerebral cortex, retina, and cochlea. Source: [75].

The first evidence supporting the efficacy of infrared neural stimulation dates back to the mid-2000s when Wells and colleagues [76] successfully evoked compound action potentials in the rat sciatic nerve using pulsed infrared light. This groundbreaking discovery paved the way for subsequent research, leading to numerous studies across various species under both *in vitro*[77]–[80] and *in vivo*[81]–[84] conditions. These investigations sought to elucidate the underlying biological mechanisms triggered by infrared illumination and refine the application of INS as a neuromodulation tool. One of the key findings in this field was reported by Albert et al. [85], who identified the involvement of mechanosensitive ion channels, particularly transient receptor potential vanilloid (TRPV) channels, in mediating the excitatory response of neural tissue to infrared stimulation. This insight aligns with the broader significance of TRPV channels in neuroscience, as highlighted by the Nobel Prize-winning discoveries of David Julius and Ardem Patapoutian [86], [87].

Since their identification, TRPV channels have been increasingly recognized for their role in various pathological conditions, including epilepsy [88], Alzheimer's disease [89], and Parkinson's disease [90], further underscoring their importance in neural function and dysfunction. In recent years, the translational potential of INS has gained traction with the first reported human trial, marking a significant milestone in the field and reinforcing its potential as a safe and non-invasive neuromodulation technique [91]. However, despite these advancements, the precise mechanisms of action underlying INS remain an active area of research. Shapiro et al. demonstrated that water content in biological tissue serves as the primary chromophore, leading to localized increases in temperature upon infrared absorption [77]. Additionally, they proposed that electrostatic changes in the cell membrane contribute to the observed spike rate increase, providing one possible explanation for INS-induced neural excitation. While initial studies predominantly focused on the excitatory effects of INS, further research has revealed its inhibitory capabilities as well. Duke et al. [92] initially attributed this suppression of neural activity to an increase in background temperature. However, Ganguly et al. [79] later provided a more detailed explanation based on experimental and theoretical models using an *Aplysia californica* model system. Their findings demonstrated that while sodium channels remained unaffected by thermal changes, the activation of potassium channels led to reversible suppression of neural activity. This discovery offered new insights into the bidirectional effects of INS, broadening its potential applications in neuromodulation. Despite these significant milestones, much of the current knowledge regarding INS remains derived from *in vitro* experiments, and only a limited number of studies have explored its effects on cellular excitability in the living brain. Bridging this gap with more extensive *in vivo* investigations will be critical for fully understanding the physiological impact of INS and advancing its application toward clinical translation.

Our research group's preliminary measurements relying on a neural probe with an integrated platinum heater gave further evidence in mice that temperature change induced by resistive heating is also suitable to modulate neural activity similar to infrared (IR) irradiation [93]. This was also confirmed by a recent study by Zhou et al [94]. To examine the effect of infrared IR stimulation on the activity of neocortical neurons, our group has developed an implantable photonic device (optrode) that can transmit the IR irradiation into the tissue in a spatially confined manner, while simultaneously measuring the evoked electrophysiological response of individual neurons and monitoring the tissue temperature [95], [96]. During the *in vivo* validation of the optrode, we demonstrated for the first time that low-energy (below 13 mW) continuous wave infrared light can be efficiently used to either reversibly excite or suppress the activity of neuronal populations in the cortex of rats with cell type-specific characteristic responses [83]. Moreover, we provided histological evidence that repeated intracortical suppression of multi-unit activity by low-power continuous wave IR light does not lead to heat-induced cell loss under *in vivo* conditions [97]. Although the efficacy and safety of our illumination protocol have been confirmed, a detailed characterization of layer- and neuron-type-specific changes in the activity of neuron populations to IR stimulation within the cortex has not been revealed.

This information would be essential to translate the method to the preclinical settings, aiming at disease-specific neuromodulation schemes.

2 Aims

As neurodegenerative and psychiatric disorders continue to increase on a global scale, there is an urgent demand for innovative neuromodulation strategies that can safely and effectively alleviate symptoms, improve patients' quality of life, and provide alternative or adjunct therapies to conventional pharmacological treatments. While pharmaceuticals have yielded positive results in the treatment of numerous conditions, including Parkinson's disease, epilepsy, and depression, they frequently induce adverse effects and lack the requisite specificity to ensure long-term efficacy. Electrical stimulation techniques, including deep brain stimulation, have demonstrated notable clinical success in addressing specific symptoms, particularly those associated with movement disorders, as evidenced by recent studies [72]. Meanwhile, optogenetics has revolutionized fundamental neuroscience research by allowing precise control of neural circuits through genetically engineered light-sensitive ion channels [73]. Nevertheless, the reliance of optogenetics on genetic modification complicates its immediate clinical implementation.

Infrared neural stimulation is a promising alternative neuromodulation approach that exploits the temperature sensitivity of neurons to modulate activity without the need for genetic manipulation [74]. The INS offers spatially localized, gene-free neuromodulation by inducing controlled, transient heating of neural tissue, thereby enabling highly targeted excitation or inhibition. Since its initial demonstration by Wells et al. [76], which exhibited evoked action potentials in the rat sciatic nerve using pulsed infrared light, INS has been the subject of extensive research in both *in vitro* and *in vivo* settings [77], [81]. However, the underlying mechanisms remain incompletely understood, with studies suggesting roles for transient receptor potential vanilloid channels and membrane electrostatics. It is noteworthy that the majority of insights derived from mechanistic studies originate from *in vitro* research. The layer- and cell-type-specific effects of INS in the intact cortex have not yet been thoroughly characterized, indicating a significant knowledge gap that prevents progress towards preclinical and therapeutic applications. Moreover, the absence of long-term safety and efficacy data for INS in living brain tissue further limits its clinical development.

Concurrently, advances in neural recording technologies have enabled detailed monitoring of brain activity at multiple scales. Microelectrode arrays play a pivotal role in extracellular electrophysiology, particularly for deep brain regions such as the hippocampus, a structure vital for memory and spatial navigation. However, integrating electrophysiological recordings with optical imaging modalities such as two-photon microscopy remains challenging due to the opacity and rigidity of conventional electrode materials. There is an urgent need for transparent, flexible, and biocompatible neural interfaces that enable artifact-free, long-term multimodal recordings combining electrical

signals with high-resolution optical imaging [98]. Recent advancements in polymer materials, such as thiol-ene/acrylate shape memory polymers, hold considerable promise due to their ability to integrate optical transparency, flexibility, and biocompatibility. However, the optical properties and long-term electrophysiological performance of such SMP-based microelectrocorticography devices require comprehensive validation, particularly regarding their compatibility with two-photon microscopy and stability during chronic implantation *in vivo*.

The overall objective of this dissertation is to develop and evaluate novel optical and electrical neural interface technologies for minimally invasive, cell-type-specific neuromodulation and multimodal neural recording, including recording brain activity using various types of brain implants. The aim of this study is twofold: first, to characterize the layer- and cell-type-specific cortical responses to infrared neural stimulation, and second, to assess the optical and electrophysiological performance of a transparent thiol-ene/acrylate-based microECoG device suitable for long-term two-photon imaging and chronic neural recordings.

The specific objectives are:

1. Characterize the layer- and cell-type-specific effects of infrared neural stimulation in the rat neocortex.

   Using a Neuropixels probe during infrared stimulation, I will investigate how principal neurons and interneurons across different cortical layers respond to both continuous-wave and pulsed infrared illumination. This objective includes the quantification of excitatory and inhibitory effects on single-unit activity, as well as the identification of differences between stimulation paradigms and neuronal subtypes. By addressing these critical gaps in understanding the physiological impact of INS *in vivo*, this objective will contribute to a more comprehensive and precise understanding of the mechanisms underlying neural activity.

2. Evaluate optical properties and compatibility of the transparent microECoG device with two-photon microscopy

   This objective focuses on assessing whether the thiol-ene/acrylate SMP-based microECoG device maintains high optical clarity and introduces minimal distortion during two-photon imaging. By imaging fluorescent microbeads and fixed brain slices with and without the SMP microECoG in the optical path, I will quantify potential changes in bead diameter, dendritic morphology, and fluorescence intensity, establishing the SMP microECoG's suitability for simultaneous electrophysiology and high-resolution optical imaging.

3. Assess long-term electrophysiological stability and biocompatibility of the transparent microECoG device during chronic hippocampal recordings

   To validate the SMP microECoG's chronic recording capabilities, I will monitor spike detection quality, signal-to-noise ratio, and stability of hippocampal neural activity over extended implantation periods *in vivo*.

The objective of this research is to address these fundamental gaps in neuromodulation and neural interface technologies. The outcomes of this study will provide critical insights that will contribute to the development of next-generation tools for both basic neuroscience research and therapeutic interventions in neurological and psychiatric disorders.

3 Methods

3.1 Properties of the thiol-ene/acrylate microECoG

Electrophysiological recordings are classified as either invasive or non-invasive, depending on the placement of the electrodes relative to the brain. Non-invasive methods, such as electroencephalography (EEG), record brain activity from the scalp.They are easy to use, but offer limited spatial resolution [99], [100]. In contrast, invasive methods achieve higher spatial resolution by placing electrodes within or on the brain. Examples include the Utah array and Michigan probes, which allow for localized recordings from superficial and deep brain regions, respectively [101], [102]. However, their insertion into brain tissue can provoke immune responses and reduce long-term stability [103].

Electrocorticography (ECoG) offers a middle ground, recording signals from the brain surface using subdural electrodes. It captures both cortical activity and local field potentials (LFPs), reflecting similar neural dynamics with different depth sensitivities. Since ECoG avoids cortical penetration, it presents lower clinical risk and improved long-term stability compared to intracortical devices. A sampling rate of 1–2 kHz is typically sufficient for capturing the lower-frequency oscillations (1–500 Hz) associated with LFPs. Figure 3.1 illustrates electrode placement for various recording techniques.

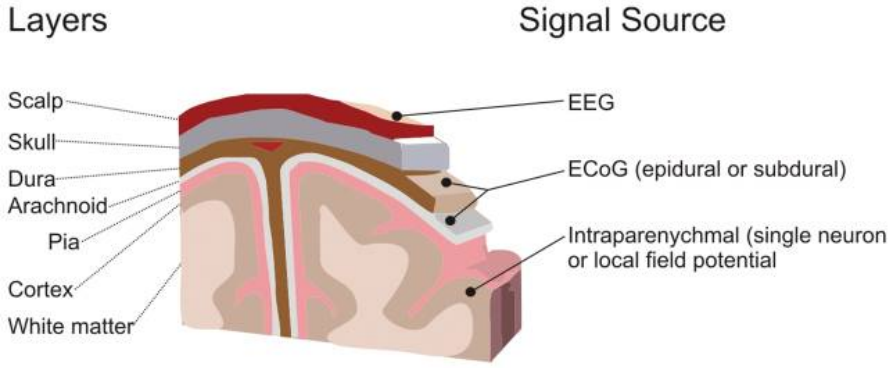

Figure 3.1: Location of signal recording devices in the brain Source: [104].

Minimising the inflammatory response of the nervous system is crucial for improving the longevity and performance of implanted neural devices, particularly in multimodal neuroimaging applications. Responsive polymers, such as thiol-ene acrylates, offer a promising solution to this problem by reducing the mechanical mismatch between the implant and the surrounding tissue. This mitigates chronic inflammation at the tissue-device interface. Thiol-ene-based flexible devices have undergone extensive electrical [105] and optical [106] characterisation, demonstrating high optical transparency (>85% at 550 nm) and a refractive index of approximately 1.54 [107]. These optical properties,

combined with the material's flexibility and biocompatibility, enable its use in wearable LED devices [108] and establish it as an ideal candidate for neural interfaces integrating cortical electrophysiology and simultaneous two-photon imaging. The shape-memory properties of thiol-ene acrylates further support their use in developing transparent, flexible implants that can maintain stable, long-term neural recordings with minimal tissue disruption. In our previous paper [60], we presented the change of the Young's modulus of a thiol-ene/acrylate neural probe, which decreased from 2 GPa to 300 MPa upon immersion into room temperature saline solution and heating the medium up to 37 °C. Later, we proposed the first thiol-ene/acrylate-based microECoG device and confirmed its electrical stability and biocompatibility in chronic experiments in mice [42]. Based on our histology study targeting astrocyte (GFAP staining) evolution and neuronal survival after 80 days of implantation, on average, there was no significant difference in the average number of cell nuclei below the implant, while the difference in fluorescence intensity of astrocyte markers showed a mild scar evolution.

Building on the advantages outlined above, our study utilizes a custom-designed ECoG device optimized for high-resolution cortical recordings. The transparent thiol-ene/acrylate-based micro-electrocorticography device with 31 channels was fabricated using standard microelectromechanical systems processes at Qualia Labs, Inc., and subsequently packaged at Pázmány Péter Catholic University. The fully transparent electrode array was designed for in vivo cortical recordings in mice, covering a $2.4 \times 32.4 \times 3\ mm$ area with 31 gold recording sites arranged symmetrically. The diameter of each site is 115 μm, with a spacing of 400 μm between them. The total thickness of the device is approximately 18 μm. These dimensions were chosen to optimise the acquisition of neural signals in the mouse brain, balancing recording sensitivity and spatial resolution. The 115 μm site diameter provides sufficient contact area to capture extracellular neural activity with a favourable signal-to-noise ratio while minimising tissue damage. The 400 μm spacing between sites enables distinct neural populations to be sampled with reduced crosstalk. This facilitates spatial mapping of neural activity across the cortical surface and creates an imaging window for two-photon imaging.

The device incorporates a softening thiol-ene/acrylate polymer substrate that becomes flexible at body temperature (37 °C), allowing it to conform to the brain surface and potentially reduce neuroimmune responses. Fabrication involved spin-coating thiol-ene/acrylate layers onto a silicon handle wafer, with intermediate Parylene C encapsulation and photolithographic patterning of 400 nm gold traces for electrodes and wiring. In some devices, a 300 nm sputtered iridium oxide (SIROF) layer was added to the recording sites to improve electrochemical performance. After release from the wafer, the arrays were mounted onto Omnetics through-hole connectors using conductive epoxy and sealed with insulating adhesive.

Further details of the material synthesis and microfabrication processes are available in previous publications [60], [109]. Figure 3.3b shows the implanted SMP microECoG under a microscope.

The microECoG device used in this study was developed in collaboration with Qualia

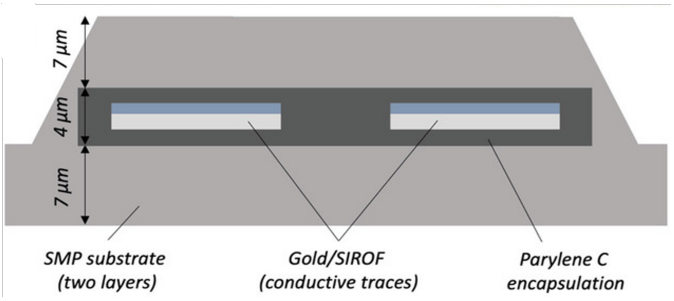

Figure 3.2: Schematic figure, showing the cross-section of the device. Source: [42].

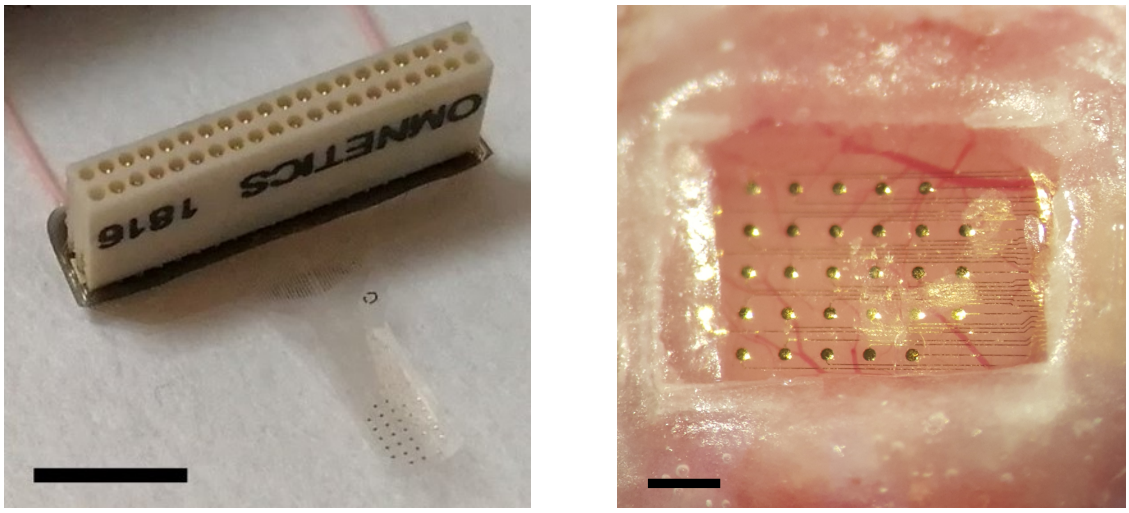

(a) (b)

Figure 3.3: Photo of the SMP microECoG. A) Image of the ready-assembled SMP microECoG with connector attached. Scale bar is 5 *mm* B) Photo of the implanted SMP microECoG. Scale bar is 1 *mm*.

Labs by the Research Group for Implantable Microsystems. Qualia Labs carried out the microfabrication, while the Research Group for Implantable Microsystems performed the device packaging at Pázmány Péter Catholic University. Electrochemical and biocompatibility characterisations were conducted jointly at Pázmány Péter Catholic University and Femtonics Ltd. My role in the project was to perform the optical characterisation and long-term spike detection phases solely. Specifically, I analysed bead-based optical measurements, *in vitro* dendrite detection, and *in vivo* relative intensity changes. I also conducted data analysis for long-term spike detection.

3.2 Animal surgery

For the INS acute *in vivo* experiments were performed on adult Wistar rats ($n = 8$; 5 females). The induction of anesthesia was achieved by administering an intraperitoneal injection of ketamine and xylazine, thus ensuring a stable physiological state optimal for the subsequent electrophysiological recordings. Following the induction of anesthesia, a craniotomy was performed to expose the cortical surface, with the size of the craniotomy varying according to the specific experimental condition. Next, for four animals, a cranial

window with a size of about 10 $mm \times 5$ mm was drilled over the left brain hemisphere. For the other four animals, a smaller craniotomy with a size of 3 $mm \times 3$ mm was prepared. The use of different craniotomy sizes was necessary because, in a subset of experiments, a flexible polyimide-based microelectrocorticogram array was implanted onto the exposed brain surface to capture electrophysiological signals over a larger cortical area, which was part of a parallel study investigating neural dynamics in the somatosensory cortex.

For infrared neural stimulation, a silicon-based optical probe [97] was inserted into the brain tissue at a depth of 1.2 mm, positioning the probe tip within the lower portion of cortical layer 5. Since infragranular layers, particularly layer 5b, exhibit the highest activity in the chosen anesthesia model [110], this region was selected as the primary target for infrared stimulation. Stimulation was applied to either the somatosensory cortex (n=6) or the association cortex (n=2), with the stimulation site centered within the exposed craniotomy. To record neural responses with high spatial resolution, a single-shank Neuropixels 1.0 silicon probe (IMEC, Leuven, Belgium) was inserted into the brain tissue adjacent to the optrode, maintaining an approximate lateral distance of $200 - 500$ μm. The probe was inserted to a depth of $3 - 4$ mm, enabling simultaneous recordings across multiple cortical layers, including the deep layers where the effects of infrared stimulation were anticipated to be most prominent. The experimental setup is illustrated in Figure 4.1A.

To implant the SMP ECoG device, adult male C57BL/6J mice (n=3) were used. Each mouse underwent cortical microinjections of AAV1.Dlx-GCaMP6f, followed by the surgical placement of a microECoG array over its somatosensory cortex. Under anesthesia, the mice's scalps were removed, and their skulls were cleaned in preparation for surgery. A craniotomy measuring approximately 2.6×3.2 mm was made above the somatosensory cortex at the following coordinates: 1: [-1.6, -2.0] and 2: [-2.4, -2.0] using a 0.3-mm drill bit. After opening the skull and carefully removing the dura, the flexible microECoG device was positioned directly on the cortical surface. To maintain the array's position and protect the brain, two custom-shaped glass coverslips were utilized: one with dimensions small enough to fit within the craniotomy and another with dimensions slightly larger to overlap its edges. Before the surgical procedure, the coverslips were adhered to each other using an optical adhesive, facilitating their seamless integration. The device, reference electrode (positioned above the cerebellum), and connector were secured using a quick-setting adhesive and dental cement. A headbar was attached just in front of the craniotomy to allow for future head-fixation during recordings. The experimental protocol was implemented only after a minimum of five days had elapsed, allowing the mice to recover from any potential stressors or injuries.

To investigate the long-term spiking activity with the SMP ECoG devices, transgenic adult mice (16–54 weeks old) of both sexes (n = 4 males, n = 3 females) expressing GCaMP6 were used. The surgical procedure followed a previously described method with slight modifications. A 3 mm craniotomy was made above the hippocampus, and the overlying cortex was carefully removed. The thiol-ene/acrylate microelectrode device

was then carefully positioned on the surface of the hippocampus and secured using a custom-made deep brain adapter, consisting of a silicone cylinder.

It is important to note that I did not take part in any of the surgical procedures involved in this study. My role was limited to the analysis and interpretation of the data.

3.3 Optical stimulation

The infrared stimulation was performed by using a sharp tip, multimodal photonic optrode device detailed in our previous work [97]. This multimodal photonic optrode has a 5 mm long shank with a 0.2 $mm \times 0.2$ mm rectangular cross section ending in a symmetrical 30° pointed sharp tip. Optrodes were calibrated before the *in vivo* experiments to quantify the output power at the optrode tip and the estimated temperature change (Figure 4.1C-D and Figure 3.4). To measure the spatial distribution of the IR-induced heating, the sharp tip optrode, and a platinum temperature sensor were simultaneously immersed in a 2 ml polyethylene cylinder filled with water. Temperature measurement was made in various spatial locations around the optrode's tip with 100 μm spatial resolution along two axes, perpendicular (Figure 4.1C) and along the shaft (Figure 4.1D). More details of the setup can be found in our previous work [83]. The optical power of IR light at a wavelength of 1550 nm was controlled by a fiber-coupled laser diode with a maximum output power of 70 mW (LPSC-1550-FG105LCA-SMA, Thorlabs GmbH, Germany). The choice of wavelength was based on our previous studies [83], [97]. The stimulation cycle was composed of 4-minute long ON (laser diode switched on), and 4-minute long OFF (diode switched off) periods to allow sufficient time for the temperature of the stimulated region to return to baseline temperature (Figure 3.5). Given the low power output, long exposure times are not critical, as they will not substantially damage the neural tissue. In our previous work [97], we performed histological analysis on cortical tissue subjected to a similar stimulation pattern. This analysis confirmed that repeated use of these stimulation parameters did not significantly affect the number of cells along the cortical column. Both continuous wave (CW) and pulsed IR illumination were tested. Pulsed IR stimulation cycles included the following frequencies: 1 Hz, 10 Hz, 50 Hz, 100 Hz, and 500 Hz. The different illumination types (pulsed IR stimulation with different frequencies and continuous IR stimulation) were presented in a random order. To check the reproducibility of the stimulation patterns in the electrophysiological traces, 5 trials were consecutively performed for each illumination type. The driving current of the IR laser diode (400 mA in each case) was supplied by a Keithley 2611B SYSTEM SourceMeter (Keithley Instruments Inc, OH, USA). Each onset of the laser diode was synchronized with trigger signals generated by the same Keithley instrument. The change in the temperature of the surrounding medium upon IR exposure was characterized using a calibrated platinum temperature sensor in an *in vitro* model detailed in our previous work (Table 3.1).

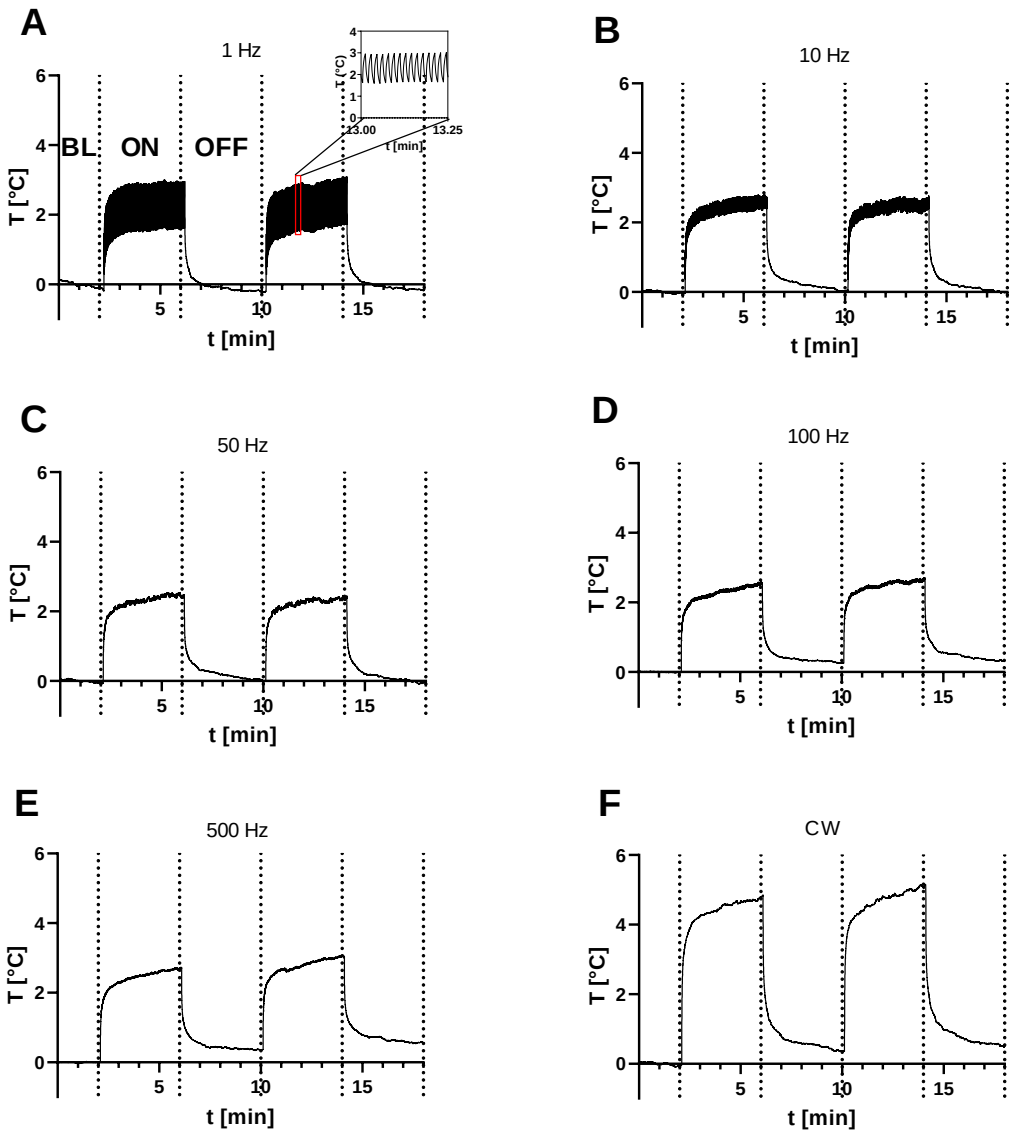

Figure 3.4: Changes in the temperature of the cortical tissue during infrared stimulation at each stimulating frequency. A) 1 Hz. A 15-second interval is enlarged to display the data with higher resolution. B) 10 Hz C) 50 Hz D) 100 Hz E) 500 Hz F) CW stimulation [J1].

Stimulation frequency	Maximum temperature change [°C]
1 Hz	3.10
10 Hz	2.82
50 Hz	2.56
100 Hz	2.71
500 Hz	3.09
CW	5.16

Table 3.1: Maximum temperature change compared to baseline temperature during different stimulation frequencies

Figure 3.5: Stimulation cycle. BL: baseline; ON: IR light on; OFF: IR light off

3.4 Electrophisiology

As outlined in section 1.1.2, the neural signals we record originate from ionic currents carried by sodium (Na^+), potassium (K^+), calcium (Ca^{2+}), and chloride (Cl^-) ions crossing neuronal membranes [111]. Electrodes play a crucial role in this process, as they must efficiently conduct neural signals while minimizing impedance and external noise. Impedance refers to the opposition to electrical current flow in an alternating current (AC) circuit and is influenced by both resistance and reactance [112]. In neural recordings, lower impedance is generally desirable, as it improves signal quality by reducing signal loss and thermal noise. The impedance of an electrode depends on factors such as its material, surface area, and frequency, with smaller electrodes generally having higher impedance. Because neural signals are extremely small, they require amplification before further processing. Amplifiers increase signal strength while preserving a high signal-to-noise ratio (SNR). Additionally, modern amplifiers often incorporate filters to remove unwanted noise, such as power line interference at 50/60 Hz. After amplification and filtering, the signals are digitized and transmitted to a data acquisition system, where they can be visualized as waveforms on a monitor or further analyzed.

For the INS experiments, cortical electrical activity (both local field potentials and spiking activity) was collected using the Neuropixels recording system. The neural signals were recorded on 384 channels (selected from the total of 960 recording sites) at a sampling rate of 30 kHz/channel for spiking activity and 2.5 kHz/channel for local field potentials, and with a resolution of 10 bit using the SpikeGLX software package (`https://billkarsh.github.io/SpikeGLX/`). The Neuropixels probe has a shaft with dimensions of 70 $\mu m \times 24$ μm and a length of 10 mm. The Nuropixels probe features 960 staggered electrodes, which are densely arranged along the shaft. The inter-electrode distance is 16 μm between columns and 20 μm between rows, with each electrode site measuring 12 $\mu m \times 12$ μm [113]. Only the first 384 recording sites of the probe (located closest to the probe tip) were used for data acquisition. To collect wideband (0.1–7500 Hz) neural activity with the recording sites of the optrode, we used an Intan RHD-2000 electrophysiological recording system (Intan Technologies, Los Angeles, CA, USA). Recordings were acquired with a 32-channel (headstage) at a sampling frequency of 20 kHz/channel and a resolution of 16 bit. Neuropixels probe and optrode recordings were collected simultaneously. Only the Neuropixels recordings were analyzed in this study.

During the SMP microECoG experiments, the electrophysiological signals were recorded using the RHD2132 amplifier board (Intan Technologies) with a bandwidth range of 0.1 Hz to 7.5 kHz and a sampling rate of 20 kHz.

3.5 Two-photon imaging

Two-photon microscopy is a laser-scanning technique that utilizes the absorption of two photons at once to excite fluorescence, thereby facilitating deeper tissue imaging with reduced phototoxicity and enhanced spatial resolution [114], [115]. In comparison to confocal microscopy, it provides enhanced imaging depth and reduced scattering, rendering it optimal for in vivo imaging of living cells and tissues. The quadratic dependence on excitation intensity necessitates the utilization of pulsed lasers with high photon flux for effective imaging. Two-photon calcium imaging is a technique that utilizes fluorescent Ca^{2+} indicators to monitor neural activity *in vivo*. Calcium influx through voltage-gated channels has been identified as a pivotal signal in neuronal communication, plasticity, and gene expression [116], [117]. Calcium imaging captures these dynamics with high temporal and spatial resolution, enabling real-time observation of neuronal processes across multiple time scales.

To evaluate the optical properties of the SMP microECoG, two-photon imaging was performed at 910 nm using a Femto2D-DualScanhead two-photon microscope (Femtonics Ltd.) in resonant and galvanic scanning modes. Image acquisition and storage were performed using MATLAB-based MES software (Femtonics Ltd.), while I performed data analysis using custom MATLAB scripts and algorithms.

Fluorescent microbeads were used to evaluate the influence of micro-ECoG on two-photon imaging. These beads were enclosed between glass slides to ensure that the same 6 μm nominal size beads remained in focus under all imaging conditions.

Three Thy1-GCaMP6f transgenic mice (aged 22, 23 and 103 days) were used for in vitro optical characterization. Horizontal hippocampal slices (350 μm thick) were prepared according to previously established protocols [98]. Slices were continuously perfused with artificial cerebrospinal fluid (aCSF) and oxygenated. Images of hippocampal regions were acquired both with and without the SMP microECoG in place and then processed using a custom algorithm.

3.6 Data analysis

3.6.1 Spike sorting and curation

Spikes, or action potentials, are rapid voltage fluctuations generated by neurons to transmit information. These all-or-none events, driven primarily by sodium (Na^+) currents, produce the strongest transmembrane currents and are detected as high-frequency signals in extracellular recordings [118]. The sampling rate of electrodes is a critical factor in capturing neural activity with high temporal resolution. For extracellular recordings of action potentials, a sampling rate of 20–30 kHz is generally considered sufficient due to the Nyquist theorem [119], which states that a signal must be sampled at least twice its highest frequency component to avoid aliasing. Spikes typically contain frequency components up to 5-10 kHz, so a 20–30 kHz sampling rate ensures accurate waveform reconstruction

while minimizing data storage and processing demands. Lower sampling rates can lead to aliasing and distortions, making spike sorting less reliable, while significantly higher rates provide diminishing returns in spike resolution. The process of recording and processing spikes in neural signals involves several key steps. First, the recorded data is filtered using high-pass filters to extract the spikes. The filtered signal captures the activity of multiple neurons simultaneously, so it is crucial to distinguish and identify the spikes from different neurons. The spikes from each neuron recorded from a particular electrode have a distinctive shape that is influenced by factors such as the morphology of the dendritic tree, the relative position and orientation of the neuron to the electrode, the distribution of ion channels, and the characteristics of the extracellular environment [120]. These spikes are organized into clusters based on their shape in a process called spike sorting. The basic steps of spike sorting is shown in Figure 3.6.

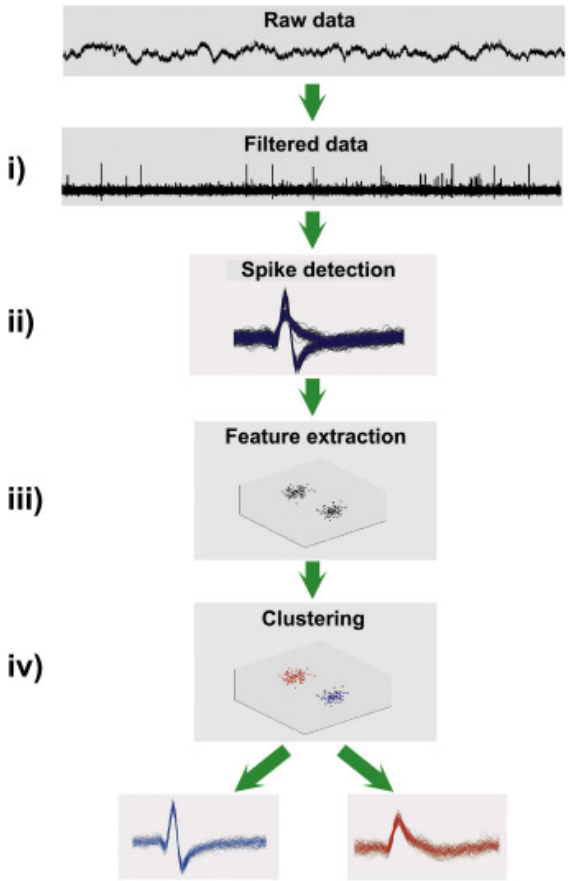

Figure 3.6: Steps of spike sorting. (i) Bandpass-filtered data. (ii) Spike detection (iii) Feature extraction for dimension reduction. (iv) Clustering of the spikes into single units. Source: [121].

Once sorted, each cluster is assigned to a single neuron. However, in cases of poor signal-to-noise ratio, some clusters cannot be resolved, resulting in a multi-unit cluster of activity. This cluster represents a mixture of spikes from multiple neurons, characterized by a lower amplitude and a violation of the refractory period, where spikes can occur within a short time window (less than 2.5 ms). By combining extracellular recordings with spike sorting, we can isolate the activity of individual neurons from a few units per

electrode. This can be done over periods ranging from hours to months or even years.

To ensure standardisation of peak potential measurements across animals, we applied a consistent and well-controlled experimental and analytical pipeline. All recordings were performed under identical anesthesia protocols. Anesthesia was induced via an intraperitoneal injection of ketamine (75 mg/kg) and xylazine (10 mg/kg), then maintained with additional intramuscular doses of the same mixture. Anesthesia depth was carefully monitored using reflex testing, and recordings were only initiated once a stable anesthetic state was confirmed. This approach minimised variability in brain state, which could otherwise affect neuronal excitability or spike amplitude. Electrophysiological data were processed using an identical spike sorting pipeline for all animals. In our experiments, the spikes from the Neuropixels data were detected using KiloSort (v.3.0), a spike sorting algorithm [122]. which I run on an NVIDIA V100 GPU. Single units were then manually curated based on their auto-correlograms, cross-correlograms, firing rates, amplitude distributions, and spike waveform characteristics. Single units of substandard quality were excluded from further analysis based on quality metrics (presence ratio, interspike interval violation, amplitude cutoff) calculated with SpikeInterface (v.0.98.2) [123]. The presence ratio determines the proportion of recordings in which spikes are detected. A higher presence ratio value indicates better unit stability over time (range: 0-1, presence ratio $\geq$ 0.9 was used for our recordings). Interspike interval violations quantify the rate of refractory period violations, where lower numbers indicate less contamination by spikes from other clusters (ISI violation $\leq$ 2) [124]. The amplitude cutoff assesses the miss rate utilizing the amplitude histogram (range: 0-0.5, amplitude cutoff $\leq$ 0.01). Auto-correlograms and signal-to-noise ratio were analyzed using SpikeInterface along with custom Python and MATLAB scripts. The signal was defined as the maximum spike waveform amplitude, while noise was calculated as the standard deviation of background activity on the same channel. Figure 3.7 displays the quality metrics plots from the SMP microECoG experiments, used to filter the data. Waveform visualization was performed using Spikes (Cortex-lab) and MATLAB scripts, while firing rate, amplitude distribution, spike count, and real amplitudes were computed using custom MATLAB scripts.

3.6.2 Differentiation between cell types

In the neocortex, there are two primary neuron types: inhibitory interneurons and excitatory neurons (principal cells), distinguishable based on the duration of their extracellular action potential waveform [37]. Generally, spikes with a shorter duration reflect inhibitory interneurons, while longer spikes refer to principal cells. To identify these two neuron types in our recordings, I calculated the trough-to-peak time of the mean spike waveform for each single unit. As expected, the distribution of the trough-to-peak times was not unimodal and contained two peaks (Hartigan's dip test [125], $p = 4.608 \times 10^{-3}$), indicating significant bimodality. Since the bimodal distributions were slightly different between animals, the threshold for differentiating putative interneurons and principal cells was manually set for each animal based on the distribution of trough-to-peak times (Animal

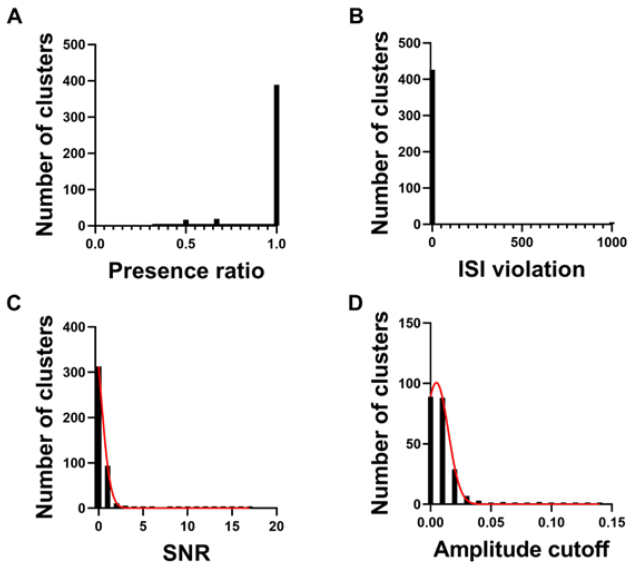

Figure 3.7: Quality metrics demonstrating sorting quality. Histogram of A) presence ratio, B) interspike interval violation (ISI), C) Signal-to-noise ratio, and D) amplitude cutoff. Gaussian nonlinear regression curves were fitted to the SNR and amplitude cutoff histograms to quantify the spike quality metrics. [J2].

1: threshold=0.61 ms, Animal 2: 0.58 ms, Animal 3: 0.42 ms, Animal 4: 0.48 ms, Animal 5: 0.43 ms, Animal 6: 0.53 ms, Animal 7: 0.44 ms, Animal 8: 0.41 ms). If the trough-to-peak time was longer than the threshold, the single unit was classified as a principal cell. If it was equal or shorter, it was classified as an interneuron.

For the experiments using SMP microECoGs, I additionally classified wide-spiking interneurons. In order to distinguish between the various cell types, putative pyramidal cells, narrow-spiking interneurons, and wide-spiking interneurons were classified based on two criteria: the trough-to-peak time of the waveform and the burstiness index (BI), which was calculated based on the autocorrelograms of the recorded single units. The threshold (1.2) for determining burstiness was set according to the literature [36].

3.6.3 Identification of the laminar location of single units

I determined the laminar position of the recording sites of the Neuropixels probe based on the registered cortical population activity and the Nissl-stained coronal brain sections containing the probe tracks. Layer 1 is a cell-sparse layer with only a few single units detected; therefore, I excluded these units from further analysis. Since the relatively thin nature of layers 2 and 4 led to increased uncertainty in delineating their boundaries, single units located in superficial and input layers (layers 2, 3, and 4) were grouped. Additionally, under anesthesia, superficial layers exhibit sparse spontaneous population activity with lower numbers of neurons firing compared to infragranular layers [126], [127]. The combined thickness of these three layers was approximately 650 μm. Layer 5, with a thickness of around 450 μm, contains the cell bodies of the largest pyramidal cells and displays the strongest neuronal activity under ketamine/xylazine anesthesia

[110]. Finally, layer 6 with smaller pyramidal cells has the largest extent ($\sim$ 600 μm thickness) but shows weaker firing activity compared to layer 5 [110]. The boundary between layer 6 and the white matter could be identified by a significant decrease in neuronal activity and the presence of short-duration spikes with a large positive peak, indicative of axonal activity [128]. Each recording site was assigned to one of the layer groups. After that, each single unit was assigned to the recording site (i.e., to a layer) where its mean spike waveform had been detected with the largest amplitude. To combine data from multiple animals, depth normalization was implemented to address differences in the labeling of recording channels between animals. This normalization procedure was based on established literature [129]–[131]. It involves measuring the distance from each recording site to the pial surface, then expressing this as a fraction of the total cortical thickness (pial surface to white matter), with 0 representing the surface and 1 the white matter boundary. My method extends this approach by incorporating the following steps: for each animal, I identify the channels where single units were detected, using the previously established channel labels that mark the borders of each cortical layer. Each layer was then normalized to a range between 0 and 1. A value of 1 was added to the layer 5 channels to ensure an accurate representation of relative depths, while a value of 2 was added to the superficial and input layers. This resulted in a depth scale ranging from 0 to 3, with depth decreasing. This method was necessary because the channels with detected single units were irregularly spaced and varied across animals, requiring a flexible normalization approach that accurately preserves laminar boundaries and relative depths despite discontinuous sampling. For visualization purposes, these values were further normalized between 0 and 1, with 0 representing the deepest channel and 1 representing the most superficial channel to help the graphical representation of depth information. The method is illustrated in Figure 3.8.

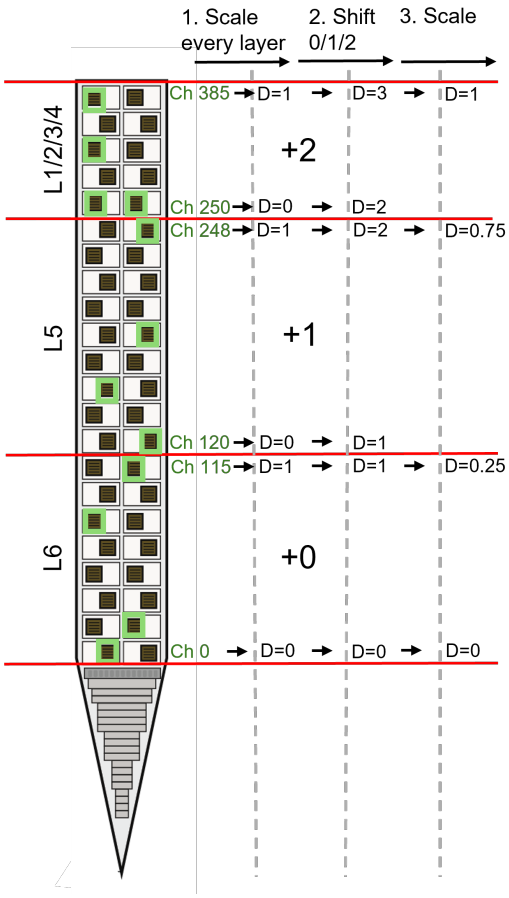

Figure 3.8: Example of the depth normalization method. The channels on the Neuropixels probe on which single units were detected are marked in green. (Ch: channel; D: depth; L1/2/3/4: superficial and input layers; L5: Layer 5; L6: Layer 6).

3.6.4 Firing rate analysis

For each single unit recorded during the INS measurements, the relative firing rate change compared to the baseline period was calculated in ten-second intervals for every ON period as shown in Equation 3.1.

$$RelativeFiringRate = \frac{FiringRate - Baseline}{Baseline} \tag{3.1}$$

The baseline firing rate was defined as the average firing rate during the last two minutes of OFF periods (spontaneous cortical activity) preceding the ON periods (IR stimulation-related activity). To ensure data quality, single units were also filtered based on the baseline firing rate. A threshold was set according to the distribution of baseline data. Specifically, the lower threshold was set as $10th\ percentile - 3 \times interpercentile\ range$, where the interpercentile range is calculated as the difference between the 90th and 10th percentiles. The upper threshold was defined similarly as $90th\ percentile + 3 \times interpercentile\ range$. The application of these thresholds allowed the exclusion of extreme values, with approximately 4 % ($n = 322$) of the data being identified and removed as outliers.

To examine the impact of stimulation, each single unit was classified based on the

relative firing rate change as having either suppressed, increased, or neutral activity (unaffected). This categorization was determined through the assessment of the degree of change in the firing rate. An empirical threshold was established to differentiate meaningful activity changes from noise. Specifically, a single unit was classified as excited (increased activity) if its firing rate increased more than 20% compared to the baseline during at least 60% of the ON periods, suppressed if its firing rate decreased by 20% or more, and unaffected if the firing rate fell within the range of −20% to 20%. The criterion of 60% was set based on the presence of five ON periods per experiment, ensuring that a majority of stimulation trials showed consistent modulation. Further examination revealed that unaffected neurons rarely exhibited conflicting responses (e.g., increased activity in two trials and suppressed activity in two others), with most showing three to five unaffected trials. This confirms the reliability of this classification approach.

As described before, to calculate the relative firing rate, the two-minute OFF periods were used as a baseline firing rate. However, it is also necessary to compare the results to longer spontaneous cortical activity, which is uninterrupted with IR stimulation. This serves as an important control measure for understanding the inherent variability in neuronal activity and ensuring that any observed changes during stimulation trials are indeed attributable to the stimulation protocol rather than natural fluctuations. For this purpose, 10 minutes of spontaneous activity were recorded in each animal before the stimulation session. From this dataset, five animals were selected as control data. The firing rates from the five controls, where no stimulation was applied, were also calculated. The firing rates of each unit were z-score normalized and then scaled between -1 and 1 to standardize and scale appropriately for analysis and presentation (Figure 3.9).

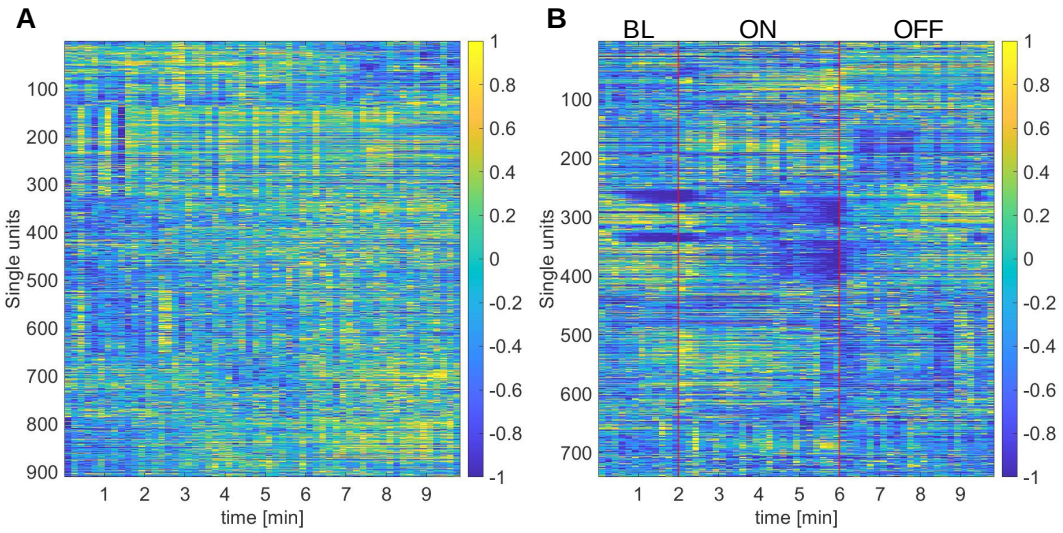

Figure 3.9: Colormaps of the normalized firing rate of all single units isolated from five rats when no stimulation was applied (A), and from the same five rats when the IR stimulation was applied (B) The beginning of the ON period is marked with vertical red lines [J1].

To examine the neuronal response time under different stimulation frequencies, I

measured the latency at which activity reached 90% of the firing rate change during the ON periods (rise time), and when it reached 10% of the firing rate change of the ON periods during the following OFF periods (fall time). Figure 3.10 illustrates the defined rise and fall times on two example single units, with one showing increased (Figure 3.10A), while the other displaying suppressed activity (Figure 3.10B).

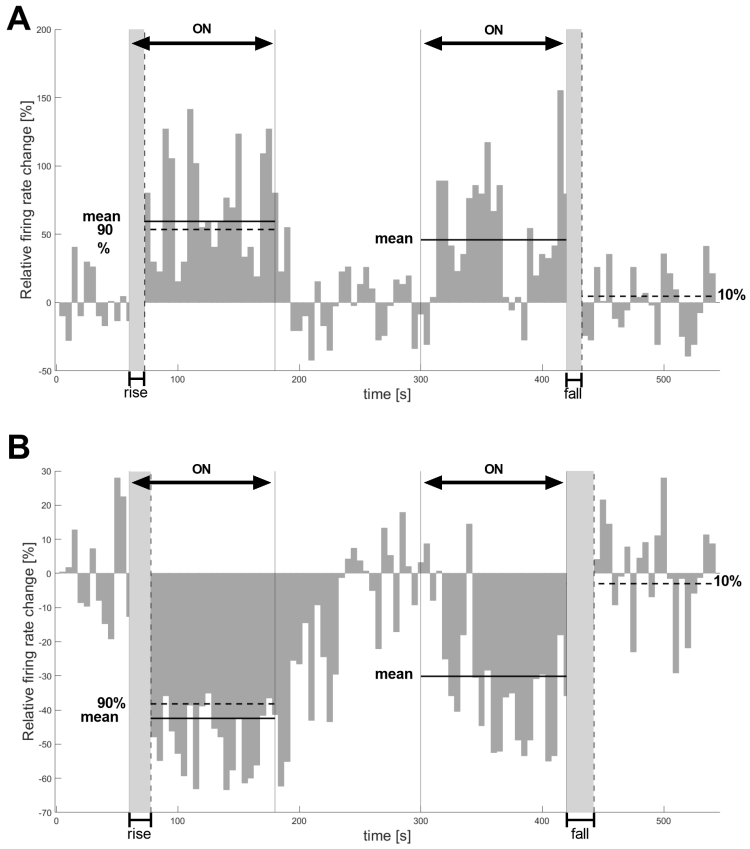

Figure 3.10: Method for determining rise time and fall time based on change in firing rate. A) Illustrative example of a single unit with increased activity during IR stimulation. Rise time is the interval during which the relative firing rate alteration reaches 90% of the average during the ON period. Fall time is the interval in which the relative firing rate change attains 10% of the mean from the prior ON period during the OFF period. B) Illustrative example of a single unit with suppressed activity during IR stimulation [J1].

3.6.5 Fluorescent bead measurements

An image can be defined as a two-dimensional function: $f(x, y)$, where x and y are coordinates, and f is the intensity value of the pixel in the coordinates. If the values are finite and discrete, the image is a digital image [132]. Preprocessing the images before other operations is an important step in image processing. With preprocessing, the wanted features can be enhanced, while the noises and unwanted features can be eliminated, and the image can be smoothed with mathematical models. Noise is unnecessary information in the images. Morphological processing adds a structuring element to the images [133]. It is used to extract shapes from the image. Morphological operations are, for example,

erosion, dilation, opening, and closing. Erosion is used to remove structures from the image, and dilation fills the holes, which are given by the structuring element. Image segmentation is a tool to partition the image into segments. Edge detection, thresholding on binary images, and statistical classification can be used for segmentation. The process mostly relies on the change of the intensity values in the image, using the common patterns to group the pixels based on their intensity values and their neighbors' intensity values. Usually, the objects are grouped into two groups: foreground and background pixels. Thresholding means the mapping of grayscale values between 0 and 1 as equation 3.2 shows.

$$S(x,y) = \begin{cases} 0 & \text{if } f(x,y) < T(x,y) \\ 1 & \text{if } f(x,y) \geq T(x,y) \end{cases} \tag{3.2}$$

where $S(x,y)$ is the segmented pixel value, $f(x,y)$ is the intensity value and $T(x,y)$ is the threshold value of the pixel at the coordinates (x,y). The threshold can be global, or it can be determined by an adaptive threshold algorithm based on the local neighborhood of the pixels.

For the analysis, two-photon microscopy images were acquired of fluorescent beads, with a nominal size of 6 μm in diameter. Two sets of images were obtained: one with the SMP microECoG and one without it. In the images taken with the SMP microECoG, the beads were positioned beneath the transparent electrode grid, and the imaging was performed through the SMP microECoG. I created MATLAB scripts to analyze these images, which will be explained in this section.

First, the images were divided into four overlapping tiles, and the fluorescence values were normalized to a range between 0 and 1 to improve detection accuracy. The segmentation approach varied depending on the mean intensity of each tile. If the mean intensity exceeded 0.1, adaptive thresholding was applied with a sensitivity value of 0.1. For tiles with a mean intensity of 0.1 or less, a global threshold was determined using Otsu's method.

Circular Hough Transform (CHT) [134] is then applied to identify the centers and radii of the beads. This step allows the precise localization of each bead within the image. I chose the Circular Hough Transform based on the geometric characteristics of the target features and the imaging conditions in my dataset. The structures I aimed to detect, such as microbeads, are circular and consistent in size, aligning well with the assumptions underlying the CHT. Furthermore, the images often exhibit low contrast and noise due to experimental constraints, which makes robust detection challenging. Of the various available methods, the CHT offers an appealing compromise: it can tolerate partial occlusion, uneven illumination, and blurred edges more effectively than contour-following or edge-linking approaches, which tend to malfunction in the presence of noise or incomplete boundaries. Although template matching can also detect shapes under such conditions, it is generally less flexible concerning radius variation and can be more computationally demanding for even modest size ranges. Crucially, my prior knowledge

of the approximate radius range enables us to apply the CHT in a constrained and computationally efficient manner. This targeted application minimises false detections while enhancing sensitivity to true circular features. In this context, CHT is not just a robust default, it is analytically justified given the shape priors, scale consistency, and signal-to-noise limitations inherent in the data.

The algorithm has three main steps:

1. Accumulator Array Computation
   The high gradient foreground pixels are candidate pixels that are allowed to cast 'votes' in the accumulation array. These pixels vote in a circular pattern around them with a fixed radius. Figure 3.11 shows a candidate pixel on an actual circle and the voting patterns of the candidate pixels.

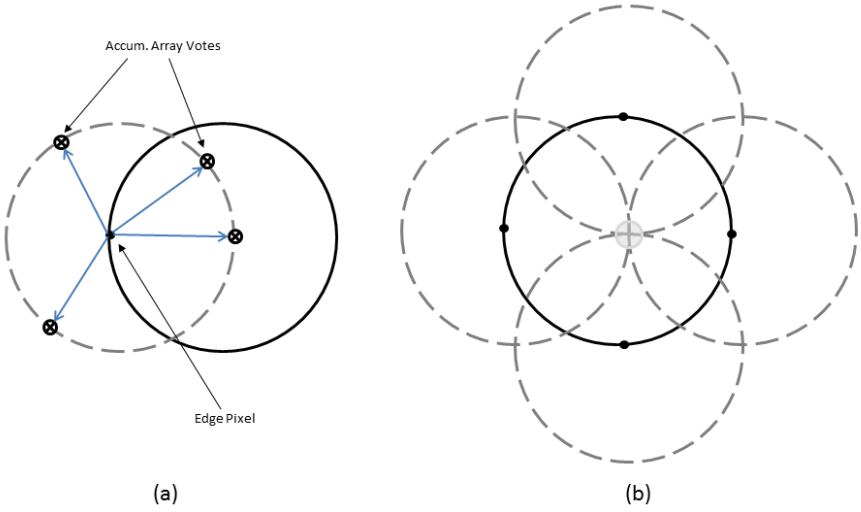

Figure 3.11: Accumulator Array Computation. A) The candidate pixels on an actual circle. B) The voting pattern is indicated by a dashed line. Source: [135].

2. Center Estimation
   The votes of the candidate pixels tend to accumulate at the array corresponding to the circle's center, so the centers are estimated by detecting the peaks in the array. Figure 3.11 (b) shows an estimated circle center by the vote patterns.

3. Radius Estimation
   Phase coding [136] for radius estimation utilizes complex values, with the radius information encoded in the phase of the array entries. The votes give information not only about the possible center but also about the radius of the circle associated with the location of the center. The radius can be estimated by simply decoding the phase information from the center location in the array.

The final step is statistical analysis. The MATLAB statistics function [137] is used to calculate key statistical measures, including mean diameter, interquartile range, mean absolute deviation, range, and standard deviation. These measurements provide insight into the distribution of bead sizes.

However, the accuracy of bead detection can be affected by shadows, reflections, and variations in intensity that may not be visible to the naked eye but are detected by the algorithm. In addition, due to the relatively small bead size compared to the image resolution, pixelation can distort their circular shape, making accurate center detection more difficult. As shown in Figure 3.12a, some inaccuracies arise from inconsistencies in intensity between different beads. As the algorithm relies on circular fitting, these pixelation effects affect the accuracy of the measurements. To minimize errors caused by outlier beads, the analysis was repeated exclusively on beads that were consistently detected in both images, those taken with (Figure 3.12c) and without the SMP microECoG (Figures 3.12b and 3.12d) in the light path. Fluorescence-related edge artefacts were further reduced by thresholding during image scaling. Figure 3.12e illustrates an example of overlapping beads, which the algorithm successfully detects.

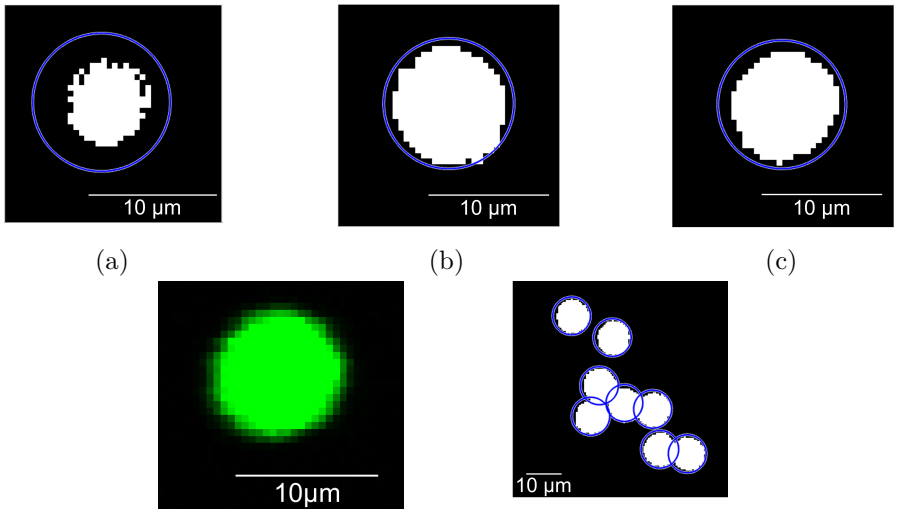

Figure 3.12: Examples of bead detection. A) Outlier beads, which were detected larger than their actual size. These outlier values were eliminated by repeating the measurement on only the same beads that were detected in both of the images. B) The same detected bead without the SMP microECoG. C) The same detected bead under the SMP microECoG. D) The same detected bead without the SMP microECoG in MES software. E) Beads near and on top of each other. The algorithm can successfully detect the overlapping beads.

To evaluate the performance capabilities of the CHT, two quantitative assessments were conducted: sensitivity to image noise and resilience to spatial overlap between circular features. These tests were designed to determine the practical limits of the reliability of the CHT in conditions reflective of real-world imaging scenarios. First, I evaluated the robustness of CHT to increasing levels of Gaussian noise. Starting with a clean grayscale image without the SMP micro ECoG from the experiment, I added Gaussian noise with variances ranging from 0 to 0.05. The centres of the beads were used as the ground truth. For each noise level, I used the algorithm to calculate standard performance metrics. Precision, which is the proportion of correctly detected circles relative to all detections, recall, the proportion of ground truth circles that were successfully detected, and detection

rate, or the number of detected circles divided by the ground truth count. I used a pixel-wise distance threshold of 5 to match the positions of the detected centres to the reference positions. Additionally, I estimated the inherent noise in the original experimental image by manually selecting a background region. The noise variance was computed from the coefficient of variation (CV), which normalises the standard deviation by the mean intensity, yielding a scale-independent noise estimate. The resulting curves (Figure 3.13A) demonstrate a rapid decline in precision and recall as the noise level increases. The detection rate is also increasing with the noise, which means that more circles were found than the ground thruth. Notably, the estimated noise variance of the original experimental image (0.0007) falls just before the inflection point of this deterioration, where precision and recall begin to decline. This suggests that while the inherent noise level in the data is relatively low and does not significantly impair circle detection, further increases would reduce accuracy. These findings emphasize the importance of maintaining low noise levels or applying denoising filters before executing CHT-based detection on experimental images. As illustrated in Figure 3.13B, the detection rate remains 100 % when the circles are overlapped by maximum 90% of their diameter. However, performance deteriorates rapidly beyond 90% overlap, revealing that the CHT has a limited ability to resolve tightly clustered or touching circular features. This limitation arises from CHT's reliance on edge continuity and geometric symmetry, both of which become ambiguous in the presence of significant overlap.

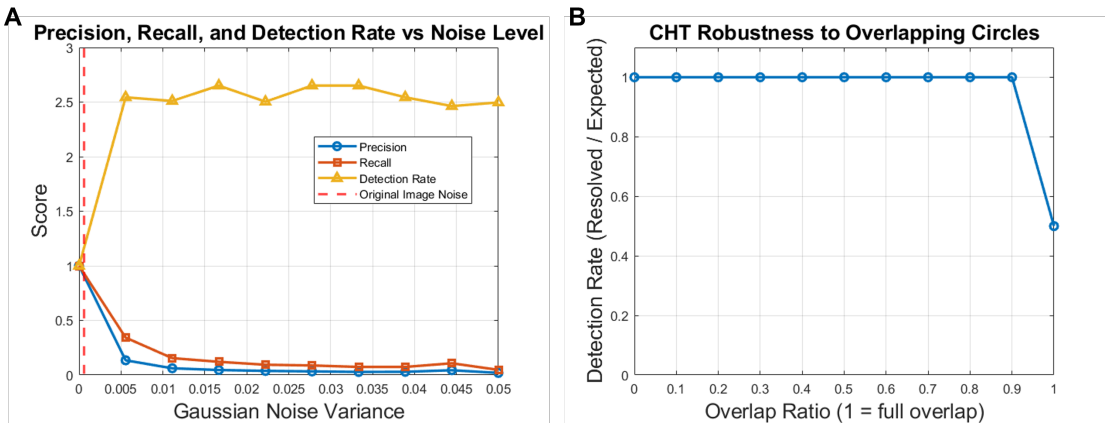

Figure 3.13: Limitations of Circular Hough Transform. A) Precision, recall, and detection rate of the CHT as a function of Gaussian noise variance. The original image noise is around 0.0007 (red line). B) CHT detection rate as a function of overlap ratio between two synthetic circles.

3.6.6 Measuring dendrites of neurons

The *in vitro* images were taken of the hippocampus of a Thy1-GCaMp6f transgenic mouse. Figure 3.14 shows a two-photon microscopy image taken of the hippocampal area. The cell bodies and the dendrites are visible.

I analyzed these images using a custom MATLAB script and calculated statistics from the results. The algorithm's first step involves cutting the images into overlapping tiles to improve detection accuracy, followed by applying Gaussian filtering. Gaussian filtering,

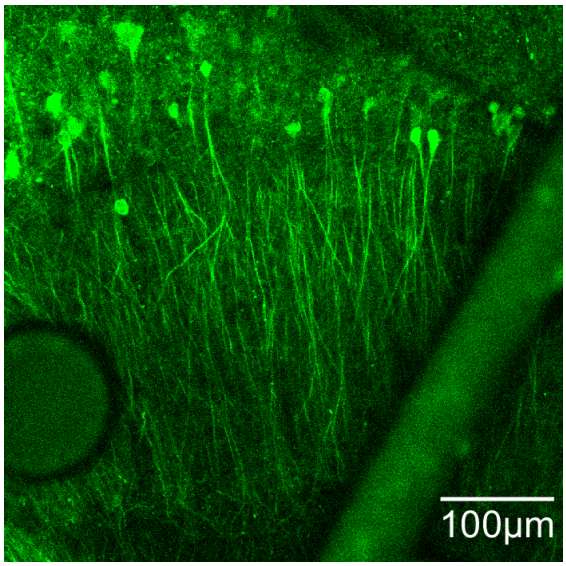

Figure 3.14: *In vitro* two-photon image taken of the dendrites of neurons. One of the recording sites is visible in the lower left corner of the image, while an electrode trace can be seen on the right side.

or Gaussian smoothing, is a linear filter used to blur images and reduce noise. Equation 3.3 shows the Gaussian function, where σ is the standard deviation of the distribution, which is assumed to have a mean of 0 [138].

$$G(x,y) = \frac{1}{\sqrt{2\pi\sigma^2}} e^{-\frac{x^2+y^2}{2\sigma^2}} \tag{3.3}$$

The selection criteria for the tested neurites were based on intensity and morphological features extracted from the images. Namely, after Gaussian filtering, a reference pixel intensity was manually selected to set an adaptive threshold for segmenting neurites. The next step is to apply morphological operations, which use a structuring element to process the image [139]. A key function used is *imclose*, which performs a morphological close. This operation consists of dilation followed by erosion. Dilatation assigns each pixel the maximum value of its neighborhood, increasing the visibility of objects and filling small gaps. Erosion, on the other hand, assigns each pixel the minimum value of its neighbors, helping to remove small artifacts and isolated structures. These operations are essential for dealing with intensity variations in dendrites, ensuring that darker regions are recognized as part of the structure rather than being overlooked.

A watershed algorithm was then applied to separate the detected objects. dendrites were automatically identified based on their circularity, calculated using the circularity field of the *regionprops* function. An object was classified as a dendrite if its circularity value was below the threshold of 0.1. After detection, the identified objects from each tile were mapped back to their original coordinates in the full image, and duplicate detections were removed.

After morphological processing, connected components (i.e. objects) were extracted by filtering them based on an area range of 50–1000 pixels to exclude dendrites and other objects that were too small or large.

Once the dendrites had been identified, the minor axes were determined by matching the normalised second central moments of the detected regions. This method measures diameters via the length of the minor axes of fitted ellipses. Finally, pixel-to-micron conversion was used to accurately measure dendrite diameters.

Although the current algorithm offers a systematic method of estimating neurite diameters, several limitations must be recognised. Firstly, diameters are measured at a single representative point per segmented neurite using the minor axis length of fitted ellipses. This approach does not capture local diameter variations along the dendrite, which may be biologically significant. Secondly, although the size and roundness thresholds used to filter objects are effective at excluding noise and non-neuritic structures, they may also exclude thin or irregularly shaped dendrites, which could bias the sample. Thirdly, manually selecting the reference pixel intensity for thresholding introduces variability dependent on the user and may affect the consistency of segmentation across images. Finally, image quality factors such as contrast and noise levels may influence the algorithm's performance.

In order to critically assess the robustness and limitations of the dendrite width measurement algorithm, I conducted a sensitivity analysis in which I varied key elements of the workflow that depend on the user and the parameters. Specifically, I simulated three different reference pixel selections to approximate inter-user variability. For each of these selections, I applied three distinct areas and three roundness thresholds, resulting in 27 parameter combinations in total. I then quantified the number of segmented objects, the mean dendrite width (based on the minor axis length of fitted ellipses), and the standard deviation for each configuration.

The analysis revealed that the estimated mean dendrite width is moderately sensitive to the intensity of the reference pixel chosen and to the area threshold used during segmentation (Figure 3.15). At the lowest area threshold setting (50–500 pixels), Reference Pixel 3 yielded the largest mean diameter, followed by Reference Pixel 1, then Reference Pixel 2. This pattern persisted at the intermediate threshold (50–1,000 pixels), although mean values remained relatively stable across references. However, at the highest threshold (50–2,000 pixels), all three conditions showed an increase in mean diameter, with Reference Pixel 3 exhibiting the most pronounced rise again. Across all thresholds, the standard deviation also increased, reflecting growing variability in segmented object sizes as inclusion criteria became less restrictive. In addition, increasing the roundness threshold enabled more rounded objects to be included in the analysis (Figure 3.15B). Since smaller structures tend to be more circular, this resulted in a decrease in the measured mean dendrite width as these smaller, rounder objects were added to the segmented population. Conversely, stricter roundness thresholds excluded more circular structures, focusing the analysis on elongated, irregularly shaped dendrites. This illustrates the direct impact of shape-based filtering on dendrite width estimates and emphasises the importance of carefully adjusting the roundness threshold to balance the inclusion of relevant structures with the exclusion of noise or non-dendritic features.

These results demonstrate that both segmentation parameters and initial thresholding

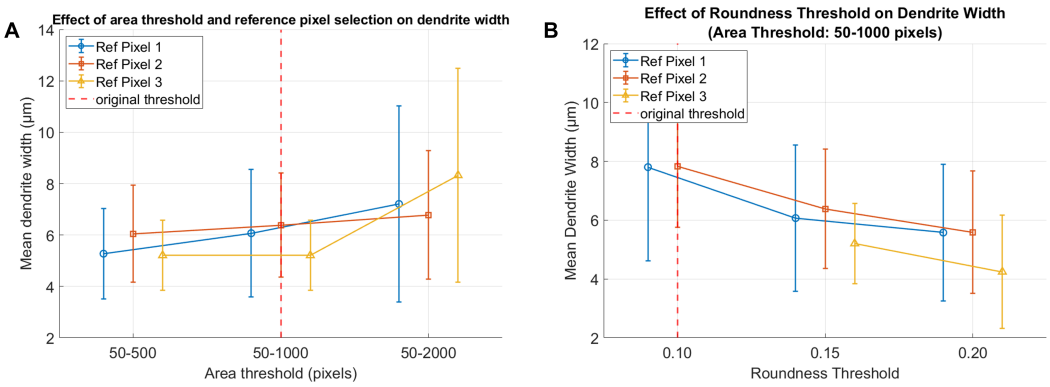

Figure 3.15: Sensitivity of mean dendrite width measurements to reference pixel selection, area thresholding, and roundness threshold. A) The mean dendrite widths (± standard deviation) for three simulated reference pixels are shown across three area threshold ranges (50–500, 50–1000, and 50–2000 pixels). B) Mean dendrite width for three simulated reference pixel selections (Ref Pixel 1–3) at increasing roundness thresholds (0.10, 0.15, 0.20), using a fixed area filter of 50–1000 pixels. For Ref pixel 3, there were no detected objects at 0.1 roundness threshold. Each line represents the results for one reference pixel. Error bars are horizontally offset for clarity. The red dashed line marks the original area threshold setting used.

conditions influence estimates of dendrite width and contribute to measurement variability. This highlights the importance of applying consistent criteria, especially in comparative analyses, and suggests that inter-user selection can introduce bias if it is not standardised or automated. While the current method offers a structured and reproducible way of quantifying dendrite width, it does have inherent limitations. Notably, using a single diameter estimate per object (via the minor axis of an ellipse) may oversimplify dendritic morphology, which can vary substantially along a single process. Future enhancements could include measuring diameter profiles along neurites, integrating skeleton-based morphology metrics or using semi-automated tools for reference pixel selection to minimise user variability.

3.6.7 Relative fluorescent intensity change measurements

In vivo resonance scanning measurements lasting between 3 and 10 minutes were recorded using MESc (Femtonics Ltd) from three freely moving adult mice, and analyzed using MES and MATLAB. Images were acquired from the somatosensory cortex of a mouse in which the GCaMP indicator was expressed in interneurons. These images were obtained using a thiol-ene/acrylate-based ECoG array implanted on the brain surface, directly in the optical path. As a result, cells appeared beneath the transparent electrode grid (Figure 3.16).

As the size of cell bodies varies at different z-planes and depends on cell orientation, comparing their dimensions does not provide an accurate assessment of the optical resolution of the SMP microECoG. Instead, the resolution and distortion effects of the long-term implanted SMP microECoG can be better assessed by analyzing changes in

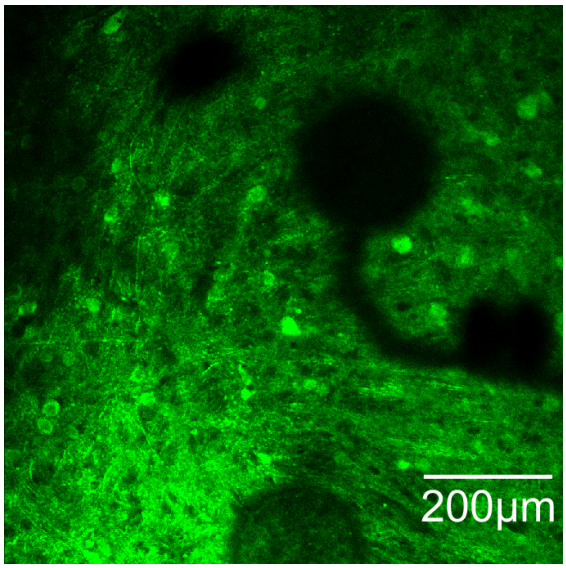

Figure 3.16: Image taken with the SMP microECoG placed in the light path. The shadows of the recording sites are visible.

the relative fluorescence intensity of cell bodies in *in vivo* images.

During data collection, resonant two-photon microscopy recordings were performed for 3-10 minutes. Frames from these recordings were averaged to generate images for segmentation. The segmentation algorithm was based on the same approach used to compare dendrite diameters in *in vitro* images (Section 3.6.6). Cell bodies were detected automatically by evaluating the roundness of the objects, using a threshold of 0.4 to exclude protrusions and noise. The detected cells were used as regions of interest (ROI) to extract cellular calcium activity. To visualize cell activity, the raw fluorescence signals from the ROIs were smoothed with a Gaussian filter ($\sigma = 5$) and converted into relative fluorescence changes as follows

$$\delta F = \frac{f - f_0}{f_0} \tag{3.4}$$

where f_0 is the fluorescent signal and f is the mean intensity value of the cell bodies. The background fluorescent value was determined for each image by finding the lower 8th percentile of the image.

Results were visualized using boxplot figures, where the whiskers represent the 5th and 95th percentiles, outliers are indicated by the $\diamond$ symbol, and the mean is shown as $\square$. All figures were produced using OriginPro.

3.6.8 Method for evaluating the long-term single unit activity with the SMP microECoG

Concurrent two-photon imaging and LFP recordings were performed utilizing an acousto-optical microscope (FEMTO3D Atlas Plug & Play, Femtonics), with the mice being positioned on a custom-designed linear treadmill. The focus of this section of the dissertation will be on spike analysis, obtained from the thiol-ene/acrylate microECoG

device. Figure 3.17 shows the schematic figure of the setup.

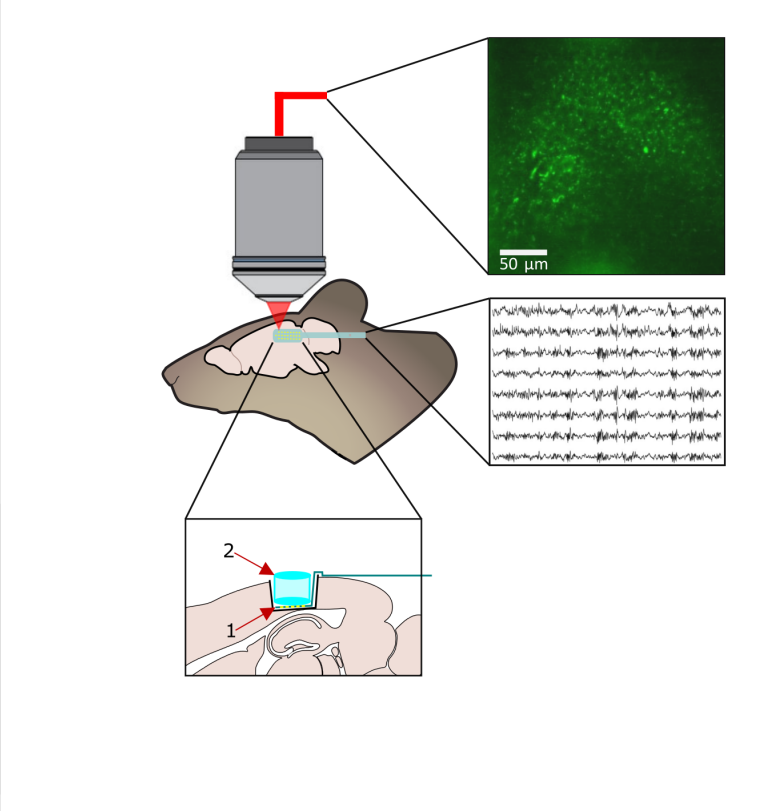

Figure 3.17: Schematic figure of the setup used for measuring Ca^{2+} signals with two-photon microscopy, alongside simultaneous electrophysiological recordings from the hippocampus. The ECoG is placed in the light path of the two-photon microscope. (1: ECoG device; 2: silicone cylinder)[J2]

3.6.9 Statistics

All statistical analyses were executed with a significance threshold of $alpha = 0.05$. Figure 3.18 shows the decision tree for selecting an appropriate statistical test. Briefly, prior to hypothesis testing, the distribution of each dataset was assessed for normality and log-normality. The analysis incorporated the D'Agostino-Pearson omnibus test and the Shapiro-Wilk test. Furthermore, a visual inspection of probability plots (Q-Q plots) was conducted to further evaluate distribution characteristics. For normally distributed data, parametric tests were applied. In cases involving the comparison of more than two groups, a one-way analysis of variance (ANOVA) was employed. In instances where the ANOVA model indicated a significant effect, post hoc tests were implemented to identify specific group differences. Dunnett's test was used when comparing experimental groups to a control, and Tukey's test was used when making pairwise comparisons among all groups. Both tests control the family-wise error rate (FWER), and multiplicity-adjusted p-values are reported.

In cases where the data did not meet the normality assumptions, non-parametric alternatives were employed. The Kruskal-Wallis test was employed to facilitate comparisons

across multiple groups. Following the attainment of a substantial Kruskal-Wallis result, Dunn's test was employed for the purpose of post hoc comparisons. Adjusted p-values were reported for all comparisons to account for multiple testing, using Bonferroni-style corrections as implemented in Prism.

For pairwise comparisons, Student's t-tests were employed for normally distributed data, while paired t-tests were utilized to compare bead diameters and two-sample (unpaired) t-tests were employed to compare dendritic diameters. Both analyses were conducted using OriginPro (OriginLab). Non-parametric paired comparisons were executed using the Mann-Whitney U test when applicable.

All statistical analyses involving group comparisons and post hoc tests were carried out using GraphPad Prism (v9.5.1).

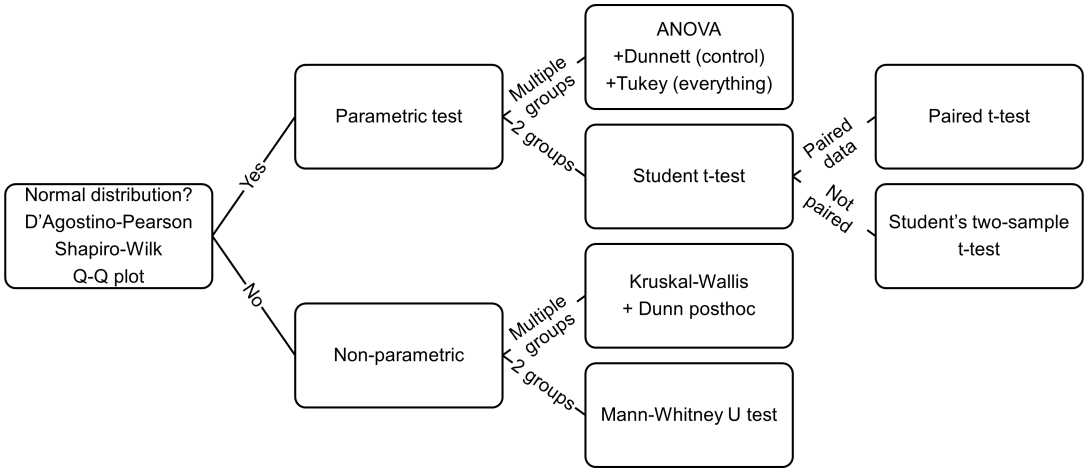

Figure 3.18: Decision tree for selecting appropriate statistical tests based on data characteristics and study design.

4 Results

The findings presented here are the result of my own research and analysis and represent my contribution to this dissertation. The scope of my role entailed the entire workflow, which included the processing of raw data, the execution of statistical analyses, the development of customized scripts, and the generation of the final figures and visual representations, as well as the discussion of the outcomes.

4.1 Results related to the INS experiments

4.1.1 Frequency-dependent effects of infrared stimulation on spontaneous activity of the neocortex

To investigate the effects of infrared stimulation on cortical neurons in vivo, the activity of 7,549 single units was recorded from eight anesthetized rats during pulsed (1–500 Hz) and continuous wave stimulation. Infrared light (1550 nm) was delivered via a sharp-tip multimodal photonic optrode [97], and cortical activity was recorded with a Neuropixels probe positioned near the optrode (Figure 4.1A). Spike sorting was used to extract single-unit activity, and quality metrics were applied to exclude low-quality units.

Relative firing rate changes were computed for each unit based on a baseline period preceding IR stimulation. Figure 4.1B displays the normalized firing rate change of all single units in one of the rats during continuous infrared light stimulation. Approximately 30% of the single units showed no noticeable change in their activity ($n = 34/116$) in response to infrared stimulation, while a large proportion of neurons increased ($n = 48/116$) or decreased ($n = 34/116$) their firing rate. Figure 4.1E and Figure 4.1F show an example of a putative interneuron with suppressed activity originating from layer 5 and a pyramidal cell with increased activity from layer 6, respectively.

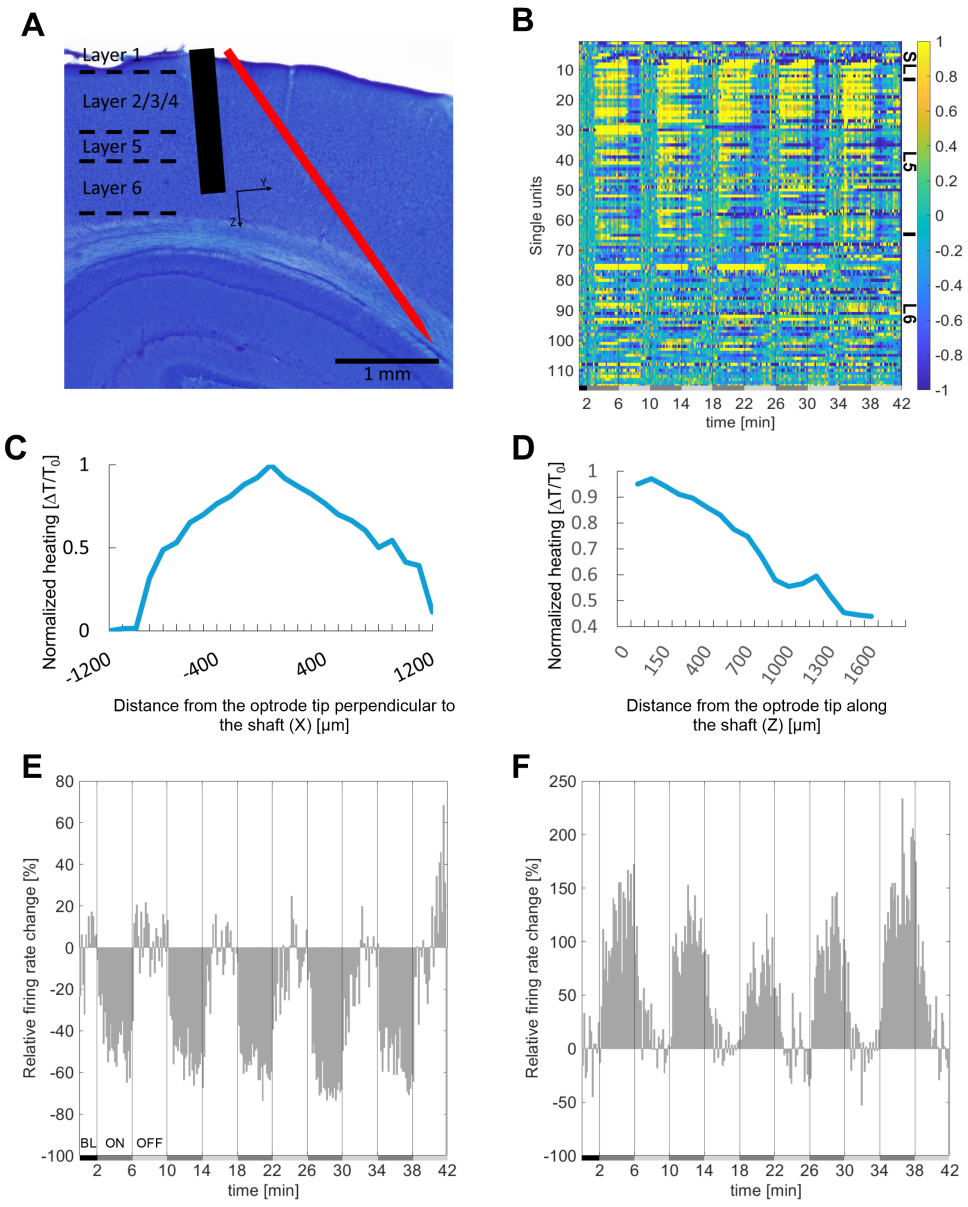

Figure 4.1: Experimantal setup and temperature-dependent firing rates. A) The experimental setup demonstrated on a sample Nissl-stained coronal brain section from the parietal association cortex (optrode: black; Neuropixels: red). The axes adjacent to the optrode tip indicate the orientation of the measurements presented in C-D). It should be noted that the x-axis is perpendicular to the paper. B) Colormap of the normalized relative firing rate change of all single units isolated from a representative rat during CW IR light stimulation protocol. The single units are ordered according to their cortical depth. The baseline and the ON and OFF periods are marked with horizontal bars (baseline: black; ON: dark gray; OFF: light gray). (SL, superficial and input cortical layers (layers 2/3/4); L5, layer 5; L6, layer 6.) C) Spatial distribution of the IR-induced heating under bench top calibration conditions. The temperature values are normalized to the maximum temperature change observed (0-no temperature change, 1-maximum temperature change). The temperature measurement was made along two axes, C) perpendicular D) and along the shaft. The same axes are shown in A), with the x-axis oriented perpendicular to the paper. E) Relative firing rate change of a putative layer 5 interneuron displaying suppressed activity F) and a putative layer 6 principal cell with increased activity during stimulation [J1].

Each single unit was classified as having either suppressed, increased, or unaffected activity in response to infrared light stimulation. Figure 4.2A illustrates the percentage of neurons falling into each category across different stimulation protocols. The firing rate of the majority of single units did not change markedly throughout the entirety of the infrared stimulation protocol, except when continuous wave stimulation was applied (Table 4.1). In cases where cells were affected, pulsed wave stimulation elicited a greater number of single units with increased activity compared to those with decreased activity. Conversely, continuous wave stimulation elicited a greater proportion of single units showing activity suppression. In addition, cortical temperature exhibited stimulation type-dependent changes (Figure 4.2B), with CW stimulation eliciting the most pronounced temperature change relative to baseline temperature. Figure 4.2C and D present the average change in firing rate for single units exhibiting either suppressed or increased activity. Single units that were activated by IR stimulation doubled their firing rates on average compared to the baseline firing rates, while suppressed units showed about a 40% decrease in their firing rates. Those single units, that increased their activity to stimulation exhibited significantly higher firing rate changes exposed to CW stimulation than to pulsed stimulation (1 Hz, 10 Hz, 50 Hz)(Kruskal-Wallis test: $p < 0.0001$). Single units with suppressed activity exhibited a significantly lower firing rate during CW stimulation in comparison to stimulation at frequencies of 1 Hz, 10 Hz, and 50 Hz (Kruskal-Wallis test: $p < 0.0001$)). Comparing Figure 4.2B, C, and D, it becomes apparent that the proportion of single units exhibiting decreased or increased activity aligns with the degree of temperature change induced by infrared light. Moreover, Figure 4.3 illustrates that the firing rate change of neurons closely tracks the temperature change.

	suppressed activity [%]	increased activity [%]	unaffected activity [%]
1 Hz	16.1	23.55	60.35
10 Hz	13.71	25.75	60.54
50 Hz	16.93	22.05	61.02
100 Hz	18.11	22.99	58.9
500 Hz	13.31	28.59	58.1
CW	33.56	27.89	38.55

Table 4.1: Percentage of single units with suppressed, increased, and unaffected activity at each stimulation frequency. Data are averaged across all Neuropixels channels and include recordings from all cortical layers. (CW, continuous wave).

When considering only whether single units were affected or unaffected, without distinguishing between increased or suppressed activity, there appears to be a difference in the proportion of affected neurons between lower (1-50 Hz) and higher (100 Hz, 500 Hz, and continuous wave) stimulation frequencies. Specifically, the proportion of affected units may decrease at the higher frequencies, suggesting a potential shift in cortical responsiveness as stimulation frequency increases (Figure 4.2E). During CW stimulation, the proportion of single units affected by IR stimulation was significantly higher than the proportion of unaffected neurons (one-way ANOVA: $p < 0.0001$). Additionally, the

proportion of affected cells was significantly higher during CW stimulation when compared to stimulation at frequencies of 1 Hz, 10 Hz, and 50 Hz (one-way ANOVA: $p < 0.0001$).

Examining the change in baseline firing rates during repeated trials of infrared stimulation is critical because establishing local baselines for each neuron, rather than a single global baseline, provides a more accurate assessment of how stimulation modifies neuronal activity levels over time. It is critical to assess whether neuronal excitability is modulated over time and whether repeated stimulation produces different effects based on protocol parameters. I calculated the local baseline firing rates by averaging the firing rates of each single unit during the last two minutes of each OFF period preceding the ON periods. The baseline firing rates gradually increased with consecutive stimulation trials, reaching a plateau around the fourth trial (Figure 4.2F) (see further examples in Figure 4.4).

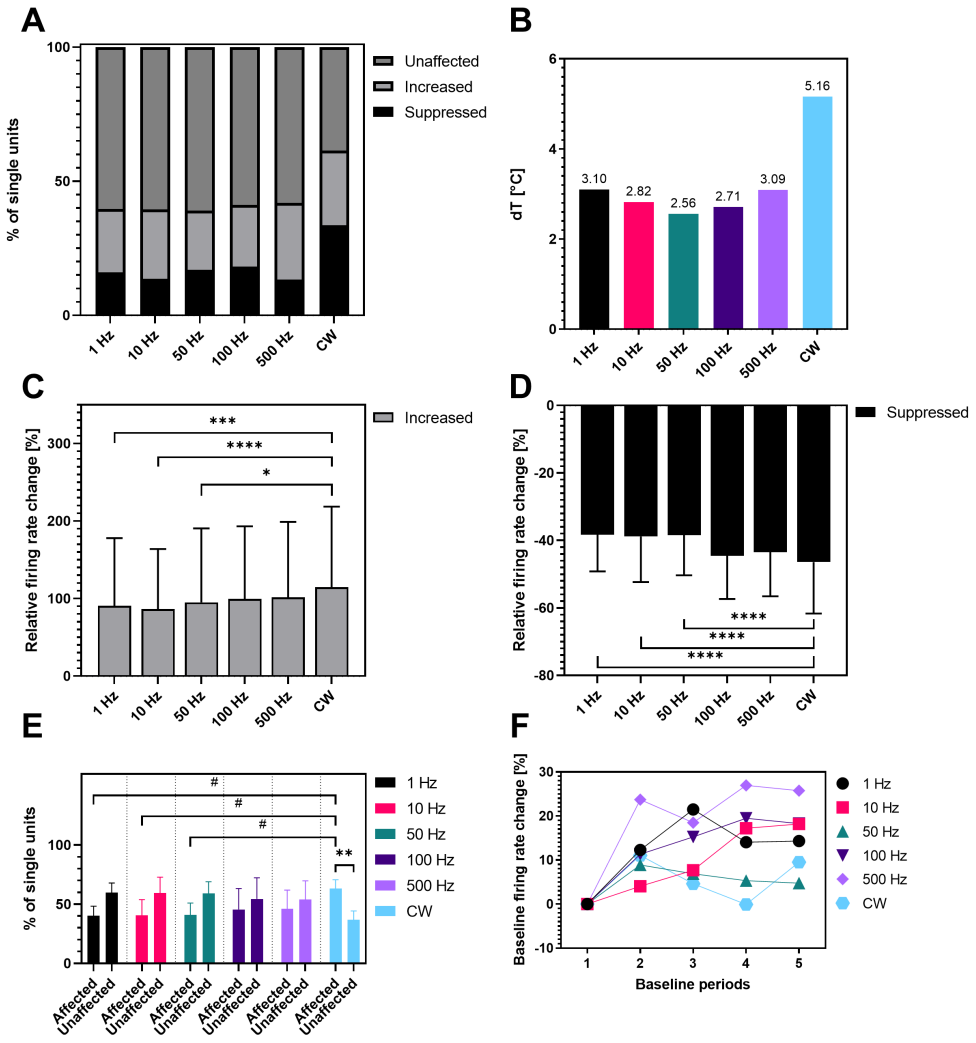

Figure 4.2: Effects of infrared stimulation on firing rates. A) The percentage of single units with suppressed and increased activity and unaffected cells at each infrared stimulation frequency. B) The maximum temperature during IR stimulation relative to the baseline temperature for each stimulation frequency. The average relative change of the firing rate in cells with C) increased and D) suppressed activity. There is a significant difference between CW stimulation and 1 Hz, 10 Hz, and 50 Hz stimulation for both single units with increased and suppressed activity (Kruskal-Wallis test: $p < 0.0001$). E) Percentage of single units affected and unaffected by stimulation. There is a significant difference between the percentage of affected cells and unaffected cells in the case of CW stimulation and between the percentage of single units affected by CW stimulation and 1, 10, and 50 Hz IR stimulation (one-way ANOVA: $p < 0.0001$). F) Average baseline firing rate calculated during OFF periods immediately preceding the stimulation periods compared to the first baseline period (two minutes before the first stimulation trial) for each stimulation frequency. Error bars represent standard deviation. (one-way ANOVA: $*p < 0.05, **p < 0.01, ***p < 0.001, ****p < 0.0001, \#p < 0.05$)[J1]

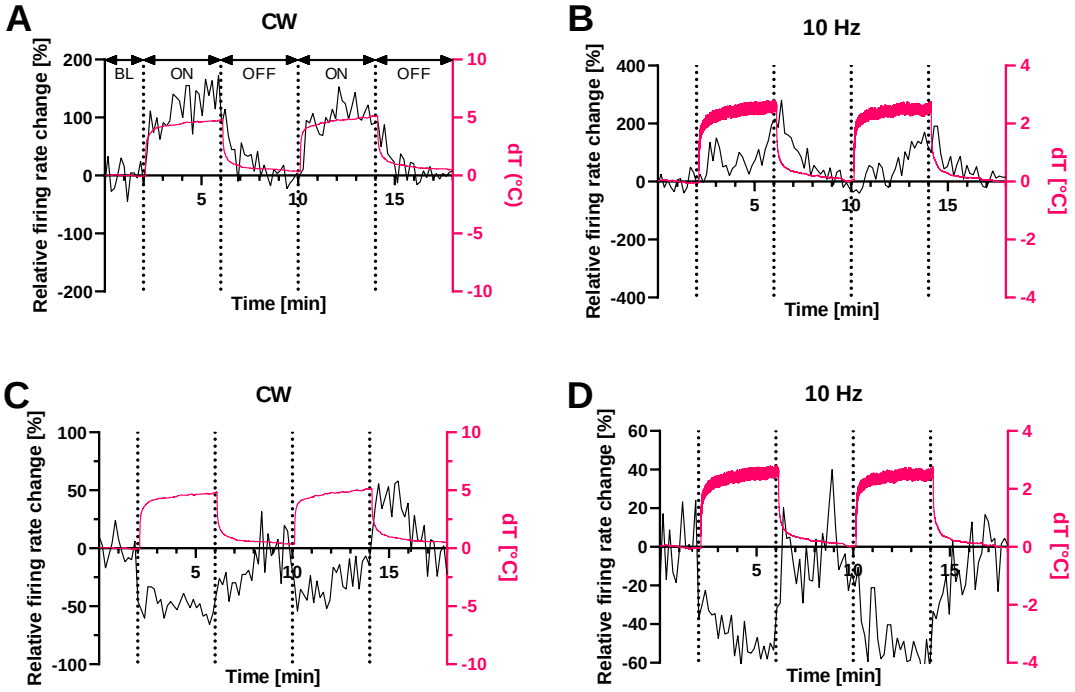

Figure 4.3: Changes in the temperature of the cortical tissue and the relative firing rate change during infrared stimulation. Single unit firing rate changes with increased activity at A) CW and B) 10 Hz stimulation, compared to the temperature change. Single unit firing rate changes with suppressed activity at C) CW and D) 10 Hz stimulation, compared to the temperature change [J1].

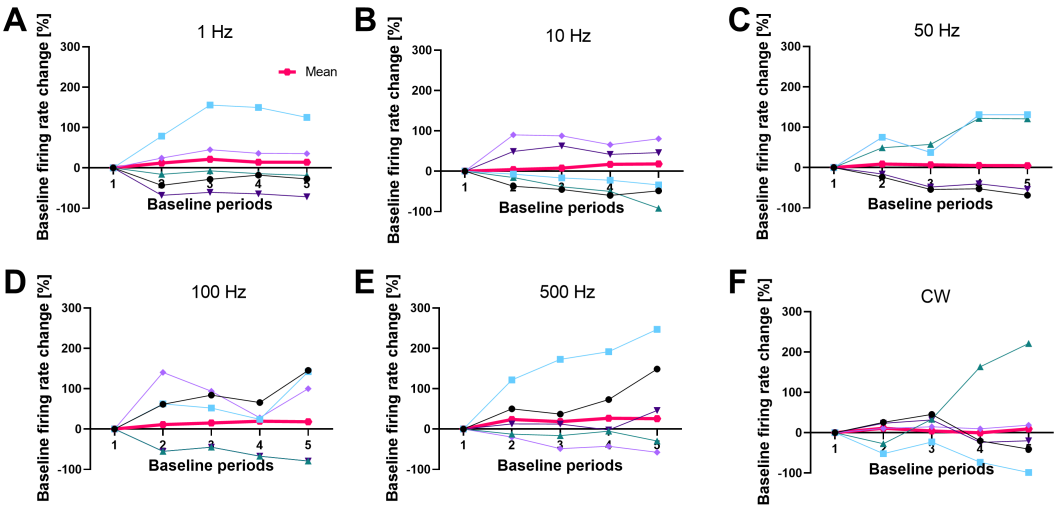

Figure 4.4: Change in baseline firing rates after consecutive infrared stimulation trials from one of the animals. The figure exhibits five different neuron examples, with the average of all baselines from this animal highlighted with a pink bold line. A) 1 Hz stimulation B) 10 Hz stimulation C) 50 Hz stimulation D) 100 Hz stimulation E) 500 Hz stimulation F) continuous (CW) stimulation [J1].

	PW			CW		
	Unaffected [%]	Increased [%]	Suppressed [%]	Unaffected [%]	Increased [%]	Suppressed [%]
Layer 2/3/4	63.54 ± 3.09	18.24 ± 4.92	18.22 ± 4.77	36.95	15.22	47.83
Layer 5	61.92 ± 1.41	21.29 ± 2.34	12.57 ± 2.89	36.89	27.27	35.82
Layer 6	63.71±3.7	23.73 ± 5.28	12.57 ± 2.89	42.94	33.33	23.72

Table 4.2: The mean ratio of unaffected single units during pulsed wave (1 Hz, 10 Hz, 50 Hz, 100 Hz, 500 Hz) and continuous wave stimulation, along with their standard deviation.

4.1.2 Cortical layer-type dependent effects of infrared stimulation

Isolated single units were assigned to cortical layers based on electrophysiological markers of the recorded cortical slow wave activity and on anatomical features of Nissl-stained coronal brain sections containing the probe track. Cortical layer 1 was excluded based on the absence of cells, and layers 2, 3, and 4 were combined (hereafter referred to as superficial and input layers) (Table 4.3).

During pulsed wave stimulation, the activity of most single units remained unchanged in the superficial and input layers (Figure 4.5A), as well as in layer 5 (Figure 4.5B) and layer 6 (Figure 4.5C) (Table 4.2). However, continuous-wave stimulation markedly increased the number of affected cells, resulting in the highest percentage of suppressed activity within each layer (Table 4.2). The response to CW stimulation, which increased the number of affected cells in all three layers, was consistent across each layer group, even though fewer cells were recorded in the superficial and input layers compared to layers 5 and 6 (Table 4.3). Interestingly, despite the differences in cell count in the cortical layers, the proportion of cells with suppressed activity was significantly higher in the superficial and input layers, and even in layer 5 compared to layer 6 (47.83% vs. 35.83% vs. 23.72%).

The change in firing rate did not exhibit a clear increase in stimulation frequency in the superficial and input layers (Figure 4.5D), however, it was observed to be highest during continuous wave stimulation. A similar observation was noted in layer 5 (Figure 4.5E), while layer 6 (Figure 4.5F) showed no evident increase in firing rate. Conversely, for suppressed single units, the firing rate change decreased in the superficial and input layers (Figure 4.5G), layer 5 (Figure 4.5H), and layer 6 (Figure 4.5I). A significant difference in the relative firing rate change was observed between CW stimulation and 10 Hz stimulation in superficial and input layers (Figure 4.5D) (Kruskal-Wallis test: $p = 0.0106$). Meanwhile, the relative firing rate change in layer 5 was significantly higher with CW than at 1 Hz and 10 Hz stimulation, as shown in Figure 4.5E (Kruskal-Wallis test: $p < 0.0001$). In contrast, for suppressed activity, the firing rate change in superficial and input layers was significantly lower for CW stimulation compared to 1 Hz and 10 Hz stimulation, as depicted in Figure 4.5G (Kruskal-Wallis test: $p = 0.0004$). Additionally,

	Layers 2/3/4	Layer 5	Layer 6
1 Hz	147	515	442
10 Hz	161	463	454
50 Hz	143	533	406
100 Hz	108	391	290
500 Hz	105	479	517
CW	92	374	333
Total	756	2755	2442

Table 4.3: Number of isolated single units in each layer group.

in layer 5, it was also significantly lower for CW stimulation compared to 1 Hz, 10 Hz, and 50 Hz stimulation (Kruskal-Wallis test: $p < 0.0001$). In layer 6, there was also a significant decrease in the relative firing rate in cells with suppressed activity for CW stimulation compared to 1 Hz and 50 Hz stimulation (Kruskal-Wallis test: $p = 0.0003$), although no such significant difference was observed in cells with increased activity.

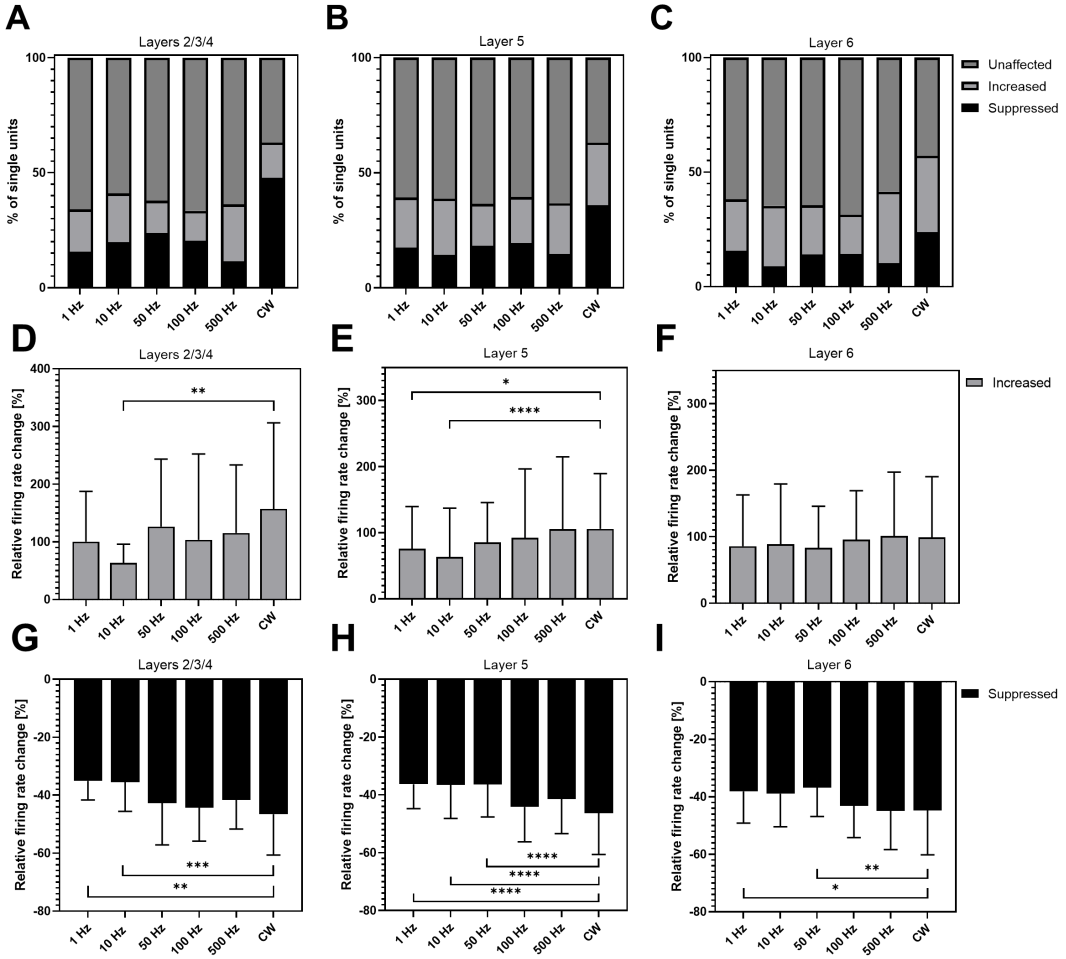

Figure 4.5: Percentage of single units with suppressed, increased, and unaffected activity in A) superficial and input cortical layers, B) layer 5, C) and layer 6. The relative firing rate change of single units with D-F) increased and G-I) suppressed activity in layers 2/3/4 (D, G), layer 5 (E, H), and layer 6 (F, I) Error bars represent standard deviation. (Kruskal-Wallis test: $*p < 0.05, **p < 0.01, ***p < 0.001, ****p < 0.0001$)[J1]

In conclusion, the results demonstrated that continuous wave stimulation led to a notable increase in suppressed activity across all cortical layers. In the case of pulsed wave stimulation, most of the single units in the superficial layers, input layer, as well as layers 5 and 6, demonstrated minimal change. In contrast, CW stimulation markedly increased the number of affected cells, resulting in the highest percentage of suppressed activity within each layer. It is also observed that the depth of the layer in question affects the number of suppressed units, with a decrease in the number of suppressed units and an increase in the number of units with increased activity as depth increases. Figure 4.6 provides further insight into this distribution, demonstrating that most suppressed units are concentrated in the superficial and input layers and layer 5, while layer 6 shows more units with increased activity, with unaffected cells remaining the majority across all layers.

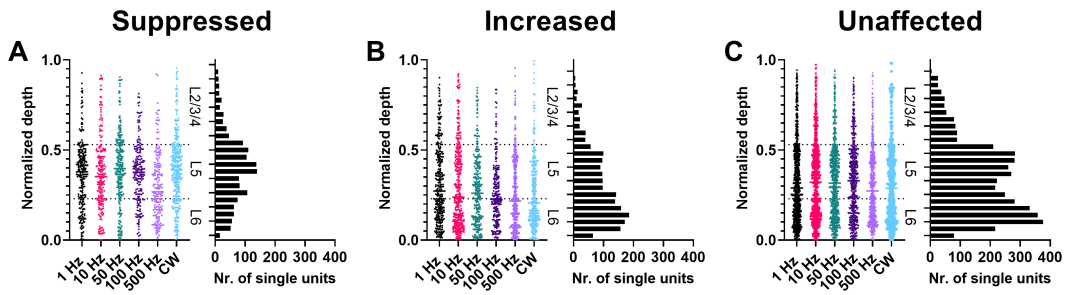

Figure 4.6: Responses of single units with suppressed (A), increased (B) and unaffected (C) responses to infrared neural stimulation at different frequencies, plotted by cortical depth. Each point represents a single unit. The y-axis indicates the normalized depth of the neurons, with dashed lines marking the boundaries between layers. Alongside each subplot is a distribution plot along the y-axis, depicting the spread of neurons' depths for each response category [J1].

4.1.3 Neuron-type dependent effects of infrared stimulation

To examine neuron type-specific effects of IR stimulation, putative interneurons, and principal cells were distinguished based on the distribution of trough-to-peak times of the mean spike waveforms. The waveforms of principal cells are wider than the waveforms of interneurons, as also shown in Figure 4.7A [37]. The average percentage of interneurons was found $24.08\% \pm 5.80\%$, and the average percentage of principal cells is $75.92\% \pm 5.80\%$ (Figure 4.7B). The higher percentage of principal cells is consistent with findings in the literature (ratio and number of principal cells and interneurons used in the recordings and analysis: Table 4.4 and Table 4.5) [140].

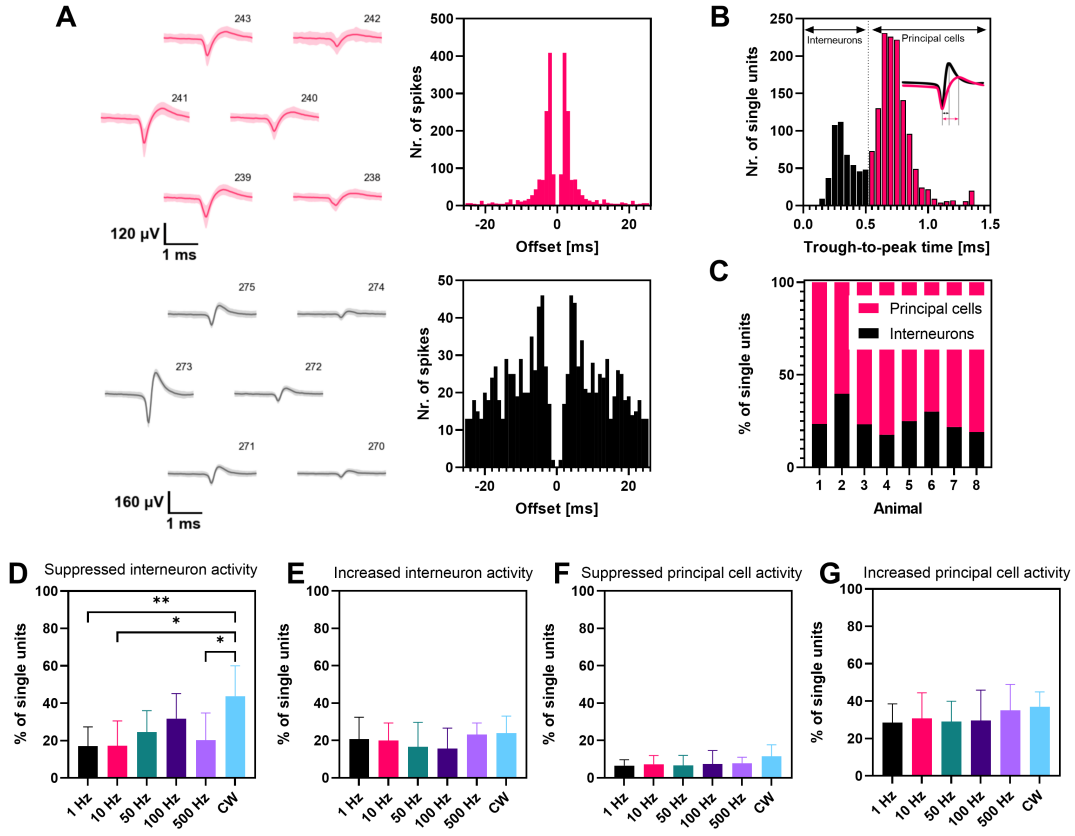

Figure 4.7: Effects of infrares stimulation on interneurons and principal cells. A) Example mean waveforms with standard deviations of a spike cluster from a principal cell (pink) and one from an interneuron (black). The channel numbers are indicated next to the waveforms. The auto-correlograms of the same spike clusters with the largest amplitude are presented in the same color. B) Bimodal distribution of the trough-to-peak times calculated from the mean spike waveforms of single units from the representative animal. The threshold used to separate putative interneurons and principal cells is marked with the dotted line (0.52 ms). Cells with narrow spike waveforms are putative interneurons (black), and single units with wide spikes are principal cells (pink). C) Proportion of interneurons and principal cells in each animal (see also Table 4.4). D) Percentage of suppressed interneurons. There is a statistically significant difference in the number of interneurons that are suppressed between the stimulation of 1 Hz, 10 Hz, 500 Hz, and CW stimulation (Kruskal-Wallis test: p = 0.0076). E) Percentage of interneurons with increased activity. F) Percentage of suppressed principal cells. G) Percentage of principal cells with increased activity. Error bars represent standard deviation. (Kruskal-Wallis test: $*p < 0.05, **p < 0.01$)[J1]

Next, for each stimulation type, I determined the proportion of putative interneurons and principal cells exhibiting suppressed or increased activity. I have found that the activity of more interneurons was suppressed (23.17% ± 13.2%) than increased (20% ± 10.11%), whereas more principal cells showed increased activity (27.85%±9.91%) compared to suppressed activity (12.98% ± 9.45%) (Figure 4.7D-G). The percentage of interneurons and principal cells, whether suppressed (Figure 4.7D and F) or exhibiting increased

	interneurons in recordings [%]	interneurons in analysis [%]	principal cells in recordings [%]	principal cells in analysis [%]
Animal 1	22.07	23.40	77.93	76.60
Animal 2	34.29	39.70	65.71	60.30
Animal 3	21.90	23.19	78.10	76.81
Animal 4	17.36	17.61	82.64	82.39
Animal 5	19.90	25.06	80.10	74.94
Animal 6	31.31	30.17	68.69	69.83
Animal 7	21.33	21.80	78.67	78.20
Animal 8	24.51	19.07	75.49	80.93

Table 4.4: Ratio of interneurons and principal cells in each animal during recordings and analysis

	Nr. of interneurons in recordings	Nr. of interneurons in analysis	Nr. of principal cells in recordings	Nr. of principal cells in analysis
Animal 1	333	196	1176	693
Animal 2	442	304	442	585
Animal 3	383	232	1366	830
Animal 4	319	215	1519	1027
Animal 5	419	247	1687	997
Animal 6	520	266	1141	586
Animal 7	429	167	1582	619
Animal 8	425	159	1309	493

Table 4.5: Number of interneurons and principal cells in each animal during recordings and analysis

activity (Figure 4.7E and G), appeared to increase with stimulation frequency. However, a statistically significant difference was found only for suppressed interneurons between 500 Hz, 10 Hz, and 1 Hz stimulation compared to CW stimulation (Kruskal-Wallis test: $p = 0.0076$). In addition, the firing rates of both interneurons (Figure 4.8A) and principal cells (Figure 4.8C) that exhibited enhanced activity increased with stimulation frequency. In contrast, the firing rates of suppressed interneurons (Figure 4.8B) and principal cells (Figure 4.8D) decreased with stimulation frequency. This was consistent with what was previously shown in Figure 4.2C and D. The average relative firing rate change of interneurons with suppressed (Figure 4.9A), increased (Figure 4.9B) and unchanged (Figure 4.9D) activity, as well as the average relative firing rate change of principal cells with suppressed (Figure 4.9D), increased (Figure 4.9E) and unchanged (Figure 4.9F) activity was also examined. Notably, there was no discernible difference in the firing rate change between the two cell types.

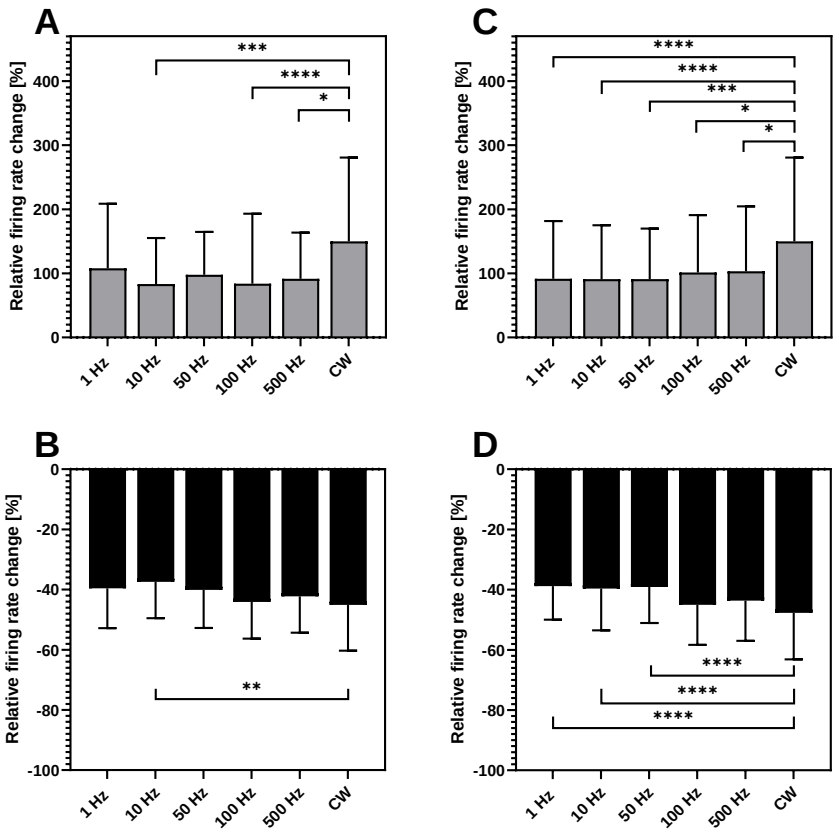

Figure 4.8: Changes in relative firing rates of interneurons and principal cells at different stimulation frequencies. A) Interneurons with increased activity showed significantly higher firing rates during continuous wave (CW) stimulation compared to 10 Hz, 100 Hz, and 500 Hz stimulation frequencies. B) Interneurons with suppressed activity showed significantly lower firing rates during CW stimulation than during 10 Hz stimulation. C) Principal cells with increased activity showed significantly increased firing rates during CW stimulation compared to pulsed wave stimulation. D) Principal cells with suppressed activity showed significantly reduced firing rates during continuous stimulation compared to 1 Hz, 10 Hz, and 50 Hz stimulation. Error bars represent standard deviation. (Kruskal-Wallis test: $*p < 0.05, **p < 0.01, ***p < 0.001, ****p < 0.0001$)[J1]

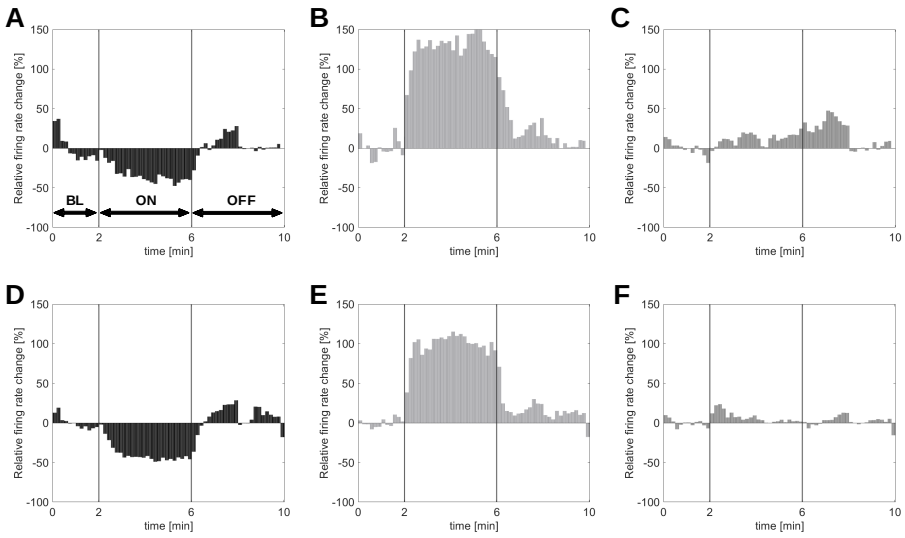

Figure 4.9: Relative firing rate change of all interneurons, averaged over every animal and trial, with A) suppressed, B) increased and C) unaffected activity. Relative firing rate change of all principal cells, averaged over every animal and trials, with D) suppressed, E) increased, and F) unaffected activity at CW stimulation [J1].

In conclusion, the examination of the types of neurons revealed that interneurons exhibited a greater degree of suppressed activity than increased activity, especially at 50 Hz, 100 Hz, and CW stimulation, while principal cells exhibited the opposite pattern, with a greater number of cells showing increased activity than suppressed activity. The firing rate changes also exhibited distinct patterns. For principal cells, higher stimulation frequencies appeared to amplify the existing response pattern: those with increased activity tended to show progressively higher firing rates, while those with suppressed activity showed progressively greater reductions in firing. In the case of interneurons, there was no significant increase or decrease. Nevertheless, the modulatory effect appeared to be most pronounced during continuous wave stimulation, associated with the highest relative firing rates in interneurons showing enhanced activity and the lowest in those showing suppression.

Data from different stimulation frequencies were recorded and analyzed separately. However, to illustrate the response of individual neurons over the entire stimulation protocol, recordings from a single animal were concatenated and then spike sorting was performed on the concatenated recording. Figure 4.10 illustrates the relative changes in firing rates of different types of neurons, and their trial-averaged responses, consisting of a principal cell with suppressed activity (Figure 4.10A), one with increased activity (Figure 4.10B), and one with unaffected activity (Figure 4.10C), an interneuron with suppressed activity (Figure 4.10D), one with increased activity (Figure 4.10E), and another with unaffected activity (Figure 4.10F) during CW stimulation. It is important to note that although these individual units may exhibit suppressed or increased activity in response

to CW stimulation, their responses to various stimulation frequencies can vary. This demonstrates that a single unit can display either suppressed or increased activity (see Figure 4.10A at 100 Hz and CW stimulation).

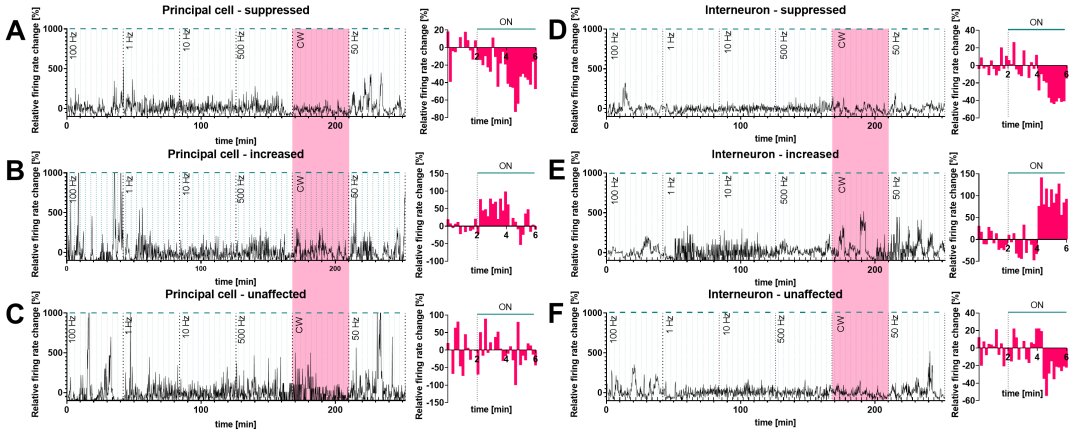

Figure 4.10: Examples of individual single-unit responses determined during CW stimulation for the different IR stimulation frequencies and their trial-averaged responses, marked in pink. A) Putative principal cell with suppressed activity at CW stimulation, B) principal cell with increased activity at CW stimulation C) principal cell with unchanged activity D) interneuron with suppressed activity at CW stimulation E) interneuron with increased activity at CW stimulation F) interneuron with unchanged activity at CW stimulation. The sequence of stimulation frequencies at this animal was the following: 100 Hz, 1 Hz, 10 Hz, 500 Hz, CW, and 50 Hz. The 4-minute-long ON periods are noted with green horizontal bars [J1].

4.1.4 Single unit response times to infrared stimulation

Analyzing the changes in neuronal activity during suppression and excitation, and investigating how these dynamics correlate with the corresponding thermal effects, may provide new insights into infrared neural stimulation and facilitate the design of optimized stimulation protocols. Figure 4.11 shows these response times across stimulation frequencies and stimulation trials. The time required to reach 90% of the maximum cortical temperature during the ON period (rise time) for each stimulation frequency shows a consistent increase with higher stimulation frequencies (Figure 4.11A). The rise times of the relative firing rate for suppressed single units during the first ON period (Figure 4.11A) were significantly longer with CW stimulation compared to pulsed infrared light (Kruskal-Wallis test: $p = 0.0007$). The data also showed that single units with increased activity had a significantly longer rise time with CW stimulation compared to 50 Hz stimulation (Kruskal-Wallis test: $p = 0.0002$). The time course of the firing rate change and the temperature change at CW and 10 Hz stimulation are also shown in Figure 4.3.

It is also important to analyze the temporal differences during the five trials to determine if the firing rate changes and their relationship to infrared stimulation-induced temperature changes remain consistent over multiple stimulation trials or if there are fluctuations that

could provide further insight into the dynamics of infrared neural stimulation. Notably, there is no significant difference in the rise time of the suppressed single units (Figure 4.11B) and the single units with increased activity (Figure 4.11C), indicating that the average rise time (35.95 s $\pm$ 27.6 s) remained consistent throughout the repetition of each stimulation cycle.

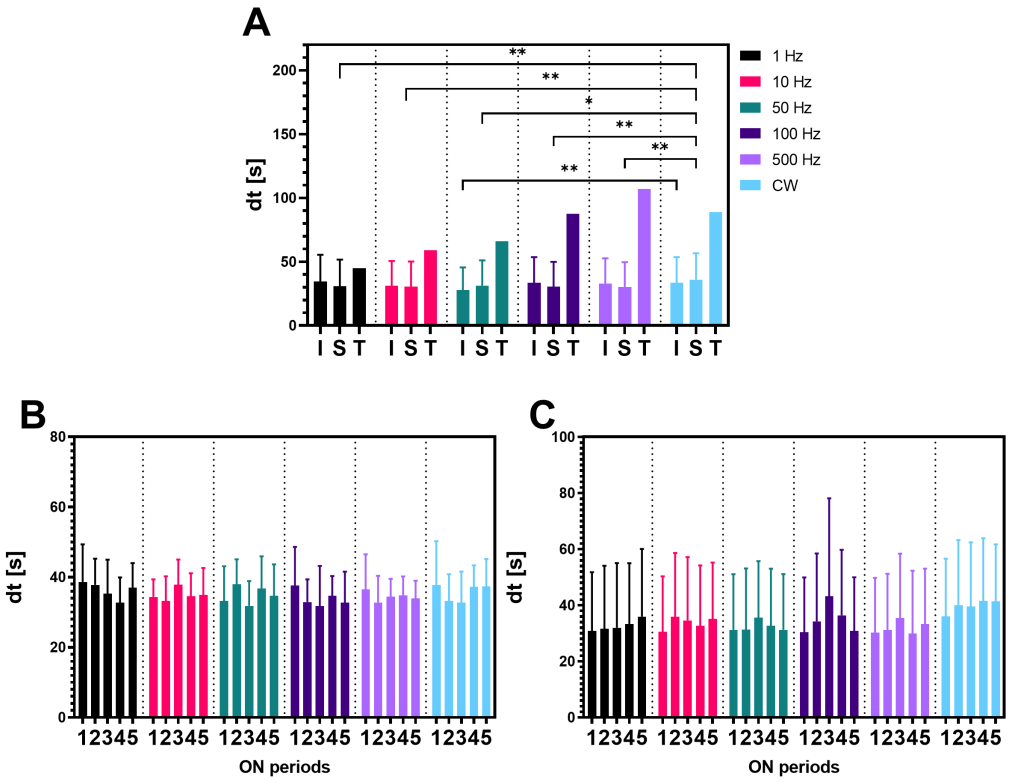

Figure 4.11: Single unit rise times. A) (I) The rise time of single units with increased activity during the first stimulation trial, at every stimulation frequency. The rise time was significantly longer when single units were stimulated with continuous light than with 50 Hz stimulation. (Kruskal-Wallis test: p = 0.0007) (S) The rise time for the single units with suppressed activity during the first stimulation trial. The duration was significantly longer when single units were stimulated with continuous light than with pulsed infrared light.(Kruskal-Wallis test: p = 0.0002) (T) The time needed for the cortical temperature to reach the 90% of the maximum at each IR stimulating frequency from the onset of the stimulus, calculated from one measurement. B) Change in the rise times during the five stimulation trials when the single units' activity was increased. C) Temporal differences in the five trials when the single units' activity was suppressed. Error bars represent standard deviation. (Kruskal-Wallis test: $*p < 0.05, **p < 0.01$)[J1]

I also examined the rate of change of temperature and firing rate after the stimulation trials. Figure 4.12A shows the time taken to reach 10% of the maximum temperature after the light was turned off (fall time). Interestingly, the fall time of the temperature did not show significant variation across different stimulation frequencies, and in particular, it was considerably faster than the rise times of the temperature (as shown in Figure

4.11A).

The time taken to reach 10% of the mean change in firing rate during the first OFF period was also examined. It can be noted that the fall time was shorter during CW stimulation compared to PW stimulation in both single units with increased and suppressed activity. In the case of single units with increased activity, the results indicated that the fall time was significantly shorter during CW stimulation compared to 10 and 50 Hz stimulation (Kruskal-Wallis test: $p = 0.0094$). However, for suppressed single units, there was no significant difference in fall times, although CW stimulation still resulted in the shortest fall time.

The changes in fall time over the five OFF periods were also examined (Figure 4.12B-C). The results suggest that the average fall time (20.91 s $\pm$ 18.78 s) remained constant throughout five repeated trials for both suppressed (Figure 4.12B) and increased (Figure 4.12C) activity, as no significant difference was observed between them.

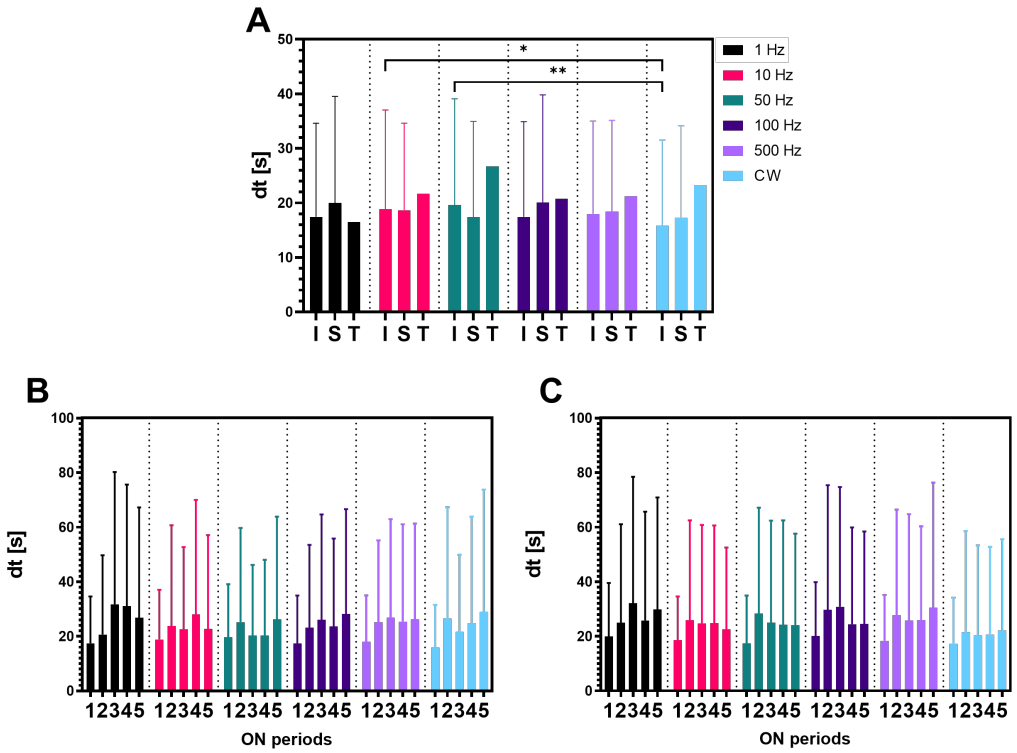

Figure 4.12: Single unit fall times. A) (I) The fall time of increased activity after the first stimulation trial. The fall time was significantly shorter when single units were stimulated with continuous light than with 10 Hz and 50 Hz stimulation (Kruskal-Wallis test: p = 0.0094). (S) The fall time of the suppressed activity after the first stimulation trial. C) (T) The time needed to reach the 10% of the maximum cortical temperature during OFF periods, calculated from a single measurement. B) Temporal differences in the five trials when the single units' activity was suppressed. C) Temporal differences in the five trials when the single units' activity was increased. Error bars represent standard deviation. (Kruskal-Wallis test: $*p < 0.05, **p < 0.01$)[J1]

I also examined the rise and fall times for the two different cell types (Figure 4.13).

The rise and fall times exhibited a high degree of similarity, with no notable differences observed. Therefore, it suggests that these effects are not cell specific, but rather stimulation frequency specific.

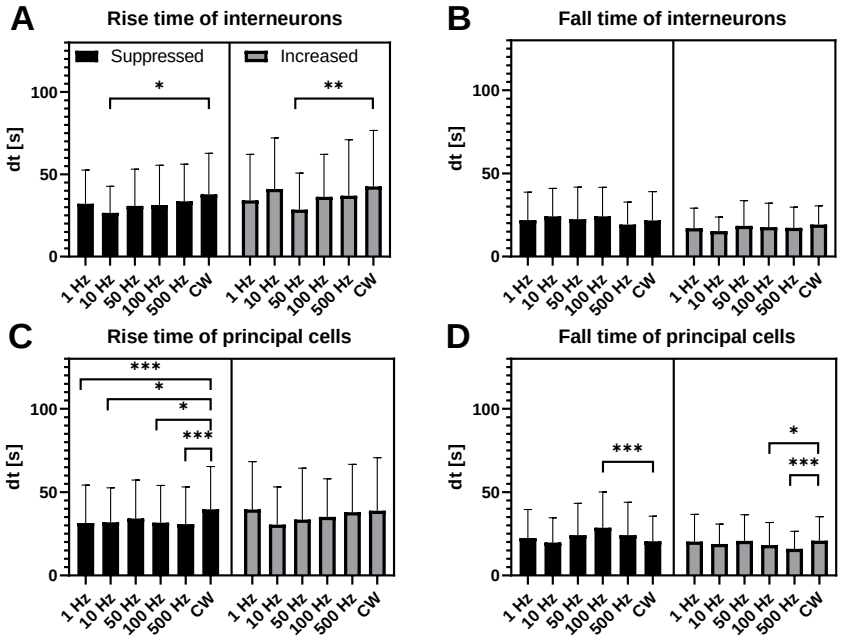

Figure 4.13: Rise times and fall times for different cell types. A) Rise times of interneurons with suppressed and increased activity. B) Fall times of interneurons with suppressed and increased activity. C) Rise time of principal cells with suppressed and increased activity. D) Fall times of principal cells with suppressed and increased activity. Error bars represent standard deviation. (Kruskal-Wallis test: $*p < 0.05, **p < 0.01, ***p < 0.001$)[J1]

4.2 Results related to the SMP microECoG experiments

4.2.1 *In vitro* measurements

To assess the effect of the microECoG device on two-photon imaging, we acquired images of 68 fluorescent microbeads placed on glass slides both with and without the SMP microECoG positioned over the beads. As part of this analysis, I developed custom image processing scripts that could automatically detect individual beads and quantify their diameters. My main contribution at this stage was designing and implementing the data analysis pipeline to evaluate the optical distortion introduced by the device. Figure 4.14A shows box plots of bead diameters, with values normalized to the mean diameter observed in the absence of the SMP microECoG ($5.6651 \pm 0.0066\ \mu m$). This normalization was performed because the mean measurement was significantly different (t-test, p « 0.001) from the 6 μm standard; however, variability in bead size and differences in two-photon microscope settings can also affect the measurements. A Student's paired t-test was performed at a significance level of 0.05 and the results showed no significant difference in bead diameters between the two conditions ($t(67) = 1.08$, $p = 0.29$, mean difference:

0.0142 μm). These results support my hypothesis that the SMP-based microECoG device does not introduce significant optical distortion. Overall, the bead size measurements remained consistent with and without the SMP microECoG and closely matched the nominal bead size, indicating that the resolution limit of the imaging system, rather than the presence of the SMP microECoG, is the primary factor affecting accuracy.

The quality of two-photon calcium imaging and the potential for optical distortion were further evaluated using acute brain slices *in vitro*. To assess the device's impact on the ability to resolve fine neuronal structures, I performed measurements of dendrite diameters in images acquired both with and without the microECoG device in place. This analysis allowed for a direct comparison of imaging resolution under the two conditions, and was a key part of my contribution to the optical characterization of the device. dendrites were identified in images of hippocampal regions, with the imaging plane aligned parallel to the dendrites to maximize the number of samples detected. Figure 4.14B shows the diameters of detected dendrites from the same field of view (FOV) at different depths from the slice surface.

The detection algorithm identified 81 dendrites in the images without the SMP microECoG and 112 dendrites with the SMP microECoG. Statistical analysis revealed no significant difference in dendrite diameter between the two conditions within the same FOV at a significance level of $\alpha = 0.05$. The results of the Student's two-sample t-test at different depths are shown in Table 4.6.

Depth	n_{without}	n_{with}	t	p
$z = 50\ \mu m$	21	28	t(47)=-0.18	0.85
$z = 60\ \mu m$	17	28	t(43)=-0.61	0.55
$z = 70\ \mu m$	16	33	t(47)=-0.18	0.85
$z = 80\ \mu m$	27	23	t(48)=-0.25	0.81

Table 4.6: Results of the Student's two-sample t-test on dendrite diameters at different depths.

These *in vitro* results demonstrate that even fine dendrites in the hippocampus can be successfully visualized in the presence of the microECoG device without introducing optical distortions in the two-photon images.

4.2.2 *In vivo* measurements

Three awake, freely moving mice implanted with the microECoG device were imaged using a two-photon microscope with the GCaMP6f calcium indicator. Imaging sessions were performed at multiple time points post-implantation, spanning up to 22 weeks. Labeled neurons were visible in the first images (1-2 weeks post-implantation) and their clear contrast to the background was maintained throughout the experiment.

In order to quantify imaging stability over time, I developed and applied an analytical method that measured the fluorescence intensity of neurons that were automatically detected, normalised to background fluorescence, on each measurement day. For SMP mi-

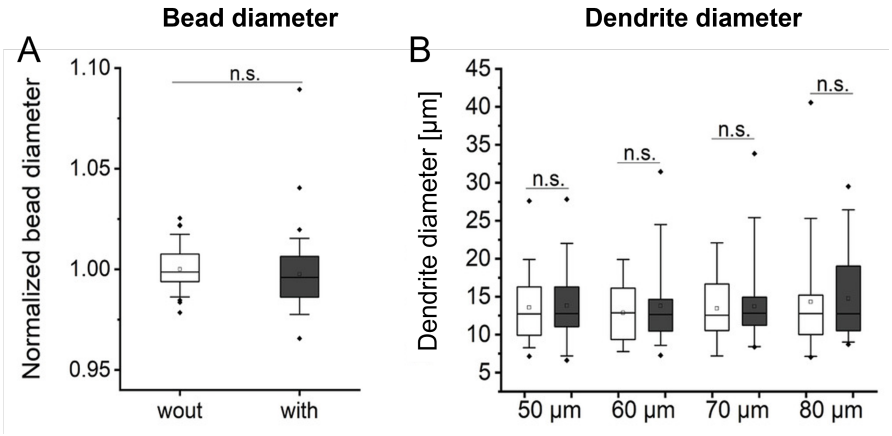

Figure 4.14: Diameter of the beads and dendrites. A) Normalized diameter of the same beads without (n = 68) and with (n = 68) the microECoG device covering them. No significant difference was observed between groups (Student's two-sample t-test: p = 0.29) B) Diameter of dendrites measured on *in vitro* slices from the same FOV but at different depths. The empty box plots represent measurements taken without the SMP microECoG covering the slice, while the filled box plots show measurements with the SMP microECoG in place. The boxplot whiskers indicate the 5th and 95th percentiles, and outliers are marked by the symbol ⋄. No significant difference was observed between groups (Student's two-sample t-test: $p_{50} = 0.85$, $p_{60} = 0.55$, $p_{70} = 0.85$, $p_{80} = 0.81$) [J3].

croECoG A, relative intensity changes remained stable across sessions, with no significant differences between measurement days (Student's t-test: $t(65) = -0.79$, $p = 0.43$) (Figure 4.15a). In contrast, SMP microECoG B showed a significant variation in relative intensity across measurement days (one-way repeated analysis of variance ANOVA, OriginPro: $F(1.72, 96.15) = 16.99$, $p \ll 0.05$). However, the mean relative intensity remained above 0.5 throughout the measurement period (Figure 4.15b).

As both SMP microECoGs used the same substrate material (thiol-ene/acrylate) in the optical path, I hypothesize that the observed differences in imaging performance are likely due to factors such as variations in GCaMP6f expression rather than the microECoG device itself. Chronic imaging quality may be influenced by immune response, sensor expression efficiency, tissue regrowth, or other biological factors.

4.2.3 Results of the spike detection

Over a period of seven weeks, data collected from a single animal demonstrated consistent neural spiking activity, including both multi-unit and single-unit events. My role involved detecting spikes directly from the raw data and then analysing the detected activity in depth. To differentiate between the various cell types, putative pyramidal cells, narrow-waveform interneurons, and wide-waveform interneurons were classified based on the trough-to-peak time of the waveform and the burstiness index. The clustering exhibited an average of $24.01 \pm 7.8\%$ of cells classified as narrow-waveform interneurons, $52.15 \pm 14.63\%$ as wide-waveform interneurons, and $23.84 \pm 14.24\%$ as pyramidal cells. The distribution

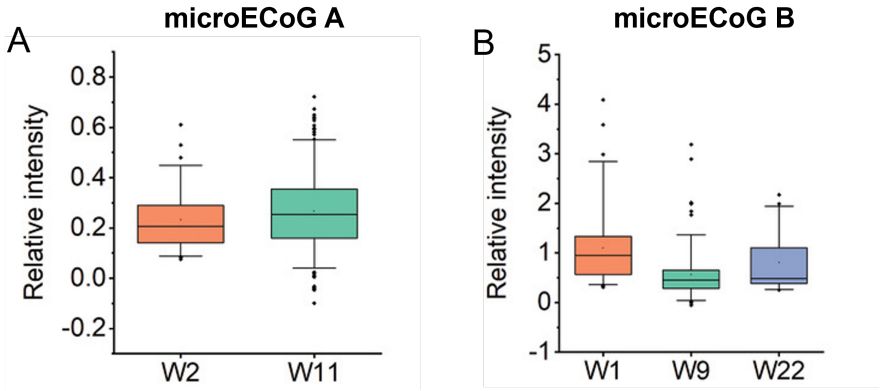

Figure 4.15: Relative intensity change measurements with microECoG A and B from two representative animals. A) Measurements with SMP microECoG A (without SIROF layer). Long-term two-photon relative intensity change compared to background intensity ($n_{W2} = 66; n_{W11} = 254$). The different box plots represent measurements taken on different days. No significant difference was observed between groups (Student's two-sample t-test: p = 0.43). B) Measurements with SMP microECoG B (with SIROF layer) ($n_{W1} = 67; n_{W22} = 57$). Box plots represent different measurement days. Boxplot whiskers are $5th$ and $95th$ percentiles, and ♦ are the outliers. No significant difference was observed between groups (one-way ANOVA: $p \ll 0.05$) [J3].

and the number of detected cell types over the seven weeks is outlined in Tables 4.7 and 4.8. The values presented in the table for interneurons and pyramidal cells do not align with the standard proportions documented in the existing literature. This is because data were collected from a limited number of clusters, and the data underwent filtering, which resulted in a restriction of the types of cells detected. Therefore, it is important to note that these numbers represent specific data and not the general cellular composition of the cortex. The mean burstiness index for the different neuron types was 1.267 ± 0.208 for narrow-waveform interneurons, 1.033 ± 0.142 for wide-waveform interneurons, and 1.426 ± 0.273 for pyramidal cells. These values indicate that pyramidal cells tend to have a higher burstiness index compared to interneurons, reflecting their well-known burst firing patterns.

Weeks	% of N-S Interneurons	% of W-S Interneurons	% of Pyramidal Cells
1	25	43,75	31,25
2	36,36	9,09	54,55
3	20	10	70
4	16,67	41,66	41,67
5	30,77	23,08	46,15
6	14,29	14,298	71,43
7	25	25	50

Table 4.7: Percentages of the different cell types over the seven weeks. (N-S: narrow-spiking; W-S: wide-spiking)

As illustrated in Figure 4.16, the waveforms of 82 spikes, along with their mean, have

Weeks	Nr. of N-S Interneurons	Nr. of W-S Interneurons	Nr. of Pyramidal Cells
1	4	7	5
2	4	1	6
3	2	1	7
4	2	5	5
5	4	3	6
6	1	1	5
7	2	2	4

Table 4.8: Number of the different cell types over the seven weeks. (N-S: narrow-spiking; W-S: wide-spiking)

been extracted from a putative pyramidal cell exhibiting single-unit activity. Figure 4.16B shows the corresponding auto-correlogram, while Figure 4.16C presents the firing rate and spontaneous activity of the single-unit activity cluster. Spike clusters recorded over seven weeks were analyzed using all available channels. The number of detected clusters varied depending on recording quality and cell firing rates. The SNR ratio was assessed throughout the recordings (Figure 4.16D). A clear trend of decreasing SNR was observed throughout the weeks. The statistical test results indicate that the majority of changes occurred during the first few weeks (weeks 1–4), likely due to biological responses and the initial development of scar tissue. In week 5, a significantly lower SNR was observed in comparison to the initial three weeks, and this diminished SNR persisted through weeks 6 and 7 (Kruskal-Wallis test: $p < 0.0001$). Figures 4.16E and 4.16F illustrate the mean amplitude and thespike rate recorded over time, respectively (Kruskal-Wallis test: $p < 0.0001$). Amplitudes in weeks 6 and 7 were significantly lower compared to weeks 1, 2, and 3. In contrast, the firing rate showed an overall increasing trend throughout the recordings, although a notably low value was observed in week 5. The firing rate in week 6 was significantly higher than in weeks 1 and 5 (Kruskal-Wallis test: $p < 0.0015$). Additionally, Figure 4.16G depicts the average number of spike clusters detected per week, highlighting variations across the seven weeks. A more detailed analysis focused on spike clusters recorded from two specific channels over the long term. A more detailed analysis focused on spike clusters recorded from two specific channels over an extended period. These clusters were selected from all recorded units due to their consistent presence on the same two channels across all weekly recordings. This allowed for a closer examination of neuronal activity characteristics over time. Figure 4.16H illustrates the maximum spike amplitude of these two clusters, while Figure 4.16I presents their corresponding firing rates. Notably, these clusters closely align with the average amplitude and spike count trends shown in Figures 4.16E and 4.16F. This consistency further supports the reliability of the findings, suggesting that the observed spike characteristics reflect broader trends in the dataset.

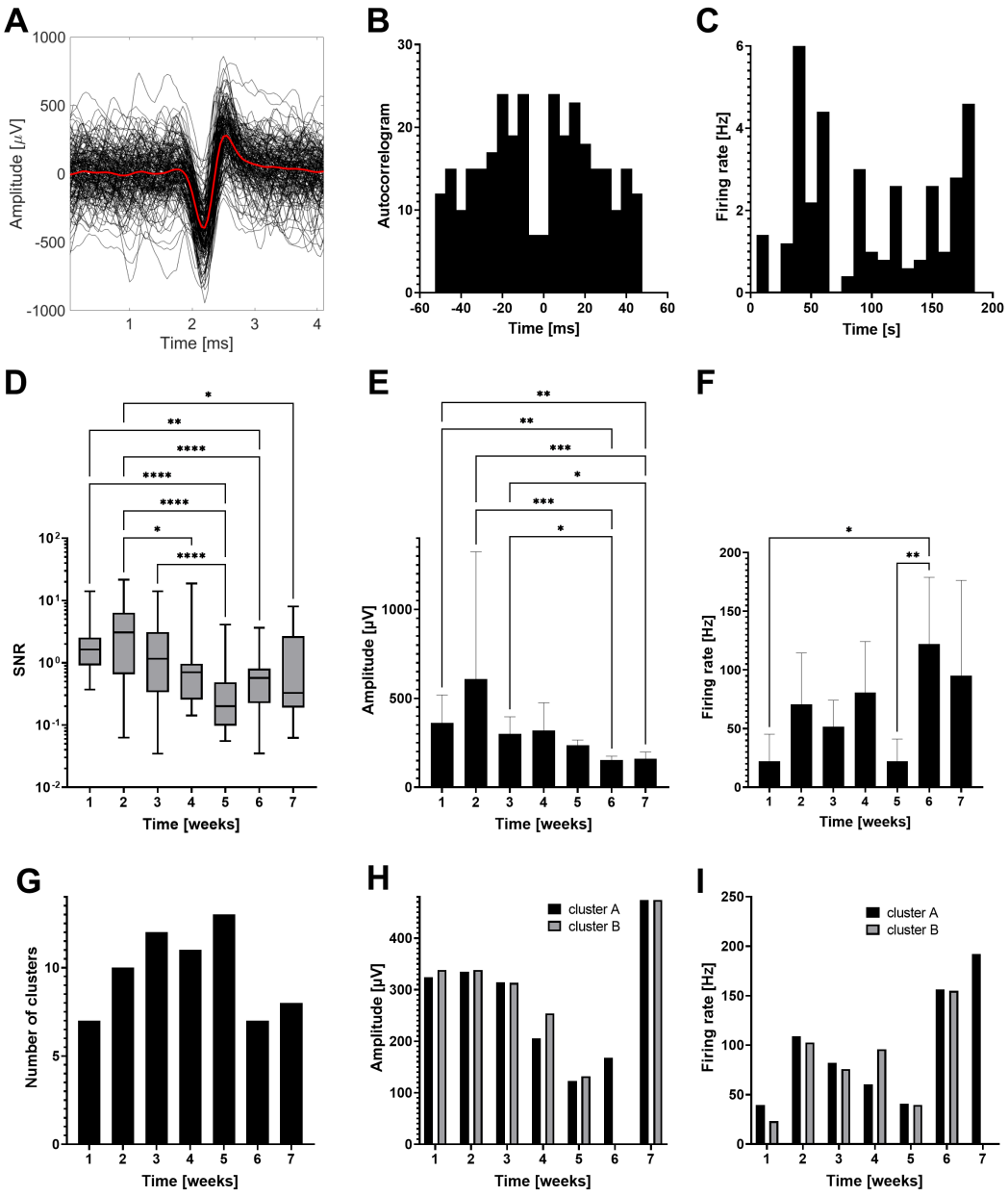

Figure 4.16: Long term single unit recordings. A) Waveforms of one single-unit cluster, their average is highlighted B) Auto correlogram of the single unit cluster. C) Firing rate of the single unit cluster D) Signal-to-noise ratio of the clusters. The box plot shows the interquartile range, which extends from the 25th to the 75th percentile, and the whiskers represent the minimum and maximum values of the data set. E) Mean amplitude of the spikes in all of the clusters during the chronic recordings. F) Firing rate in all of the clusters. G) Number of detected clusters in the chronic recordings H) Maximum amplitude of the spikes in two clusters (cluster A and B) I) Firing rate of cluster A and B. Error bars represent standard deviation. (Kruskal-Wallis test: $*p < 0.05, **p < 0.01, ***p < 0.001, ****p < 0.0001$) [J2].

5 Discussion

5.1 Cortical neuronal responses to infrared stimulation

I observed that the suppression of the cellular activity upon IR stimulus is more dominant for continuous wave protocol across all layers compared to pulsed wave stimulus of lower frequencies (Figure 4.5A-C). The number of cells responding in each cortical layer was less dependent on the type of PW stimulus, while the number of unaffected cells dropped significantly compared to affected cells in the case of CW stimulus. These features suggest that the recruitment of cells is less sensitive to the pulse duration of the stimulus (in the regime down to 2 ms), but a remarkable change in tissue temperature ($\sim$ 5 °C) may activate additional heat-sensitive ion channels in the cell membrane (see Figure 4.2). Interestingly, the number of affected cells culminates in the CW stimulus protocol, where the number of cells with suppressed activity is also increasing in all layers. My results highlight the versatile behavior of the layers of the rat somatosensory cortex during IR exposure and underline the importance of neuromodulation strategies aimed at performing spatially localized, focal stimulation. However, since the Neuropixels probe was inserted at an angle, I cannot definitively rule out the possibility that the observed effects are due to distance rather than being layer-dependent. In this study, we targeted the bottom part of layer 5 (layer 5b) with the tip of the optrode because, during ketamine/xylazine anesthesia, the strongest neuronal activity is detected in infragranular cortical layers, while activity in supragranular layers is sparse. Up-states during slow oscillations typically start in layer 5, and the maximal excitation of the tissue with infrared stimulation occurs closest to the optrode tip. Therefore, we aimed for a depth of 1200 μm from the cortical surface, the approximate location of layer 5b.

5.1.1 Cell type specificity

Our observations rely on the parallel interrogation of several hundred neurons during a single optical stimulation cycle. They eventually contribute to the analysis of the individual behavior of several thousands of cortical neurons (n=7549) throughout the whole experiment. Given the cortical activity, two important and broadly described types of neurons are responsible for computational tasks. These are the putative Glu-ergic neurons, which I here refer to as principal cells, and putative GABA-ergic interneurons. Principal neurons participate in signal propagation, while interneurons are gating signaling pathways. It is important to note, that GABA-ergic interneurons exhibit a large diversity[141], and classification of these cell types and matching them to the electrophysiological response are beyond the scope of this work. I use the term interneurons

for all of these subtypes without differentiation. Based on my results, I can say that these cells can show different activity patterns upon different stimulus onsets (see Figure 4.10). Interneurons and principal cells with suppressed and increased activity are more responsive to CW stimulus than to PW stimulus (Figure 4.7D-G). Interestingly, the number of recruited neurons increases notably as I use CW stimulus, which could be partially caused by the massive change in tissue temperature (about 5 °C), and which may be mediated by the diverse distribution of heat-sensitive ion channels in the cell membrane of various type of neurons [142].

5.1.2 Effects of repeated stimulation and baseline changes

Our study also underlines the importance of the change in activity baseline after multiple repetitions of the stimulation trial. Even though the temperature gets back to its original state (see Figure 3.4), there is a long-lasting effect of the stimulation that keeps the excitability of the affected neurons in an elevated state (see Figure 4.2F). Cayce and co-workers [81] applied individual spike trains lasting 500 ms and consisting of 250 μs long pulses to evaluate the single unit response to IR ($\lambda = 1875\ nm$) stimulation in the rat visual cortex using tungsten electrodes. Although it was not highlighted in their manuscript, the repeated use of the stimulation sequence led to elevated activity of the interrogated neurons, which responded with inhibitory behavior to the illumination of the cortex. It should be noted that in their experiment, only the superficial area of the intact cortex was exposed to light, while in the current study, intracortical stimulation is assessed. Later, the same irradiation parameters were used in the macaque visual cortex, however, the effect of the repetitive use of the stimulation sequence was not demonstrated [143]. My work also extends the dataset on this potential issue, as a change in temperature is estimated and compared to the evolution of spike rate along various stimulation types. Based on my observations, I can conclude that neuronal excitability is changed for a longer period, which goes well beyond the period necessary to reach the baseline temperature again.

5.1.3 Temporal dynamics of temperature and neural activity

Figure 4.11A shows that the rise time of temperature is varying, since at higher frequencies of pulsed and also at CW stimulation longer time was necessary to get into the steady-state. For the fall time, the system got back to the baseline in similar periods. Given Figure 4.11 and 4.12, the change in the spike rate of both excited and suppressed neurons did not follow the same time scale as that of the temperature but reached the average activity around $35 - 40\ s$. This suggests that regardless of the type of evoked activity, the same molecular switches may be activated. Even though the rise time follows temperature data, the response time in individual sessions exhibits some variability. This may be associated with the difference in the spontaneous state of the affected brain region. Importantly, this average timescale remained stable during the repetition of any type of stimulation cycle (see Figure 4.11B-C and Figure 4.12B-C). It should be noted that these temporal features are calculated based on the relative change in spike rate activity for each session.

As was implied by the change in baseline activity, the gradual increase in the absolute firing rate is not fully linked to the thermal processes, but there is a cumulative effect, even though it has no clear influence on the temporal features of individual stimulation sessions. To clarify this issue, a stimulation protocol with a much longer relaxation time should be applied in a future study.

In conclusion, our work on high-density laminar electrophysiological recordings was utilized for the first time to reveal intracortical response to pulsed and continuous-wave infrared irradiation. My findings confirm that evoked action potentials exhibit layer- and cell-specific features in the rat cortex. The results also highlight the distinct cellular response to CW and PW illumination protocol. Increasing the tissue temperature with the CW stimulus, the number of responsive cells significantly increases and shows an inhibitory effect on single unit activity, unlike PW stimuli performed at lower frequencies. Suppression and increase of both interneurons and principal cell activity are more dominant for CW stimulus. My measurement of the baseline activity gives remarkable evidence of the change of cell excitability after the repetitive use of the stimuli even though changes in both tissue temperature and the firing rate have already been reestablished. My results on the response time suggest that careful considerations need to be taken during the design of the stimulus sequence to avoid cumulative effects. Finally, I found that suppression or activation of individual interneurons and principal cells with similar firing rate change can be elicited regardless of the pulsed or continuous nature of the IR illumination, which proves that each biophysical mechanism already proposed to explain IR stimulation contributes to the evoked response of cell populations. This fact further emphasizes the importance of combining electrophysiological and molecular tools to precisely characterize the excitability of cortical cells *in vivo*.

5.2 Validation of transprent SMP microECoG for chronic multimodal recording

This study demonstrates the potential of multimodal recordings combining two-photon microscopy with a transparent shape memory polymer-based microECoG device in chronically implanted mice. My results highlight the optical performance of this innovative implant and support its long-term usability for simultaneous optical and electrical interrogation of neuronal populations.

The use of SMPs, particularly thiol-ene/acrylate, as neural interface materials has only recently gained popularity. While previous studies have successfully used SMP-based intracortical probes for electrophysiological recording in rodents [60], [144], [145], our work extends the application of this material by integrating it into a transparent electrocorticography array suitable for simultaneous optical imaging. One of the major advantages of SMPs over conventional silicon-based implants is their reduced immune response, as demonstrated in previous histological studies. Our previous research introduced the first SMP-based intracranial EEG electrode array, and building on this, I now provide evidence of its compatibility with two-photon microscopy [42].

5.2.1 Optical performance

Two-photon microscopy is an invaluable tool for high-resolution fluorescence imaging in living neural tissue. Using near-infrared excitation allows deeper penetration with minimal scattering, enabling high-contrast imaging without significant off-focal fluorescence. Given the tissue-friendly properties of SMPs, our study further validates their suitability for chronic imaging applications. Using our transparent microECoG device, I successfully visualized fine neuronal structures in hippocampal slices without noticeable optical distortion, confirming its potential for high-resolution imaging.

While previous research has explored transparent multielectrode arrays in combination with two-photon microscopy, these studies have largely been limited to proof-of-concept experiments. They have not systematically evaluated the long-term stability of optical properties or the feasibility of extended multimodal imaging sessions. In addition, image quality has not been consistently monitored over time. To address this gap, we performed chronic *in vivo* imaging for up to 22 weeks after implantation, ensuring that the detected fluorescent calcium signals remained of sufficient quality to distinguish individual neuronal structures.

Our previous work was among the first to quantitatively assess optical performance in a chronic setting using a Parylene HT/ITO-based ECoG array implanted for 51 days [98]. The present study extends this timeline and shows that optical quality remains intact after 22 weeks, with no evidence of signal degradation due to SMP microECoG failure. The ability to maintain high-resolution imaging and stable fluorescence signals over this extended period underscores the robustness of our SMP-based microECoG design.

Taken together, my results confirm that the optical performance of the transparent SMP microECoG array meets the stringent requirements for chronic multimodal experiments. This SMP microECoG enables the long-term integration of two-photon microscopy with cortical electrophysiology, paving the way for future studies exploring neural dynamics in healthy and diseased states.

5.2.2 Electrophysiological recording quality

Despite the SMP microECoG's initial non-design for single-unit activity recording, I successfully captured action potentials with adequate signal quality. To enhance SUA recording, a reduction in the size of the recording sites and the distance between them, coupled with an increase in the number of channels, would optimize performance, as asserted by Khodagholy et al [146]. Reducing electrode size and spacing while increasing the number of channels enhances spatial resolution and signal clarity, which is essential for distinguishing waveform characteristics of different neuron types. However, electrodes that are too small may decrease the signal-to-noise ratio and compromise recording stability, highlighting a practical and physiological limit to miniaturization. Moreover, different neuron sizes may require electrodes of varying dimensions for optimal recording efficiency. Electrode spacing is also critical, as it affects how many channels detect the activity of a single neuron, impacting the accuracy of spike sorting algorithms. Finally, the spatial distribution and density of neurons must be considered when designing the recording

setup, as these factors influence the detectability and separation of individual cells. An enhancement in the density of recording sites would also facilitate improved localization of signal sources within the hippocampus. However, it is important to consider that increasing the density of the electrodes could limit the optical imaging field of view. Despite these challenges, the SMP microECoG, even with its current density of channels and recording site size, is capable of detecting subtle spatiotemporal changes in both electrophysiological and calcium signals during early disease progression. This study signifies the initial successful long-term utilization of a soft microelectrode grid embedded in a hippocampal cranial chamber, enabling the chronic recording of action potentials, in addition to optical access for calcium imaging through the transparent substrate layer. The implanted shape memory polymer thiol-ene/acrylate microECoG yielded stable electrophysiological signals from the hippocampus, including MUAs, and SUAs, over several weeks, maintaining transparency for two-photon imaging for up to six months in GCaMP6f-expressing transgenic mice.

5.3 Considerations for clinical translation and limitations

While the findings of this dissertation provide valuable insight into the modulation and monitoring of cortical activity in rodents, translating these technologies to human use presents several challenges and considerations. A key limitation of infrared neuromodulation in human applications is the variability in brain size and tissue properties. The penetration of infrared light is constrained by the processes of scattering and absorption within biological tissue [147]. In contrast to the relatively thin cortex of rodents, the human cortex is significantly thicker and covered by a denser skull and dura. These disparities can significantly attenuate the delivered light, thereby reducing both efficacy and spatial resolution. Furthermore, the thermal safety window must be reconsidered for human applications. Repeated or prolonged exposure to infrared light has been demonstrated to pose a greater risk of tissue heating in humans due to reduced heat dissipation and differences in vascular perfusion. Clinical use would therefore require optimized delivery mechanisms, along with real-time temperature monitoring and adaptive feedback control to prevent unintended thermal effects. Physiological differences also impact the response to infrared stimulation. Human neurons differ in their electrophysiological properties and ion channel expression, particularly thermosensitive TRP channels, which are crucial mediators of infrared-induced effects [148], [149]. These differences imply that stimulation parameters cannot be directly translated from rodent models. For instance, human neurons may require higher radiant exposure or modified pulse patterns to achieve comparable modulation. Validation in non-human primates and human brain slices would be critical before pursuing clinical applications.

The transparent shape memory polymer-based microECoG array developed in this study demonstrates considerable potential for future human applications. The material's flexibility and optical transparency render it particularly well-suited for surface cortical recording during neurosurgical procedures and for the development of long-term brain-computer interfaces. However, adapting this technology for clinical use is a complex

undertaking. To scale the array to human cortical dimensions, it is necessary to increase both the coverage area and the channel count while preserving mechanical softness and transparency. Achieving this aim will require further material engineering to ensure that the device is durable, flexible, and biocompatible over extended implantation periods. From a functional standpoint, signal fidelity and spatial resolution may degrade due to increased cortical curvature, dura thickness, and brain movement in humans. In contrast to the relatively uncomplicated motion of rodents, the human brain is subject to more substantial micromotion, which has the potential to affect signal stability [150].

5.4 Generalizability of layer- and cell-type-specific responses

While the present study demonstrates distinct layer- and cell-type-specific responses to infrared stimulation in the rat somatosensory cortex, the extent to which these findings can be generalized to other model systems remains an important consideration. Significant differences in cortical architecture, neuron density, and the distribution of thermosensitive ion channels exist between species. For instance, the human cortex possesses expanded supragranular layers and a more diverse population of inhibitory interneurons than rodents, which may alter both the spatial and temporal dynamics of infrared-induced neuromodulation. Electrophysiological properties exhibit marked differences as well. Human pyramidal neurons manifest slower h-current kinetics and longer integration times in comparison to rodent neurons. Such physiological distinctions influence responsiveness to stimulation and may lead to divergent patterns of activation, suppression, or plasticity. Furthermore, the organization and connectivity of large-scale cortical networks in primates are more complex, potentially impacting the integration and propagation of stimulation-evoked responses.

To ascertain the broader applicability of these findings, future research should entail comparative analyses in species with more human-like cortical structures, such as non-human primates, or utilize human brain slices where feasible. Ideally, these studies should be performed under awake and behaviorally relevant conditions to assess whether the observed effects are conserved features of cortical processing or limited to the anesthetized rodent somatosensory system.

5.5 Potential applications

The findings of this dissertation propose multiple applications in both fundamental neuroscience and translational research. The two primary research directions that have been investigated, infrared neuromodulation and transparent shape memory polymer-based microelectrocorticography, hold significant promise for the advancement of brain interface technologies and experimental neuroscience.

In the context of infrared neuromodulation, the observed layer- and cell-type-specific effects of pulsed and continuous-wave infrared stimulation serve as a foundational basis for the development of more targeted and minimally invasive brain stimulation techniques. This approach has the potential to be applied in therapeutic contexts, such as modulating

dysfunctional circuits in neurological disorders like epilepsy, chronic pain, or movement disorders. The contact-free nature of infrared light makes it a suitable candidate for neuromodulation without introducing implants into deep tissue. Furthermore, the capacity to precisely modify excitability at specific cortical depths provides novel opportunities for non-electrical, spatially refined stimulation. A comprehensive understanding of the influence of diverse stimulation protocols on neuronal activity over time is essential for the development of safe and effective stimulation parameters for chronic or closed-loop systems, where stimulation adapts to ongoing neural responses in real time.

The SMP-based transparent microECoG array, which has been validated for long-term simultaneous optical and electrophysiological recordings, has the potential to lead to a broad range of applications in the field of neuroscience research. Its capacity to preserve optical clarity and stable electrical performance over an extended period makes it particularly beneficial for the study of chronic conditions, such as epilepsy and neurodegenerative diseases. Furthermore, the system is particularly well-suited for high-throughput drug screening, where real-time monitoring of calcium signals and electrophysiological activity can provide immediate feedback on the efficacy of the compounds under investigation. The device's transparency and flexibility make it well-suited for studying synaptic plasticity, developmental changes, and circuit remodeling over time. Despite the fact that the current design was not optimized for single-unit recordings, the successful capture of action potentials suggests its potential for further development in high-resolution brain-machine interfaces.

The techniques developed and tested in this work collectively constitute a versatile platform for probing and manipulating cortical activity with high spatial and temporal precision. The combined utilization of these approaches in future studies has the potential to substantially enhance our capacity to observe, understand, and influence neural circuits in both health and disease.

6 Conclusions

This dissertation addresses two central challenges in current neuroscientific research: the need for precise, gene-free neuromodulation strategies, such as infrared neural stimulation, and the development of flexible, transparent neural interfaces that can support long-term, multimodal recordings. Through a combination of *in vivo* electrophysiology, two-photon imaging, and device engineering, this work advances our understanding of the cortex's response to infrared stimulation and the practical development of biocompatible neural recording systems.

6.1 Addressing objective 1: Characterizing layer- and cell-type-specific cortical responses to infrared stimulation

I used high-density laminar electrophysiological recordings with a Neuropixels probe to examine the intracortical response to pulsed and continuous-wave infrared irradiation in adult Wistar rats ($n = 8$). In this study, I recorded the activity of 7,549 single-units from anesthetized rats during pulsed (1 Hz, 10 Hz, 50 Hz, 100 Hz, 500 Hz) and continuous-wave infrared light stimulation. The stimulation was applied using an optrode device positioned in layer 5 of the somatosensory cortex. I focused on investigating the effects of the stimulation on the firing rate of cells across different cortical layers and cell types, as well as exploring the temporal dynamics of the neuronal response.

Thesis group I.

Thesis I.1. I showed that continuous-wave infrared stimulation leads to a greater proportion of cortical neurons exhibiting suppressed firing compared to pulsed wave stimulation, which more commonly induced increased activity. Neurons with increased firing rates nearly doubled their activity during stimulation, while suppressed neurons exhibited an average reduction of about 40%. Additionally, CW stimulation induced significantly larger changes in firing rates than pulsed wave stimulation across the tested frequencies.

Thesis I.2. I determined that the effect induced by continuous infrared stimulation depends on which cortical layer is examined. I observed significantly greater suppression in the superficial and input layers (layers 2/3/4) compared to the deeper layers (layers 5 and 6).

Thesis I.3. I determined that the stimulation frequency significantly influences the activity of interneurons and principal cells: at higher stimulation frequencies, activity

increased in the excited cells and decreased in the suppressed cells. In the case of interneurons, more cells showed suppressed activity, while in the case of principal cells, increased activity was observed in the majority of cells.

Thesis I.4. I showed that in the case of continuous infrared stimulation, the rise time of the firing rate was significantly longer than in the case of pulsed stimulation. The fall times were consistently faster in comparison. This points to the unique temporal dynamics of neural responses to heating. The rise time remained consistent across the five stimulation periods.

Publications related to the thesis points

The publication related to this thesis group is: [J1]
The conference posters related to this thesis group are: [P1]–[P3]

6.2 Addressing objectives 2 and 3: Evaluating the optical and chronic recording performance of a transparent microECoG interface

The second focus is the development and evaluation of a transparent, flexible, thiol-ene/acrylate shape memory polymer-based microelectrocorticography device. This SMP microECoG enables two-photon optical imaging and electrophysiological recording simultaneously over long periods. The SMP microECoG exhibited high optical clarity with minimal distortion during imaging and demonstrated stable single-unit spike detection in chronic hippocampal recordings lasting at least seven weeks. This confirms its suitability for long-term neural monitoring.

A transparent microECoG device was presented using thiol-ene/acrylate shape memory polymer as a biocompatible flexible transparent polymer substrate and Parylene C encapsulating material with gold and SIROF as a conductive layer. This array features 115 μm diameter recording sites, which are spaced 400 μm apart. I assessed the impact of an SMP-based microECoG device on two-photon imaging by analyzing fluorescent microbeads and hippocampal slices in *in vitro* images, and the relative fluorescent intensity change in mice somatosensory (n=3) cortex *in vivo*, for 22 weeks. I also explored the SMP microECoG's ability to record single-unit activity from the mice hippocampus (n=7) over extended periods.

Thesis group II.

Thesis II.1. Using fluorescent microbeads, I showed that the SMP-based microECoG device produces no significant optical distortion on two-photon microscopy images. Additionally, dendritic diameters in hippocampal slices remained consistent across imaging depths, indicating that fine neuronal structures can be visualized with high fidelity

through the device, preserving the optical clarity required for high-resolution, multimodal imaging.

Thesis II.2. I demonstrated that relative intensity changes in GCaMP6f-labeled neurons relative to background fluorescence were consistently visible over 22 weeks, and no significant differences were observed during two-photon imaging of awake, freely moving mice. My results indicate that the microECoG device enables long-term stable, high-resolution multimodal imaging without significant optical signal degradation.

Thesis II.3. I conclude that SMP microECoG has reliable, long-term electrophysiological recording capabilities, including the detection of single-cell activity, for at least seven weeks, based on *in vivo* data.

Publications related to the thesis points

The publications related to this thesis group are: [J2], [J3]
The conference posters related to this thesis group are: [P4], [P5]

7 Summary

This dissertation explores state-of-the-art neurotechnologies that can precisely modulate and monitor brain activity. These technologies have applications in the treatment of neurodegenerative and neurological disorders. The first part of the study focuses on infrared neural stimulation, a minimally invasive technique that uses localized heating to influence neuronal behavior. Using high-density laminar electrodes in anesthetized rats, the results show that pulsed INS enhances neuronal firing, especially in superficial cortical layers, while continuous-wave INS suppresses activity. These results suggest that heat-sensitive ion channels (e.g., TRPV and TREK) and membrane biophysics are essential to INS mechanisms.

The second part of the study evaluates a microelectrocorticography device made of shape memory polymers that is designed for long-term, high-resolution neural recording. The device is compatible with two-photon microscopy and enables simultaneous optical imaging and electrophysiological recordings without significant optical distortion. The device successfully detects single-unit spikes for at least seven weeks, demonstrating its potential for reliable long-term neural monitoring.

Together, these studies advance the field of neurotechnology by providing novel insights into neuromodulation and neural interface design with implications for basic neuroscience research and clinical intervention.

7.1 Future outlook

Based on these findings, several potential areas of future research are emerging. Regarding neuromodulation, further investigation is needed into the biophysical and molecular mechanisms underlying changes in infrared-induced neural activity. Specifically, future work should aim to map the roles of thermosensitive ion channels, such as TRPV1, TRPV4, and TREK. It should also explore how changes in membrane capacitance contribute to spike modulation during rapid, localized heating. Understanding these mechanisms is essential for optimizing the selectivity, efficacy, and safety of INS for therapeutic use.

Regarding device engineering, efforts should be made to redesign the mmicroECoG array to increase contact density and spatial resolution. This will enhance the SMP microECoG's ability to detect and isolate single-unit activity across wider cortical areas. Additionally, developing a scaled-up, primate-compatible version of the SMP microECoG would be a significant step toward human applications. This platform could enable chronic optical and electrophysiological monitoring in non-human primates, supporting research into neurological disorders and neuromodulation therapies at a scale that is more directly relevant to the human brain.

Together, these proposed directions would extend the impact of this work and bring us closer to achieving minimally invasive, high-precision neuromodulation and monitoring systems for basic neuroscience and clinical translation.

Acknowledgements

First and foremost, I would like to express my deepest gratitude to my late supervisor, *Dr. Zoltán Fekete*, whose guidance, wisdom, and unfailing support were integral to shaping this research and dissertation. His passing was a profound loss and I am forever grateful for the time and mentorship he provided.

I would like to express my sincere gratitude to my current supervisors, *Dr. Ágoston Csaba Horváth* and *Dr. Kristóf Iván*, for their support and guidance during the last part of my research. Their insights, patience, and encouragement were essential to the completion of this thesis.

I would also like to thank the members of the Implantable Microsystems Research Group, including *Dr. Ágoston Csaba Horváth*, *Dr. Ágnes Szabó*, *Ákos Mórocz*, and *Levente Víg*, for their collaboration, advice, and stimulating discussions that have added to my research experience.

I am grateful to my collaborators, *Dr. Richárd Fiáth*, *Gábor Juhász*, *Miklós Madarász*, *Dr. Zsuzsanna Helyes* and *Dr. Katalin Kovács-Rozmer* for their contributions, expertise, and dedication.

Special thanks to the Doctoral School, especially *Prof. Gábor Szederkényi* and *Prof. Sándor Pongor*, for providing an inspiring academic environment that fostered my growth as a researcher. I am also grateful to *Dr. Tivadarné Vida* for her administrative support, which ensured a smooth and organized process throughout my PhD. journey.

Finally, I would like to express my sincere gratitude to my family and friends for their constant encouragement and support. In particular, I am deeply grateful to my husband, *Gábor Dániel Balogh*, for his belief in me, his patience and his love throughout this journey. Without his support, this achievement would not have been possible.

This dissertation is dedicated to all those who have supported me in this journey, and I am deeply grateful to each and every one of you.

Author's list of publications

List of journal publications

[J1] **Z. Balogh-Lantos**, R. Fiáth, Á. C. Horváth, and Z. Fekete, "High density laminar recordings reveal cell type and layer specific responses to infrared neural stimulation in the rat neocortex", *Scientific Reports*, vol. 14, no. 1, p. 31 523, 2024 (cit. on pp. 37, 45, 46, 58, 61, 62, 65–67, 69–74, 88).

[J2] G. Juhász, M. Madarász, B. Szmola, F. Fedor, **Z. Balogh-Lantos**, Á. Szabó, B. Rózsa, and Z. Fekete, "Hippocampal recording with a soft microelectrode array in a cranial window imaging scheme: A validation study", *Scientific Reports*, vol. 14, no. 1, p. 24 585, 2024 (cit. on pp. 42, 55, 79, 89).

[J3] Á. Szabó, M. Madarász, **Z. Lantos**, A. Zátonyi, V. Danda, L. Spurgin, C. Manz, B. Rózsa, and Z. Fekete, "Transparent thiol-ene/acrylate-based microecog devices used for concurrent recording of fluorescent calcium signals and electrophysiology in awake animals", *Advanced Materials Interfaces*, vol. 9, no. 25, p. 2 200 729, 2022 (cit. on pp. 76, 77, 89).

[J4] R. Matta, **Z. Balogh-Lantos**, Z. Fekete, M. Baca, A. Kaszas, D. Moreau, and R. P. O'Connor, "A flexible, implantable, bioelectronic electroporation device for targeted ablation of seizure foci in the mouse brain", *Sensors*, vol. 25, no. 1, p. 4, 2024.

[J5] Á. C. Horváth, Á. Mórocz, B. Csomai, Á. Szabó, **Z. Balogh-Lantos**, P. Fürjes, E. Z. Tóth, R. Fiáth, and Z. Fekete, "Silicon optrode with a micromirror-tip providing tunable beam profile during infrared neuromodulation of the rat neocortex", *Advanced Materials Technologies*, vol. 9, no. 20, p. 2 400 044, 2024.

List of conference posters

[P1] **Z. Lantos**, R. Fiáth, C. Horváth Á, and Z. Fekete, "Intracortical effects of continuous infrared neural stimulation", 2023, Poster presented at the Joined neuroscience meeting of the Hungarian Neuroscience Society and the Austrian Neuroscience Association, Budapest, Hungary (cit. on p. 88).

[P2] **Z. Balogh-Lantos**, R. Fiáth, C. Horváth Á, and Z. Fekete, "Cell- and layer-type specific intracortical effects of continuous infrared neural stimulation revealed by high-density laminar recordings in the rat neocortex", 2024, Poster presented at the Federation of European Neuroscience Societies Forum, Vienna, Austria (cit. on p. 88).

[P3] **Z. Balogh-Lantos**, R. Fiáth, C. Horváth Á, and Z. Fekete, "Cell- and layer-type specific intracortical effects of continuous infrared neural stimulation revealed by high-density laminar recordings in the rat neocortex", 2024, Poster presented at the International Neuroscience Conference, Pécs, Hungary (cit. on p. 88).

[P4] **Z. Lantos**, Á. Szabó, F. Fedor, A. Zátonyi, M. Madarász, L. T., and Z. Fekete, "Shape memory polymer based transparent electrode array for long-term multimodal neuroimaging", 2022, Poster presented at the Federation of European Neuroscience Societies Forum, Paris, France (cit. on p. 89).

[P5] **Z. Lantos**, Á. Szabó, F. Fedor, A. Zátonyi, M. Madarász, L. T., and Z. Fekete, "Shape memory polymer based transparent electrode array for long-term multimodal neuroimaging", 2022, Poster presented at the International Neuroscience Meeting, Budapest, Hungary (cit. on p. 89).

[P6] **Z. Balogh-Lantos**, R. Fiáth, C. Horváth Á, K. Kovács-Rozmer, Z. Helyes, and Z. Fekete, "Cell- and layer-specific roles of trpv1 ion channels in infrared neurostimulation: Insights from high-density laminar recordings in the mouse neocortex", 2025, Poster presented at the Annual Meeting of the Hungarian Neuroscience Society, Debrecen, Hungary.

[P7] M. Madarász, **Z. Lantos**, B. Szmola, Á. Szabó, B. Rózsa, Z. Fekete, and G. Juhász, "Concurrent imaging of calcium signals and recording of electrophysiology in the hippocampus of awake mouse", 2023, Poster presented at the Joined neuroscience meeting of the Hungarian Neuroscience Society and the Austrian Neuroscience Association, Budapest, Hungary.

List of references related to the dissertation

[1] P. Scheltens, K. Blennow, M. M. Breteler, B. De Strooper, G. B. Frisoni, S. Salloway, and W. M. Van der Flier, "Alzheimer's disease", *The Lancet*, vol. 388, no. 10043, pp. 505–517, 2016 (cit. on p. 10).

[2] L. V. Kalia and A. E. Lang, "Parkinson's disease", *The Lancet*, vol. 386, no. 9996, pp. 896–912, 2015 (cit. on p. 10).

[3] R. D. Thijs, R. Surges, T. J. O'Brien, and J. W. Sander, "Epilepsy in adults", *The lancet*, vol. 393, no. 10172, pp. 689–701, 2019 (cit. on p. 10).

[4] J. Olesen, A. Gustavsson, M. Svensson, H.-U. Wittchen, B. Jönsson, C. S. Group, and E. B. Council, "The economic cost of brain disorders in europe", *European journal of neurology*, vol. 19, no. 1, pp. 155–162, 2012 (cit. on p. 10).

[5] S. D. Skaper, L. Facci, M. Zusso, and P. Giusti, "An inflammation-centric view of neurological disease: Beyond the neuron", *Frontiers in cellular neuroscience*, vol. 12, p. 72, 2018 (cit. on p. 10).

[6] R. A. Nixon and D.-S. Yang, "Autophagy and neuronal cell death in neurological disorders", *Cold Spring Harbor perspectives in biology*, vol. 4, no. 10, a008839, 2012 (cit. on p. 10).

[7] M. Nimgampalle, H. Chakravarthy, S. Sharma, S. Shree, A. R. Bhat, J. A. Pradeepkiran, and V. Devanathan, "Neurotransmitter systems in the etiology of major neurological disorders: Emerging insights and therapeutic implications", *Ageing Research Reviews*, p. 101 994, 2023 (cit. on p. 10).

[8] H. Raju and P. Tadi, "Neuroanatomy, somatosensory cortex", in *StatPearls [Internet]*, StatPearls Publishing, 2022 (cit. on p. 10).

[9] M. Bushnell, G. Duncan, R. Hofbauer, B. Ha, J.-I. Chen, and B. Carrier, "Pain perception: Is there a role for primary somatosensory cortex?", *Proceedings of the National Academy of Sciences*, vol. 96, no. 14, pp. 7705–7709, 1999 (cit. on p. 10).

[10] H. Eichenbaum, T. Otto, and N. J. Cohen, "The hippocampus—what does it do?", *Behavioral and neural biology*, vol. 57, no. 1, pp. 2–36, 1992 (cit. on p. 10).

[11] L. A. Fogwe, V. Reddy, and F. B. Mesfin, "Neuroanatomy, hippocampus", 2018 (cit. on p. 10).

[12] K. Saladin, *Human anatomy*. New York: Mc Graw Hill, 2016 (cit. on p. 11).

[13] N. L. Strominger, R. J. Demarest, and L. B. Laemle, "Cerebral cortex", in *Noback's Human Nervous System, Seventh Edition: Structure and Function*. Totowa, NJ: Humana Press, 2012, pp. 429–451, ISBN: 978-1-61779-779-8. DOI: 10.1007/978-1-61779-779-8_25. [Online]. Available: https://doi.org/10.1007/978-1-61779-779-8_25 (cit. on p. 11).

[14] K. Brodmann, *Vergleichende Lokalisationslehre der Grosshirnrinde in ihren Prinzipien dargestellt auf Grund des Zellenbaues*. Barth, 1909 (cit. on p. 11).

[15] D. B. Tower and J. P. Schadé, *Structure and function of the cerebral cortex*. Elsevier Publishing Company, 1960 (cit. on p. 12).

[16] G. Meyer, A. M. Goffinet, and A. Fairén, "What is a cajal–retzius cell? a reassessment of a classical cell type based on recent observations in the developing neocortex", *Cerebral Cortex*, vol. 9, no. 8, pp. 765–775, 1999 (cit. on p. 12).

[17] M. Judaš and M. Pletikos, "The discovery of the subpial granular layer in the human cerebral cortex", *Translational Neuroscience*, vol. 1, no. 3, pp. 255–260, 2010 (cit. on p. 12).

[18] C. D. Gilbert and M. Sigman, "Brain states: Top-down influences in sensory processing", *Neuron*, vol. 54, no. 5, pp. 677–696, 2007 (cit. on p. 12).

[19] L. Cauller, "Layer i of primary sensory neocortex: Where top-down converges upon bottom-up", *Behavioural brain research*, vol. 71, no. 1-2, pp. 163–170, 1995 (cit. on p. 12).

[20] S. J. Cruikshank, O. J. Ahmed, T. R. Stevens, S. L. Patrick, A. N. Gonzalez, M. Elmaleh, and B. W. Connors, "Thalamic control of layer 1 circuits in prefrontal cortex", *Journal of Neuroscience*, vol. 32, no. 49, pp. 17 813–17 823, 2012 (cit. on p. 12).

[21] E. Jones, "The core and matrix of thalamic organization", *Neuroscience*, vol. 85, no. 2, pp. 331–345, 1998 (cit. on p. 12).

[22] S. Huang, S. J. Wu, G. Sansone, L. A. Ibrahim, and G. Fishell, "Layer 1 neocortex: Gating and integrating multidimensional signals", *Neuron*, vol. 112, no. 2, pp. 184–200, 2024 (cit. on p. 12).

[23] Y.-W. Lam and S. M. Sherman, "Functional organization of the somatosensory cortical layer 6 feedback to the thalamus", *Cerebral cortex*, vol. 20, no. 1, pp. 13–24, 2010 (cit. on p. 12).

[24] G. Buzsáki and J. J. Chrobak, "Temporal structure in spatially organized neuronal ensembles: A role for interneuronal networks", *Current opinion in neurobiology*, vol. 5, no. 4, pp. 504–510, 1995 (cit. on pp. 13, 14).

[25] P. C. Petersen, J. H. Siegle, N. A. Steinmetz, S. Mahallati, and G. Buzsáki, "Cellexplorer: A framework for visualizing and characterizing single neurons", *Neuron*, vol. 109, no. 22, pp. 3594–3608, 2021 (cit. on p. 13).

[26] M. Megıas, Z. Emri, T. Freund, and A. Gulyás, "Total number and distribution of inhibitory and excitatory synapses on hippocampal ca1 pyramidal cells", *Neuroscience*, vol. 102, no. 3, pp. 527–540, 2001 (cit. on p. 13).

[27] I. Salimi, K. M. Friel, and J. H. Martin, "Pyramidal tract stimulation restores normal corticospinal tract connections and visuomotor skill after early postnatal motor cortex activity blockade", *Journal of Neuroscience*, vol. 28, no. 29, pp. 7426–7434, 2008 (cit. on p. 13).

[28] M. Glickstein, "Golgi and cajal: The neuron doctrine and the 100th anniversary of the 1906 nobel prize", *Current Biology*, vol. 16, no. 5, R147–R151, 2006 (cit. on p. 13).

[29] Y. Kawaguchi, "Distinct firing patterns of neuronal subtypes in cortical synchronized activities", *Journal of Neuroscience*, vol. 21, no. 18, pp. 7261–7272, 2001 (cit. on pp. 13, 14).

[30] T. H. J. Waters, "Spiking patterns of neocortical l5 pyramidal neurons in vitro change with temperature", *Frontiers in cellular neuroscience*, vol. 5, p. 1, 2011 (cit. on p. 13).

[31] T. Otsuka and Y. Kawaguchi, "Firing-pattern-dependent specificity of cortical excitatory feed-forward subnetworks", *Journal of Neuroscience*, vol. 28, no. 44, pp. 11 186–11 195, 2008 (cit. on p. 13).

[32] R. N. Lemon, S. N. Baker, and A. Kraskov, "Classification of cortical neurons by spike shape and the identification of pyramidal neurons", *Cerebral cortex*, vol. 31, no. 11, pp. 5131–5138, 2021 (cit. on p. 14).

[33] M. C. Quirk, D. L. Sosulski, C. E. Feierstein, N. Uchida, and Z. F. Mainen, "A defined network of fast-spiking interneurons in orbitofrontal cortex: Responses to behavioral contingencies and ketamine administration", *Frontiers in systems neuroscience*, vol. 3, p. 735, 2009 (cit. on p. 14).

[34] R. Mozumder, S. Chung, S. Li, and C. Constantinidis, "Contributions of narrow- and broad-spiking prefrontal and parietal neurons on working memory tasks", *Frontiers in Systems Neuroscience*, vol. 18, p. 1 365 622, 2024 (cit. on p. 14).

[35] M. A. Whittington, R. D. Traub, N. Kopell, B. Ermentrout, and E. H. Buhl, "Inhibition-based rhythms: Experimental and mathematical observations on network dynamics", *International journal of psychophysiology*, vol. 38, no. 3, pp. 315–336, 2000 (cit. on p. 14).

[36] Y. Senzai and G. Buzsáki, "Physiological properties and behavioral correlates of hippocampal granule cells and mossy cells", *Neuron*, vol. 93, no. 3, pp. 691–704, 2017 (cit. on pp. 15, 42).

[37] P. Barthó, H. Hirase, L. Monconduit, M. Zugaro, K. D. Harris, and G. Buzsaki, "Characterization of neocortical principal cells and interneurons by network interactions and extracellular features", *Journal of neurophysiology*, vol. 92, no. 1, pp. 600–608, 2004 (cit. on pp. 14, 41, 66).

[38] A. L. Hodgkin and A. F. Huxley, “Action potentials recorded from inside a nerve fibre”, *Nature*, vol. 144, no. 3651, pp. 710–711, 1939 (cit. on p. 15).

[39] N. Bajaj, “Wavelets for eeg analysis”, *Wavelet theory*, vol. 11, 2020 (cit. on p. 16).

[40] C. Iber, “The aasm manual for the scoring of sleep and associated events: Rules, terminology, and technical specification”, *(No Title)*, 2007 (cit. on p. 16).

[41] J. L. Skousen, S. M. E. Merriam, O. Srivannavit, G. Perlin, K. D. Wise, and P. A. Tresco, “Reducing surface area while maintaining implant penetrating profile lowers the brain foreign body response to chronically implanted planar silicon microelectrode arrays”, in *Progress in brain research*, vol. 194, Elsevier, 2011, pp. 167–180 (cit. on pp. 17, 20).

[42] F. Z. Fedor, M. Madarász, A. Zátonyi, Á. Szabó, T. Lőrincz, V. Danda, L. Spurgin, C. Manz, B. Rózsa, and Z. Fekete, “Soft, thiol-ene/acrylate-based electrode array for long-term recording of intracranial eeg signals with improved biocompatibility in mice”, *Advanced Materials Technologies*, p. 2 100 942, 2021 (cit. on pp. 17, 22, 23, 33, 34, 82).

[43] S. Huang, Y. Liu, Y. Zhao, Z. Ren, and C. F. Guo, “Flexible electronics: Stretchable electrodes and their future”, *Advanced Functional Materials*, vol. 29, no. 6, p. 1 805 924, 2019 (cit. on p. 17).

[44] V. Viswam, M. E. J. Obien, F. Franke, U. Frey, and A. Hierlemann, “Optimal electrode size for multi-scale extracellular-potential recording from neuronal assemblies”, *Frontiers in neuroscience*, vol. 13, p. 385, 2019 (cit. on p. 18).

[45] C. Li and G. Wang, “Mems manufacturing techniques for tissue scaffolding devices”, in *Mems for Biomedical Applications*, Elsevier, 2012, pp. 192–217 (cit. on p. 18).

[46] S. M. Sze, *Semiconductor devices: physics and technology*. John wiley & sons, 2008 (cit. on pp. 18, 19).

[47] O. O. Abegunde, E. T. Akinlabi, O. P. Oladijo, S. Akinlabi, and A. U. Ude, “Overview of thin film deposition techniques”, *AIMS Materials Science*, vol. 6, no. 2, pp. 174–199, 2019 (cit. on p. 18).

[48] J.-B. Jorcin, M. E. Orazem, N. Pébère, and B. Tribollet, “Cpe analysis by local electrochemical impedance spectroscopy”, *Electrochimica Acta*, vol. 51, no. 8-9, pp. 1473–1479, 2006 (cit. on p. 18).

[49] K. R. Jessen, “Glial cells”, *The international journal of biochemistry & cell biology*, vol. 36, no. 10, pp. 1861–1867, 2004 (cit. on p. 20).

[50] A. Gilletti and J. Muthuswamy, “Brain micromotion around implants in the rodent somatosensory cortex”, *Journal of neural engineering*, vol. 3, no. 3, p. 189, 2006 (cit. on p. 20).

[51] B. D. Winslow and P. A. Tresco, “Quantitative analysis of the tissue response to chronically implanted microwire electrodes in rat cortex”, *Biomaterials*, vol. 31, no. 7, pp. 1558–1567, 2010 (cit. on p. 20).

[52] V. S. Polikov, P. A. Tresco, and W. M. Reichert, "Response of brain tissue to chronically implanted neural electrodes", *Journal of neuroscience methods*, vol. 148, no. 1, pp. 1–18, 2005 (cit. on pp. 20, 21).

[53] R. Biran, D. C. Martin, and P. A. Tresco, "Neuronal cell loss accompanies the brain tissue response to chronically implanted silicon microelectrode arrays", *Experimental neurology*, vol. 195, no. 1, pp. 115–126, 2005 (cit. on p. 20).

[54] B. D. Winslow, M. B. Christensen, W.-K. Yang, F. Solzbacher, and P. A. Tresco, "A comparison of the tissue response to chronically implanted parylene-c-coated and uncoated planar silicon microelectrode arrays in rat cortex", *Biomaterials*, vol. 31, no. 35, pp. 9163–9172, 2010 (cit. on p. 20).

[55] S. M. Wellman and T. D. Kozai, *Understanding the inflammatory tissue reaction to brain implants to improve neurochemical sensing performance*, 2017 (cit. on p. 21).

[56] L. Grand, A. Pongrácz, É. Vázsonyi, G. Márton, D. Gubán, R. Fiáth, B. P. Kerekes, G. Karmos, I. Ulbert, and G. Battistig, "A novel multisite silicon probe for high quality laminar neural recordings", *Sensors and Actuators A: Physical*, vol. 166, no. 1, pp. 14–21, 2011 (cit. on p. 21).

[57] F. Vitale, D. G. Vercosa, A. V. Rodriguez, S. S. Pamulapati, F. Seibt, E. Lewis, J. S. Yan, K. Badhiwala, M. Adnan, G. Royer-Carfagni, *et al.*, "Fluidic microactuation of flexible electrodes for neural recording", *Nano letters*, vol. 18, no. 1, pp. 326–335, 2018 (cit. on p. 21).

[58] K. A. Sillay, P. Rutecki, K. Cicora, G. Worrell, J. Drazkowski, J. J. Shih, A. D. Sharan, M. J. Morrell, J. Williams, and B. Wingeier, "Long-term measurement of impedance in chronically implanted depth and subdural electrodes during responsive neurostimulation in humans", *Brain stimulation*, vol. 6, no. 5, pp. 718–726, 2013 (cit. on p. 21).

[59] A. Lecomte, E. Descamps, and C. Bergaud, "A review on mechanical considerations for chronically-implanted neural probes", *Journal of neural engineering*, vol. 15, no. 3, p. 031 001, 2018 (cit. on p. 21).

[60] A. Zátonyi, G. Orbán, R. Modi, G. Márton, D. Meszéna, I. Ulbert, A. Pongrácz, M. Ecker, W. Voit, A. Joshi-Imre, *et al.*, "A softening laminar electrode for recording single unit activity from the rat hippocampus", *Scientific reports*, vol. 9, no. 1, pp. 1–13, 2019 (cit. on pp. 21, 33, 82).

[61] L. Grand, L. Wittner, S. Herwik, E. Göthelid, P. Ruther, S. Oscarsson, H. Neves, B. Dombovári, R. Csercsa, G. Karmos, *et al.*, "Short and long term biocompatibility of neuroprobes silicon probes", *Journal of neuroscience methods*, vol. 189, no. 2, pp. 216–229, 2010 (cit. on p. 21).

[62] B. Markovsky. "Basics of impedance spectroscopy", Bar-Ilan University. (), [Online]. Available: `http://inrep.org.il/wp-content/uploads/2017/07/EIS-lecture-Prof.-B.-Markovsky.pdf` (cit. on p. 22).

[63] W. Li, Q. Y. Tang, A. D. Jadhav, A. Narang, W. X. Qian, P. Shi, and S. W. Pang, "Large-scale topographical screen for investigation of physical neural-guidance cues", *Scientific reports*, vol. 5, p. 8644, 2015 (cit. on p. 22).

[64] G. Piret, C. Hébert, J.-P. Mazellier, L. Rousseau, E. Scorsone, M. Cottance, G. Lissorgues, M. O. Heuschkel, S. Picaud, P. Bergonzo, *et al.*, "3d-nanostructured boron-doped diamond for microelectrode array neural interfacing", *Biomaterials*, vol. 53, pp. 173–183, 2015 (cit. on p. 22).

[65] E. Azemi, G. T. Gobbel, and X. T. Cui, "Seeding neural progenitor cells on silicon-based neural probes", *Journal of neurosurgery*, vol. 113, no. 3, pp. 673–681, 2010 (cit. on p. 22).

[66] A. Sridharan, J. K. Nguyen, J. R. Capadona, and J. Muthuswamy, "Compliant intracortical implants reduce strains and strain rates in brain tissue in vivo", *Journal of neural engineering*, vol. 12, no. 3, p. 036 002, 2015 (cit. on p. 23).

[67] E. N. Zhang, J.-P. Clément, A. Alameri, A. Ng, T. E. Kennedy, and D. Juncker, "Mechanically matched silicone brain implants reduce brain foreign body response", *Advanced Materials Technologies*, vol. 6, no. 3, p. 2 000 909, 2021 (cit. on p. 23).

[68] M. Becquerel, "Mémoire sur les effets électriques produits sous l'influence des rayons solaires", *Comptes rendus hebdomadaires des séances de l'Académie des sciences*, vol. 9, pp. 561–567, 1839 (cit. on p. 23).

[69] H. Hertz, "Ueber einen einfluss des ultravioletten lichtes auf die electrische entladung", *Annalen der Physik*, vol. 267, no. 8, pp. 983–1000, 1887 (cit. on p. 24).

[70] T. D. Kozai and A. L. Vazquez, "Photoelectric artefact from optogenetics and imaging on microelectrodes and bioelectronics: New challenges and opportunities", *Journal of materials chemistry B*, vol. 3, no. 25, pp. 4965–4978, 2015 (cit. on pp. 24, 25).

[71] "Band gap". (), [Online]. Available: `https://energyeducation.ca/encyclopedia/Band_gap#cite_note-3` (visited on 02/20/2025) (cit. on p. 24).

[72] H. Cagnan, T. Denison, C. McIntyre, and P. Brown, "Emerging technologies for improved deep brain stimulation", *Nature biotechnology*, vol. 37, no. 9, pp. 1024–1033, 2019 (cit. on pp. 26, 29).

[73] J. Deubner, P. Coulon, and I. Diester, "Optogenetic approaches to study the mammalian brain", *Current opinion in structural biology*, vol. 57, pp. 157–163, 2019 (cit. on pp. 26, 29).

[74] Z. Fekete, Á. C. Horváth, and A. Zátonyi, "Infrared neuromodulation: A neuroengineering perspective", *Journal of Neural Engineering*, vol. 17, no. 5, p. 051 003, 2020 (cit. on pp. 26, 29).

[75] A. Ping, L. Pan, J. Zhang, K. Xu, K. E. Schriver, J. Zhu, and A. W. Roe, "Targeted optical neural stimulation: A new era for personalized medicine", *The Neuroscientist*, vol. 29, no. 2, pp. 202–220, 2023 (cit. on p. 26).

[76] J. Wells, C. Kao, E. D. Jansen, P. Konrad, and A. Mahadevan-Jansen, "Application of infrared light for in vivo neural stimulation", *Journal of biomedical optics*, vol. 10, no. 6, pp. 064 003–064 003, 2005 (cit. on pp. 26, 29).

[77] M. G. Shapiro, K. Homma, S. Villarreal, C.-P. Richter, and F. Bezanilla, "Infrared light excites cells by changing their electrical capacitance", *Nature communications*, vol. 3, no. 1, p. 736, 2012 (cit. on pp. 26, 27, 29).

[78] Q. Xia and T. Nyberg, "Inhibition of cortical neural networks using infrared laser", *Journal of biophotonics*, vol. 12, no. 7, e201800403, 2019 (cit. on p. 26).

[79] M. Ganguly, J. B. Ford, J. Zhuo, M. T. McPheeters, M. W. Jenkins, H. J. Chiel, and E. D. Jansen, "Voltage-gated potassium channels are critical for infrared inhibition of action potentials: An experimental study", *Neurophotonics*, vol. 6, no. 4, pp. 040 501–040 501, 2019 (cit. on pp. 26, 27).

[80] J. B. Ford, M. Ganguly, J. Zhuo, M. T. McPheeters, M. W. Jenkins, H. J. Chiel, and E. D. Jansen, "Optimizing thermal block length during infrared neural inhibition to minimize temperature thresholds", *Journal of Neural Engineering*, vol. 18, no. 5, p. 056 016, 2021 (cit. on p. 26).

[81] J. M. Cayce, R. M. Friedman, E. D. Jansen, A. Mahavaden-Jansen, and A. W. Roe, "Pulsed infrared light alters neural activity in rat somatosensory cortex in vivo", *Neuroimage*, vol. 57, no. 1, pp. 155–166, 2011 (cit. on pp. 26, 29, 81).

[82] A. G. Xu, M. Qian, F. Tian, B. Xu, R. M. Friedman, J. Wang, X. Song, Y. Sun, M. M. Chernov, J. M. Cayce, *et al.*, "Focal infrared neural stimulation with high-field functional mri: A rapid way to map mesoscale brain connectomes", *Science advances*, vol. 5, no. 4, eaau7046, 2019 (cit. on p. 26).

[83] Á. C. Horváth, S. Borbély, Ö. C. Boros, L. Komáromi, P. Koppa, P. Barthó, and Z. Fekete, "Infrared neural stimulation and inhibition using an implantable silicon photonic microdevice", *Microsystems & nanoengineering*, vol. 6, no. 1, p. 44, 2020 (cit. on pp. 26, 27, 36).

[84] M. Meneghetti, J. Kaur, K. Sui, J. F. Sørensen, R. W. Berg, and C. Markos, "Soft monolithic infrared neural interface for simultaneous neurostimulation and electrophysiology", *Light: Science & Applications*, vol. 12, no. 1, p. 127, 2023 (cit. on p. 26).

[85] E. Albert, J. M. Bec, G. Desmadryl, K. Chekroud, C. Travo, S. Gaboyard, F. Bardin, I. Marc, M. Dumas, G. Lenaers, *et al.*, "Trpv4 channels mediate the infrared laser-evoked response in sensory neurons", *Journal of neurophysiology*, vol. 107, no. 12, pp. 3227–3234, 2012 (cit. on p. 26).

[86] M. J. Caterina and D. Julius, "The vanilloid receptor: A molecular gateway to the pain pathway", *Annual review of neuroscience*, vol. 24, no. 1, pp. 487–517, 2001 (cit. on p. 26).

[87] A. M. Peier, A. J. Reeve, D. A. Andersson, A. Moqrich, T. J. Earley, A. C. Hergarden, G. M. Story, S. Colley, J. B. Hogenesch, P. McIntyre, *et al.*, "A heat-sensitive trp channel expressed in keratinocytes", *Science*, vol. 296, no. 5575, pp. 2046–2049, 2002 (cit. on p. 26).

[88] M. Nazıroglu, "Trpv1 channel: A potential drug target for treating epilepsy", *Current neuropharmacology*, vol. 13, no. 2, pp. 239–247, 2015 (cit. on p. 27).

[89] J. Lu, W. Zhou, F. Dou, C. Wang, and Z. Yu, "Trpv1 sustains microglial metabolic reprogramming in alzheimer's disease", *EMBO reports*, vol. 22, no. 6, e52013, 2021 (cit. on p. 27).

[90] J. Yuan, H. Liu, H. Zhang, T. Wang, Q. Zheng, and Z. Li, "Controlled activation of trpv1 channels on microglia to boost their autophagy for clearance of alpha-synuclein and enhance therapy of parkinson's disease (adv. mater. 11/2022)", *Advanced Materials*, vol. 34, no. 11, p. 2 270 088, 2022 (cit. on p. 27).

[91] L. Pan, A. Ping, K. E. Schriver, A. W. Roe, J. Zhu, and K. Xu, "Infrared neural stimulation in human cerebral cortex", *Brain Stimulation*, vol. 16, no. 2, pp. 418–430, 2023 (cit. on p. 27).

[92] A. R. Duke, M. W. Jenkins, H. Lu, J. M. McManus, H. J. Chiel, and E. D. Jansen, "Transient and selective suppression of neural activity with infrared light", *Scientific reports*, vol. 3, no. 1, p. 2600, 2013 (cit. on p. 27).

[93] Z. Fekete, M. Csernai, K. Kocsis, Á. C. Horváth, A. Pongrácz, and P. Barthó, "Simultaneous in vivo recording of local brain temperature and electrophysiological signals with a novel neural probe", *Journal of Neural Engineering*, vol. 14, no. 3, p. 034 001, 2017 (cit. on p. 27).

[94] J. Zhuo, C. E. Weidrick, Y. Liu, M. A. Moffitt, E. D. Jansen, H. J. Chiel, and M. W. Jenkins, "Selective infrared neural inhibition can be reproduced by resistive heating", *Neuromodulation: Technology at the Neural Interface*, 2023 (cit. on p. 27).

[95] M. Kiss, P. Földesy, and Z. Fekete, "Optimization of a michigan-type silicon microprobe for infrared neural stimulation", *Sensors and Actuators B: Chemical*, vol. 224, pp. 676–682, 2016 (cit. on p. 27).

[96] Á. C. Horváth, Ö. C. Boros, S. Beleznai, Ö. Sepsi, P. Koppa, and Z. Fekete, "A multimodal microtool for spatially controlled infrared neural stimulation in the deep brain tissue", *Sensors and Actuators B: Chemical*, vol. 263, pp. 77–86, 2018 (cit. on p. 27).

[97] Á. C. Horváth, S. Borbély, F. Mihók, P. Fürjes, P. Barthó, and Z. Fekete, "Histological and electrophysiological evidence on the safe operation of a sharp-tip multimodal optrode during infrared neuromodulation of the rat cortex", *Scientific Reports*, vol. 12, no. 1, p. 11 434, 2022 (cit. on pp. 27, 35, 36, 57).

[98] A. Zátonyi, M. Madarász, Á. Szabó, T. Lőrincz, R. Hodován, B. Rózsa, and Z. Fekete, "Transparent, low-autofluorescence microecog device for simultaneous ca2+ imaging and cortical electrophysiology in vivo", *Journal of Neural Engineering*, vol. 17, no. 1, p. 016 062, 2020 (cit. on pp. 30, 39, 83).

[99] E. E. Sutter, "The brain response interface: Communication through visually-induced electrical brain responses", *Journal of Microcomputer Applications*, vol. 15, no. 1, pp. 31–45, 1992 (cit. on p. 32).

[100] W. J. Freeman, M. D. Holmes, B. C. Burke, and S. Vanhatalo, "Spatial spectra of scalp eeg and emg from awake humans", *Clinical Neurophysiology*, vol. 114, no. 6, pp. 1053–1068, 2003 (cit. on p. 32).

[101] J.-r. Choi, S.-M. Kim, R.-H. Ryu, S.-P. Kim, and J.-w. Sohn, "Implantable neural probes for brain-machine interfaces–current developments and future prospects", *Experimental neurobiology*, vol. 27, no. 6, p. 453, 2018 (cit. on p. 32).

[102] H. Wark, R. Sharma, K. Mathews, E. Fernandez, J. Yoo, B. Christensen, P. Tresco, L. Rieth, F. Solzbacher, R. Normann, *et al.*, "A new high-density (25 electrodes/mm2) penetrating microelectrode array for recording and stimulating sub-millimeter neuroanatomical structures", *Journal of neural engineering*, vol. 10, no. 4, p. 045 003, 2013 (cit. on p. 32).

[103] W. Shain, L. Spataro, J. Dilgen, K. Haverstick, S. Retterer, M. Isaacson, M. Saltzman, and J. N. Turner, "Controlling cellular reactive responses around neural prosthetic devices using peripheral and local intervention strategies", *IEEE transactions on neural systems and rehabilitation engineering*, vol. 11, no. 2, pp. 186–188, 2003 (cit. on p. 32).

[104] G. Schalk and E. C. Leuthardt, "Brain-computer interfaces using electrocorticographic signals", *IEEE reviews in biomedical engineering*, vol. 4, pp. 140–154, 2011 (cit. on p. 32).

[105] C. L. Frewin, M. Ecker, A. Joshi-Imre, J. Kamgue, J. Waddell, V. R. Danda, A. M. Stiller, W. E. Voit, and J. J. Pancrazio, "Electrical properties of thiol-ene-based shape memory polymers intended for flexible electronics", *Polymers*, vol. 11, no. 5, p. 902, 2019 (cit. on p. 32).

[106] N. A. Feidenhans'l, J. P. Lafleur, T. G. Jensen, and J. P. Kutter, "Surface functionalized thiol-ene waveguides for fluorescence biosensing in microfluidic devices", *Electrophoresis*, vol. 35, no. 2-3, pp. 282–288, 2014 (cit. on p. 32).

[107] X. Xiao, X. Qiu, D. Kong, W. Zhang, Y. Liu, and J. Leng, "Optically transparent high temperature shape memory polymers", *Soft Matter*, vol. 12, no. 11, pp. 2894–2900, 2016 (cit. on p. 32).

[108] M. P. Gaj, A. Wei, C. Fuentes-Hernandez, Y. Zhang, R. Reit, W. Voit, S. R. Marder, and B. Kippelen, "Organic light-emitting diodes on shape memory polymer substrates for wearable electronics", *Organic Electronics*, vol. 25, pp. 151–155, 2015 (cit. on p. 33).

[109] A. Zátonyi, Z. Borhegyi, M. Srivastava, D. Cserpán, Z. Somogyvári, Z. Kisvárday, and Z. Fekete, "Functional brain mapping using optical imaging of intrinsic signals and simultaneous high-resolution cortical electrophysiology with a flexible, transparent microelectrode array", *Sensors and Actuators B: Chemical*, vol. 273, pp. 519–526, 2018 (cit. on p. 33).

[110] R. Fiáth, B. P. Kerekes, L. Wittner, K. Tóth, P. Beregszászi, D. Horváth, and I. Ulbert, "Laminar analysis of the slow wave activity in the somatosensory cortex of anesthetized rats", *European Journal of Neuroscience*, vol. 44, no. 3, pp. 1935–1951, 2016 (cit. on pp. 35, 43).

[111] R. Llinas and Y. Yarom, "Electrophysiology of mammalian inferior olivary neurones in vitro. different types of voltage-dependent ionic conductances.", *The Journal of physiology*, vol. 315, no. 1, pp. 549–567, 1981 (cit. on p. 38).

[112] W. Franks, I. Schenker, P. Schmutz, and A. Hierlemann, "Impedance characterization and modeling of electrodes for biomedical applications", *IEEE Transactions on Biomedical Engineering*, vol. 52, no. 7, pp. 1295–1302, 2005 (cit. on p. 38).

[113] J. J. Jun, N. A. Steinmetz, J. H. Siegle, D. J. Denman, M. Bauza, B. Barbarits, A. K. Lee, C. A. Anastassiou, A. Andrei, Ç. Aydın, *et al.*, "Fully integrated silicon probes for high-density recording of neural activity", *Nature*, vol. 551, no. 7679, pp. 232–236, 2017 (cit. on p. 38).

[114] N. J. Sofroniew, D. Flickinger, J. King, and K. Svoboda, "A large field of view two-photon mesoscope with subcellular resolution for in vivo imaging", *elife*, vol. 5, e14472, 2016 (cit. on p. 39).

[115] R. K. Benninger and D. W. Piston, "Two-photon excitation microscopy for the study of living cells and tissues", *Current protocols in cell biology*, vol. 59, no. 1, pp. 4–11, 2013 (cit. on p. 39).

[116] R. W. Tsien and R. Y. Tsien, "Calcium channels, stores, and oscillations", *Annual review of cell biology*, vol. 6, no. 1, pp. 715–760, 1990 (cit. on p. 39).

[117] M. J. Berridge, P. Lipp, and M. D. Bootman, "The versatility and universality of calcium signalling", *Nature reviews Molecular cell biology*, vol. 1, no. 1, pp. 11–21, 2000 (cit. on p. 39).

[118] G. Buzsáki, C. A. Anastassiou, and C. Koch, "The origin of extracellular fields and currents—eeg, ecog, lfp and spikes", *Nature reviews neuroscience*, vol. 13, no. 6, pp. 407–420, 2012 (cit. on p. 39).

[119] E. Por, M. van Kooten, and V. Sarkovic, "Nyquist–shannon sampling theorem", *Leiden University*, vol. 1, no. 1, pp. 1–2, 2019 (cit. on p. 39).

[120] H. G. Rey, C. Pedreira, and R. Q. Quiroga, "Past, present and future of spike sorting techniques", *Brain research bulletin*, vol. 119, pp. 106–117, 2015 (cit. on p. 40).

[121] R. Q. Quiroga, "Spike sorting", *Current Biology*, vol. 22, no. 2, R45–R46, 2012 (cit. on p. 40).

[122] M. Pachitariu, S. Sridhar, and C. Stringer, "Solving the spike sorting problem with kilosort", *bioRxiv*, pp. 2023–01, 2023 (cit. on p. 41).

[123] A. P. Buccino, C. L. Hurwitz, S. Garcia, J. Magland, J. H. Siegle, R. Hurwitz, and M. H. Hennig, "Spikeinterface, a unified framework for spike sorting", *Elife*, vol. 9, e61834, 2020 (cit. on p. 41).

[124] D. N. Hill, S. B. Mehta, and D. Kleinfeld, "Quality metrics to accompany spike sorting of extracellular signals", *Journal of Neuroscience*, vol. 31, no. 24, pp. 8699–8705, 2011 (cit. on p. 41).

[125] J. A. Hartigan and P. M. Hartigan, "The dip test of unimodality", *The annals of Statistics*, pp. 70–84, 1985 (cit. on p. 41).

[126] A. L. Barth and J. F. Poulet, "Experimental evidence for sparse firing in the neocortex", *Trends in neurosciences*, vol. 35, no. 6, pp. 345–355, 2012 (cit. on p. 42).

[127] S. Sakata and K. D. Harris, "Laminar structure of spontaneous and sensory-evoked population activity in auditory cortex", *Neuron*, vol. 64, no. 3, pp. 404–418, 2009 (cit. on p. 42).

[128] A. A. Robbins, S. E. Fox, G. L. Holmes, R. C. Scott, and J. M. Barry, "Short duration waveforms recorded extracellularly from freely moving rats are representative of axonal activity", *Frontiers in neural circuits*, vol. 7, p. 181, 2013 (cit. on p. 43).

[129] T. Wang, Y. Li, G. Yang, W. Dai, Y. Yang, C. Han, X. Wang, Y. Zhang, and D. Xing, "Laminar subnetworks of response suppression in macaque primary visual cortex", *Journal of Neuroscience*, vol. 40, no. 39, pp. 7436–7450, 2020 (cit. on p. 43).

[130] Y. Senzai, A. Fernandez-Ruiz, and G. Buzsáki, "Layer-specific physiological features and interlaminar interactions in the primary visual cortex of the mouse", *Neuron*, vol. 101, no. 3, pp. 500–513, 2019 (cit. on p. 43).

[131] Y. Li, T. Wang, Y. Yang, W. Dai, Y. Wu, L. Li, C. Han, L. Zhong, L. Li, G. Wang, *et al.*, "Cascaded normalizations for spatial integration in the primary visual cortex of primates", *Cell Reports*, vol. 40, no. 7, 2022 (cit. on p. 43).

[132] X.-S. Yang and J. P. Papa, "Bio-inspired computation and its applications in image processing: An overview", *Bio-inspired computation and applications in image processing*, pp. 1–24, 2016 (cit. on p. 46).

[133] K. H. Höhne and W. A. Hanson, "Interactive 3d segmentation of mri and ct volumes using morphological operations.", *Journal of computer assisted tomography*, vol. 16, no. 2, pp. 285–294, 1992 (cit. on p. 46).

[134] S. J. K. Pedersen, "Circular hough transform", in *Encyclopedia of Biometrics*, 2009 (cit. on p. 47).

[135] "Imfindcircles". (), [Online]. Available: `https://www.mathworks.com/help/images/ref/imfindcircles.html` (visited on 05/08/2020) (cit. on p. 48).

[136] T. J. Atherton and D. J. Kerbyson, "Size invariant circle detection", *Image and Vision computing*, vol. 17, no. 11, pp. 795–803, 1999 (cit. on p. 48).

[137] "Measures of dispersion". (), [Online]. Available: `https://www.mathworks.com/help/stats/measures-of-dispersion.html` (visited on 05/08/2020) (cit. on p. 48).

[138] "Gaussian filtering". (), [Online]. Available: `https://www.cs.auckland.ac.nz/courses/compsci373s1c/PatricesLectures/Gaussian20Filtering_1up.pdf` (visited on 10/30/2020) (cit. on p. 51).

[139] "Types of morphological operations". (), [Online]. Available: `https://www.mathworks.com/help/images/morphological-dilation-and-erosion.html` (visited on 10/30/2020) (cit. on p. 51).

[140] S. Torres-Gomez, J. D. Blonde, D. Mendoza-Halliday, E. Kuebler, M. Everest, X. J. Wang, W. Inoue, M. O. Poulter, and J. Martinez-Trujillo, "Changes in the proportion of inhibitory interneuron types from sensory to executive areas of the primate neocortex: Implications for the origins of working memory representations", *Cerebral Cortex*, vol. 30, no. 8, pp. 4544–4562, 2020 (cit. on p. 66).

[141] G. Ascoli, L. Alonso-Nanclares, S. Anderson, G. Barrionuevo, and R. Benavides-Piccione, "749 burkhalter a, buzsáki g, cauli b., defelipe j., fairén a., petilla interneuron nomenclature 750 group, et al. petilla terminology: Nomenclature of features of gabaergic interneurons of the 751 cerebral cortex", *Nature Reviews Neuroscience*, vol. 9, no. 557-568, pp. 752–753, 2008 (cit. on p. 80).

[142] R. Tremblay, S. Lee, and B. Rudy, "Gabaergic interneurons in the neocortex: From cellular properties to circuits", *Neuron*, vol. 91, no. 2, pp. 260–292, 2016 (cit. on p. 81).

[143] J. M. Cayce, R. M. Friedman, G. Chen, E. D. Jansen, A. Mahadevan-Jansen, and A. W. Roe, "Infrared neural stimulation of primary visual cortex in non-human primates", *Neuroimage*, vol. 84, pp. 181–190, 2014 (cit. on p. 81).

[144] A. M. Stiller, J. O. Usoro, J. Lawson, B. Araya, M. A. González-González, V. R. Danda, W. E. Voit, B. J. Black, and J. J. Pancrazio, "Mechanically robust, softening shape memory polymer probes for intracortical recording", *Micromachines*, vol. 11, no. 6, p. 619, 2020 (cit. on p. 82).

[145] A. M. Stiller, J. Usoro, C. L. Frewin, V. R. Danda, M. Ecker, A. Joshi-Imre, K. C. Musselman, W. Voit, R. Modi, J. J. Pancrazio, *et al.*, "Chronic intracortical recording and electrochemical stability of thiol-ene/acrylate shape memory polymer electrode arrays", *Micromachines*, vol. 9, no. 10, p. 500, 2018 (cit. on p. 82).

[146] D. Khodagholy, J. N. Gelinas, T. Thesen, W. Doyle, O. Devinsky, G. G. Malliaras, and G. Buzsáki, "Neurogrid: Recording action potentials from the surface of the brain", *Nature neuroscience*, vol. 18, no. 2, pp. 310–315, 2015 (cit. on p. 83).

[147] A. Kaszas, G. Szalay, A. Slézia, A. Bojdán, I. Vanzetta, B. Hangya, B. Rózsa, R. O'connor, and D. Moreau, "Two-photon gcamp6f imaging of infrared neural stimulation evoked calcium signals in mouse cortical neurons in vivo", *Scientific Reports*, vol. 11, no. 1, p. 9775, 2021 (cit. on p. 84).

[148] U. Ernsberger, T. Deller, and H. Rohrer, "The diversity of neuronal phenotypes in rodent and human autonomic ganglia", *Cell and tissue research*, vol. 382, no. 2, pp. 201–231, 2020 (cit. on p. 84).

[149] S. Rich, H. Moradi Chameh, V. Sekulic, T. A. Valiante, and F. K. Skinner, "Modeling reveals human–rodent differences in h-current kinetics influencing resonance in cortical layer 5 neurons", *Cerebral Cortex*, vol. 31, no. 2, pp. 845–872, 2021 (cit. on p. 84).

[150] A. Al Abed, J. Amatoury, and M. Khraiche, "Finite element modeling of magnitude and location of brain micromotion induced strain for intracortical implants", *Frontiers in Neuroscience*, vol. 15, p. 727 715, 2022 (cit. on p. 85).

[151] The dblp team, *dblp computer science bibliography*. [Online]. Available: `https://dblp.org`.

[152] F. Mittelbach, M. Goossens, and J. Braams, *The LATEX companion, 2nd Edition* (Addison-Wesley series on tools and techniques for computer typesetting). Addison-Wesley, 2004, ISBN: 0201362996. [Online]. Available: `https://www.worldcat.org/oclc/53972111`.

[153] G. Grätzer, *Practical LaTeX*. Springer, 2014, ISBN: 978-3-319-06424-6. DOI: `10.1007/978-3-319-06425-3`. [Online]. Available: `https://doi.org/10.1007/978-3-319-06425-3`.

[154] P. Kime, M. Wemheuer, and P. Lehman, *BibLaTeX – sophisticated bibliographies in LaTeX*. [Online]. Available: `https://www.ctan.org/pkg/biblatex` (visited on 09/18/2023).

[155] R. Fiáth, A. L. Márton, F. Mátyás, D. Pinke, G. Márton, K. Tóth, and I. Ulbert, "Slow insertion of silicon probes improves the quality of acute neuronal recordings", *Scientific Reports*, vol. 9, no. 1, p. 111, 2019.

[156] M. D. Bagood and R. R. Isseroff, "Trpv1: Role in skin and skin diseases and potential target for improving wound healing", *International journal of molecular sciences*, vol. 22, no. 11, p. 6135, 2021.

[157] B. Csernyus, Á. Szabó, R. Fiáth, A. Zátonyi, C. Lázár, A. Pongrácz, and Z. Fekete, "A multimodal, implantable sensor array and measurement system to investigate the suppression of focal epileptic seizure using hypothermia", *Journal of Neural Engineering*, vol. 18, no. 4, p. 0460c3, 2021.

[158] G. Paxinos and C. Watson, *The rat brain in stereotaxic coordinates, ed 6. amsterdam: Academic*, 2007.

[159] G. Hervieu, J. Cluderay, C. Gray, P. Green, J. Ranson, A. Randall, and H. Meadows, "Distribution and expression of trek-1, a two-pore-domain potassium channel, in the adult rat cns", *Neuroscience*, vol. 103, no. 4, pp. 899–919, 2001.

[160] E. Ismaiel, R. Fiáth, Á. Szabó, Á. C. Horváth, and Z. Fekete, "Thermal neuromodulation using pulsed and continuous infrared illumination in a penicillin-induced acute epilepsy model", *Scientific Reports*, vol. 13, no. 1, p. 14 460, 2023.

[161] T. P. Nedungadi, M. Dutta, C. S. Bathina, M. J. Caterina, and J. T. Cunningham, "Expression and distribution of trpv2 in rat brain", *Experimental neurology*, vol. 237, no. 1, pp. 223–237, 2012.

[162] E. Suh, A. I. Matic, M. Otting, J. T. Walsh Jr, and C.-P. Richter, "Optical stimulation in mice lacking the trpv1 channel", in *Photons and Neurons*, SPIE, vol. 7180, 2009, pp. 112–116.

[163] A. Tóth, J. Boczán, N. Kedei, E. Lizanecz, Z. Bagi, Z. Papp, I. Édes, L. Csiba, and P. M. Blumberg, "Expression and distribution of vanilloid receptor 1 (trpv1) in the adult rat brain", *Molecular Brain Research*, vol. 135, no. 1-2, pp. 162–168, 2005.

[164] M. Plaksin, E. Shapira, E. Kimmel, and S. Shoham, "Thermal transients excite neurons through universal intramembrane mechanoelectrical effects", *Physical Review X*, vol. 8, no. 1, p. 011 043, 2018.

[165] V. Gautam, J. Drury, J. M. Choy, C. Stricker, H.-A. Bachor, and V. R. Daria, "Improved two-photon imaging of living neurons in brain tissue through temporal gating", *Biomedical optics express*, vol. 6, no. 10, pp. 4027–4036, 2015.

[166] M. Göppert-Mayer, "Über elementarakte mit zwei quantensprüngen", *Annalen der Physik*, vol. 401, no. 3, pp. 273–294, 1931.

[167] E. C. Leuthardt, K. J. Miller, G. Schalk, R. P. Rao, and J. G. Ojemann, "Electrocorticography-based brain computer interface-the seattle experience", *IEEE Transactions on Neural Systems and Rehabilitation Engineering*, vol. 14, no. 2, pp. 194–198, 2006.

[168] R. Srinivasan, P. L. Nunez, and R. B. Silberstein, "Spatial filtering and neocortical dynamics: Estimates of eeg coherence", *IEEE transactions on Biomedical Engineering*, vol. 45, no. 7, pp. 814–826, 1998.

[169] J. S. Duncan, J. W. Sander, S. M. Sisodiya, and M. C. Walker, "Adult epilepsy", *The Lancet*, vol. 367, no. 9516, pp. 1087–1100, 2006.

[170] R. B. Yaffe, P. Borger, P. Megevand, D. M. Groppe, M. A. Kramer, C. J. Chu, S. Santaniello, C. Meisel, A. D. Mehta, and S. V. Sarma, "Physiology of functional and effective networks in epilepsy", *Clinical Neurophysiology*, vol. 126, no. 2, pp. 227–236, 2015.

[171] R. S. Fisher, W. V. E. Boas, W. Blume, C. Elger, P. Genton, P. Lee, and J. Engel Jr, "Epileptic seizures and epilepsy: Definitions proposed by the international league against epilepsy (ilae) and the international bureau for epilepsy (ibe)", *Epilepsia*, vol. 46, no. 4, pp. 470–472, 2005.

[172] M. De Curtis and G. Avanzini, "Interictal spikes in focal epileptogenesis", *Progress in neurobiology*, vol. 63, no. 5, pp. 541–567, 2001.

[173] J. G. Jefferys, "Models and mechanisms of experimental epilepsies", *Epilepsia*, vol. 44, pp. 44–50, 2003.

[174] B. Litt and J. Echauz, "Prediction of epileptic seizures", *The Lancet Neurology*, vol. 1, no. 1, pp. 22–30, 2002.

[175] H.-Y. Chu and W. Fang, "Bulk micromachining fabrication platform using the integration of drie and wet anisotropic etching", *Microsystem technologies*, vol. 11, no. 2-3, pp. 141–150, 2005.

[176] B. S. Yilbas, A. Al-Sharafi, and H. Ali, *Self-Cleaning of Surfaces and Water Droplet Mobility*. Elsevier, 2019.

[177] R. Cheung and P. Argyrakis, "Microscale sensors based on silicon carbide and silicon", *Proceedings of the Institution of Mechanical Engineers, Part C: Journal of Mechanical Engineering Science*, vol. 222, no. 1, pp. 19–26, 2008.

[178] B. Bhattacharyya, *Electrochemical micromachining for nanofabrication, MEMS and nanotechnology*. William Andrew, 2015.

[179] B. P. Kerekes, K. Tóth, A. Kaszás, B. Chiovini, Z. Szadai, G. Szalay, D. Pálfi, A. Bagó, K. Spitzer, B. Rózsa, *et al.*, "Combined two-photon imaging, electrophysiological, and anatomical investigation of the human neocortex in vitro", *Neurophotonics*, vol. 1, no. 1, p. 011 013, 2014.

[180] D. O. Adewole, M. D. Serruya, J. A. Wolf, and D. K. Cullen, "Bioactive neuroelectronic interfaces", *Frontiers in neuroscience*, vol. 13, p. 269, 2019.

[181] C. Stosiek, O. Garaschuk, K. Holthoff, and A. Konnerth, "In vivo two-photon calcium imaging of neuronal networks", *Proceedings of the National Academy of Sciences*, vol. 100, no. 12, pp. 7319–7324, 2003.

[182] R. Chittajallu, S. Alford, and G. Collingridge, "Ca2+ and synaptic plasticity", *Cell calcium*, vol. 24, no. 5-6, pp. 377–385, 1998.

[183] J. T. Russell, "Imaging calcium signals in vivo: A powerful tool in physiology and pharmacology", *British journal of pharmacology*, vol. 163, no. 8, pp. 1605–1625, 2011.

[184] C. Grienberger and A. Konnerth, "Imaging calcium in neurons", *Neuron*, vol. 73, no. 5, pp. 862–885, 2012.

[185] E. Neher and T. Sakaba, "Multiple roles of calcium ions in the regulation of neurotransmitter release", *Neuron*, vol. 59, no. 6, pp. 861–872, 2008.

[186] M. J. Berridge, M. D. Bootman, and H. L. Roderick, "Calcium signalling: Dynamics, homeostasis and remodelling", *Nature reviews Molecular cell biology*, vol. 4, no. 7, pp. 517–529, 2003.

[187] B. Schwaller, "Cytosolic ca2+ buffers", *Cold Spring Harbor perspectives in biology*, vol. 2, no. 11, a004051, 2010.

[188] G. Schalk, D. J. McFarland, T. Hinterberger, N. Birbaumer, and J. R. Wolpaw, "Bci2000: A general-purpose brain-computer interface (bci) system", *IEEE Transactions on biomedical engineering*, vol. 51, no. 6, pp. 1034–1043, 2004.

[189] "Basics of neural oscillations". (), [Online]. Available: `https://www.emotiv.com/blogs/tutorials/basics-of-neural-oscillations` (visited on 03/04/2025).

[190] "What is photolithography?" (), [Online]. Available: `https://www.geeksforgeeks.org/what-is-photolithography/#photolithography-process` (visited on 02/03/2025).

[191] "Somatosensory cortex". (), [Online]. Available: `https://brain-for-ai.fandom.com/wiki/Somatosensory_cortex` (visited on 01/19/2025).

[192] Q. Chen, J. Cichon, W. Wang, L. Qiu, S.-J. R. Lee, N. R. Campbell, N. DeStefino, M. J. Goard, Z. Fu, R. Yasuda, *et al.*, "Imaging neural activity using thy1-gcamp transgenic mice", *Neuron*, vol. 76, no. 2, pp. 297–308, 2012.

[193] T. Ware, D. Simon, C. Liu, T. Musa, S. Vasudevan, A. Sloan, E. W. Keefer, R. L. Rennaker, and W. Voit, "Thiol-ene/acrylate substrates for softening intracortical electrodes", *Journal of Biomedical Materials Research Part B: Applied Biomaterials*, vol. 102, no. 1, pp. 1–11, 2014.

[194] S. S. Sahu, "Engineering magnetic hardness of cobalt thin films via phase transformation, grain modification and defects", Ph.D. dissertation, National Institute of Science Education and Research Bhubaneswar, 2017.

[195] A. F. Hussein, N. Arunkumar, C. Gomes, A. K. Alzubaidi, Q. A. Habash, L. Santamaria-Granados, J. F. Mendoza-Moreno, and G. Ramirez-Gonzalez, "Focal and non-focal epilepsy localization: A review", *IEEE Access*, vol. 6, pp. 49 306–49 324, 2018.

[196] M. Carter and J. C. Shieh, *Guide to research techniques in neuroscience*. Academic Press, 2015.

[197] M. Blumberg, J. Freeman, and S. Robinson, *Oxford handbook of developmental behavioral neuroscience*. Oxford University Press, 2009.

[198] Z. Fekete and A. Pongrácz, "Multifunctional soft implants to monitor and control neural activity in the central and peripheral nervous system: A review", *Sensors and Actuators B: Chemical*, vol. 243, pp. 1214–1223, 2017.

[199] R. C. Gonzalez, R. E. Woods, *et al.*, *Digital image processing*, 2002.

[200] L. Wang, L. Ma, J. Yang, and J. Wu, "Human somatosensory processing and artificial somatosensation", *Cyborg and Bionic Systems*, 2021.

[201] R. J. Dolan, "Emotion, cognition, and behavior", *science*, vol. 298, no. 5596, pp. 1191–1194, 2002.

[202] M. L. Phillips, W. C. Drevets, S. L. Rauch, and R. Lane, "Neurobiology of emotion perception ii: Implications for major psychiatric disorders", *Biological psychiatry*, vol. 54, no. 5, pp. 515–528, 2003.

[203] I. Bufalari, T. Aprile, A. Avenanti, F. Di Russo, and S. M. Aglioti, "Empathy for pain and touch in the human somatosensory cortex", *Cerebral cortex*, vol. 17, no. 11, pp. 2553–2561, 2007.

[204] L. Timmermann, M. Ploner, K. Haucke, F. Schmitz, R. Baltissen, and A. Schnitzler, "Differential coding of pain intensity in the human primary and secondary somatosensory cortex", *Journal of neurophysiology*, vol. 86, no. 3, pp. 1499–1503, 2001.

[205] R. Dobson and G. Giovannoni, "Multiple sclerosis–a review", *European journal of neurology*, vol. 26, no. 1, pp. 27–40, 2019.

[206] R. H. Dworkin, "An overview of neuropathic pain: Syndromes, symptoms, signs, and several mechanisms", *The Clinical journal of pain*, vol. 18, no. 6, pp. 343–349, 2002.

[207] F. Mauguiere and J. Courjon, "Somatosensory epilepsy: A review of 127 cases", *Brain*, vol. 101, no. 2, pp. 307–332, 1978.

[208] F. Mauguière, J. E. Desmedt, and J. Courjon, "Astereognosis and dissociated loss of frontal or parietal components of somatosensory evoked potentials in hemispheric lesions: Detailed correlations with clinical signs and computerized tomographic scanning", *Brain*, vol. 106, no. 2, pp. 271–311, 1983.

[209] W. B. Scoville and B. Milner, "Loss of recent memory after bilateral hippocampal lesions", *Journal of neurology, neurosurgery, and psychiatry*, vol. 20, no. 1, p. 11, 1957.

[210] J. J. Knierim, "The hippocampus", *Current Biology*, vol. 25, no. 23, R1116–R1121, 2015.

[211] G. Buzsáki, "Hippocampal sharp wave-ripple: A cognitive biomarker for episodic memory and planning", *Hippocampus*, vol. 25, no. 10, pp. 1073–1188, 2015.

[212] G. Buzsáki, "Theta oscillations in the hippocampus", *Neuron*, vol. 33, no. 3, pp. 325–340, 2002.

[213] K. S. Anand and V. Dhikav, "Hippocampus in health and disease: An overview", *Annals of Indian Academy of Neurology*, vol. 15, no. 4, pp. 239–246, 2012.

[214] V. Dhikav and K. S. Anand, "Is hippocampal atrophy a future drug target?", *Medical hypotheses*, vol. 68, no. 6, pp. 1300–1306, 2007.

[215] T. Bast, "The hippocampal learning-behavior translation and the functional significance of hippocampal dysfunction in schizophrenia", *Current opinion in neurobiology*, vol. 21, no. 3, pp. 492–501, 2011.

[216] F. Caraci, A. Copani, F. Nicoletti, and F. Drago, "Depression and alzheimer's disease: Neurobiological links and common pharmacological targets", *European journal of pharmacology*, vol. 626, no. 1, pp. 64–71, 2010.

[217] M. W. Barnett and P. M. Larkman, "The action potential", *Practical neurology*, vol. 7, no. 3, pp. 192–197, 2007.

[218] B. P. Bean, "The action potential in mammalian central neurons", *Nature Reviews Neuroscience*, vol. 8, no. 6, pp. 451–465, 2007.

[219] A. E. Martinez-Nunez, M. B. Justich, M. S. Okun, and A. Fasano, "Emerging therapies for neuromodulation in parkinson's disease", *Neurotherapeutics*, vol. 21, no. 3, e00310, 2024.

[220] G. T. Einevoll, C. Kayser, N. K. Logothetis, and S. Panzeri, "Modelling and analysis of local field potentials for studying the function of cortical circuits", *Nature Reviews Neuroscience*, vol. 14, no. 11, pp. 770–785, 2013.

[221] R. Chatterjee, A. Datta, and D. K. Sanyal, "Ensemble learning approach to motor imagery eeg signal classification", in *Machine Learning in Bio-Signal Analysis and Diagnostic Imaging*, Elsevier, 2019, pp. 183–208.

[222] D.-W. Park, S. K. Brodnick, J. P. Ness, F. Atry, L. Krugner-Higby, A. Sandberg, S. Mikael, T. J. Richner, J. Novello, H. Kim, *et al.*, "Fabrication and utility of a transparent graphene neural electrode array for electrophysiology, in vivo imaging, and optogenetics", *Nature protocols*, vol. 11, no. 11, pp. 2201–2222, 2016.

[223] R. Jones, "Gathering at the nodes", *Nature Reviews Neuroscience*, vol. 6, no. 9, pp. 664–664, 2005.

[224] K. Xie, S. Zhang, S. Dong, S. Li, C. Yu, K. Xu, W. Chen, W. Guo, J. Luo, and Z. Wu, "Portable wireless electrocorticography system with a flexible microelectrodes array for epilepsy treatment", *Scientific reports*, vol. 7, no. 1, p. 7808, 2017.

[225] K. J. Lee, D. Hong, J.-W. Jang, K. Y. Lee, B. Park, J.-H. Kim, J. S. Kim, and S. Kim, "A wireless ecog recording system to detect brain responses to tactile stimulation", *IEEE Sensors Journal*, vol. 23, no. 12, pp. 13 692–13 701, 2023.

[226] C.-W. Chang and J.-C. Chiou, "A wireless and batteryless microsystem with implantable grid electrode/3-dimensional probe array for ecog and extracellular neural recording in rats", *Sensors*, vol. 13, no. 4, pp. 4624–4639, 2013.

[227] W. H. Theodore and R. S. Fisher, "Brain stimulation for epilepsy", *The Lancet Neurology*, vol. 3, no. 2, pp. 111–118, 2004.

[228] N. A. Kloosterman, J. Q. Kosciessa, U. Lindenberger, J. J. Fahrenfort, and D. D. Garrett, "Boosts in brain signal variability track liberal shifts in decision bias", *Elife*, vol. 9, e54201, 2020.

[229] L. Waschke, N. A. Kloosterman, J. Obleser, and D. D. Garrett, "Behavior needs neural variability", *Neuron*, vol. 109, no. 5, pp. 751–766, 2021.

[230] T. V. Bliss and T. Lømo, "Long-lasting potentiation of synaptic transmission in the dentate area of the anaesthetized rabbit following stimulation of the perforant path", *The Journal of physiology*, vol. 232, no. 2, pp. 331–356, 1973.

[231] P. García-López, V. García-Marín, and M. Freire, "Three-dimensional reconstruction and quantitative study of a pyramidal cell of a cajal histological preparation", *Journal of Neuroscience*, vol. 26, no. 44, pp. 11 249–11 252, 2006.

[232] P. Rubio-Garrido, F. Pérez-de-Manzo, C. Porrero, M. J. Galazo, and F. Clascá, "Thalamic input to distal apical dendrites in neocortical layer 1 is massive and highly convergent", *Cerebral cortex*, vol. 19, no. 10, pp. 2380–2395, 2009.

[233] E. G. Jones and A. Peters, *Cerebral Cortex: Further Aspects of Cortical Function, Including Hippocampus*. Springer Science & Business Media, 2013, vol. 6.

[234] C. R. Noback, N. L. Strominger, R. J. Demarest, and D. A. Ruggiero, "Basic neurophysiology", *The Human Nervous System: Structure and Function*, pp. 41–75, 2005.

[235] H. Gray, *Anatomy of the human body*. Lea & Febiger, 1878, vol. 8.

[236] P. Hemond, D. Epstein, A. Boley, M. Migliore, G. A. Ascoli, and D. B. Jaffe, "Distinct classes of pyramidal cells exhibit mutually exclusive firing patterns in hippocampal area ca3b", *Hippocampus*, vol. 18, no. 4, pp. 411–424, 2008.

[237] J. A. Kim and B. W. Connors, "High temperatures alter physiological properties of pyramidal cells and inhibitory interneurons in hippocampus", *Frontiers in cellular neuroscience*, vol. 6, p. 27, 2012.